UNIVERSITA' DEGLI STUDI DI PADOVA

Centro Interdipartimentale di Studi e Attività Spaziali (CISAS)

SCUOLA DI DOTTORATO DI RICERCA IN SCIENZE TECNOLOGIE E MISURE SPAZIALI (XXI Ciclo)

INDIRIZZO: Astronautica e Scienze da Satellite

Curriculum: Ottica e Strumentazione spaziale

CICLO: XXI

STUDIO DELL'INTERAZIONE DELLA RADIAZIONE ELETTROMAGNETICA CON STRUTTURE NANOMETRICHE PER LO SVILUPPO DI OTTICHE

STUDY OF THE ELECTROMAGNETIC RADIATION INTERACTIONS WITH NANOMETRIC STRUCTURES FOR OPTICS DEVELOPMENT

Direttore della Scuola : Ch.mo Prof. Cesare Barbieri

Supervisore : Ch.mo Prof. Giampiero Naletto

Cosupervisore : Ch.mo Prof. Giampiero Naletto

Dottorando : Michele Suman

Table of Content

Riassunto

Nella regione spettrale dell'EUV e dei raggi x le radiazioni sono altamente energetiche, conseguentemente i modelli teorici che ne descrivono il comportamento sono differenti da quelli classici usati per le onde nella regione spettrale che va dal visibile all'infrarosso (molto meno energetiche).

In questa regione spettrale, infatti, tutti i materiali hanno un assorbimento non trascurabile della radiazione unito ad un basso contrasto ottico.

A causa di ciò i sistemi ottici tradizionali in trasmissione (lenti, prismi) non possono essere utilizzati, si devono pertanto utilizzare ottiche in riflessione. I materiali ed i rivestimenti monostrato, utilizzati nelle regioni a lunghezza d'onda maggiore, offrono però un'efficienza nulla in questa regione spettrale qual'ora utilizzate in incidenza normale (come é necessario per poter contenere le aberrazioni di un sistema ottico e per avere dimensioni contenute del "setup" sperimentale). E' pertanto necessario utilizzare degli specchi con "coating" realizzati da sistemi multistrato, ossia consistenti nel deposito di due o più materiali. Generalmente un materiale presenta il più basso assorbimento possibile, detto anche spaziatore, mentre l'altro, detto anche assorbitore, presenta un assorbimento relativamente alto rispetto al primo.

Una struttura tipica consiste nella ripetizione periodica di un film assorbitore alternato ad uno spaziatore conservando il valore dei singoli spessori lungo tutta la struttura, tale tipo di multilayer viene definito periodico.

Nel caso di multilayer periodici é possibile ricavare, grazie alla legge di Bragg, gli spessori che diano un picco di riflettività ad una data lunghezza d'onda. Nel caso di multilayer aperiodici, invece, risulta molto difficile determinare un metodo per ricavare la scelta degli spessori che diano luogo ad un comportamento predeterminato in riflessione; infatti essi determinano le differenze di cammino ottico tra le onde riflesse ad ogni interfaccia, comportando interferenza costruttiva o distruttiva per le diverse lunghezze d'onda.

Il lavoro di dottorato, presentato in questa tesi, consiste nel disegno nella realizzazione e nella caratterizzazione sperimentale di innovative strutture multistrato aperiodiche disegnate per le più svariate applicazioni quali la fotolitografia, l'astronomia per i raggi x e per l'estremo ultravioletto, e la riflessione di impulsi ultrabrevi, come le armoniche laser di ordine elevato generate nella interazione di impulsi laser ultrabrevi con la materia.

La procedura seguita nella ricerca della distribuzione ottimale di strati si compone nelle seguenti fasi:

• definizione dei parametri liberi da ottimizzare;

• individuazione di una funzione di merito in grado di stimare in maniera adeguata la qualità delle soluzioni al variare dei parametri;

• ottimizzazione dei parametri liberi.

Nella maggior parte dei casi considerati i parametri liberi sono gli strati del multilayer e la funzione obbiettivo é un predeterminato comportamento in riflessione. Considerando la forte irregolarità della riflessione al variare degli strati e l'elevato numero di strati e quindi di parametri liberi del problema (generalmente 100), é preferibile utilizzare algoritmi di ottimizzazione globali quali ad esempio gli algoritmi

genetici. In questo lavoro di tesi un algoritmo genetico, presente nel toolbox di MATLAB, è stato potenziato con delle regole matematiche di selezione.

Fotolitografia EUV

Uno dei più importanti campi di applicazione dei ricoprimenti multistrato è la fotolitografia EUV di nuova generazione, su cui sono concentrate le risorse della grande industria dei processori (Intel, AMD, Motorola ecc). La fotolitografia trasferisce i diversi schemi di circuito su un wafer di silicio proiettando un raggio uniforme di luce laser attraverso una maschera e facendolo convergere in seguito sul materiale fotosensibile di cui è rivestito il wafer di silicio. Successivamente si giunge al disegno finale del circuito attraverso sviluppo, "etching" (rimozione chimica) e deposito dei materiali.

Nel corso degli anni si sono sviluppati circuiti sempre più piccoli, il che solitamente ha comportato componenti elettroniche più piccole, più veloci e meno costose, mediante l'utilizzo di lunghezze d'onda di luce sempre più piccole. Il ridimensionamento delle lunghezze d'onda ha portato a considerare l'utilizzo la radiazione nell'EUV e specchi a multistrato invece che laser e lenti.

Nella fotolitografia EUV i fenomeni che degradano l'efficienza delle ottiche sono la deposizione sulla superficie degli specchi di composti di carbonio e l'ossidazione. In particolare l'ossidazione sembra essere il fenomeno più difficile da arginare, esso ha origine dagli elettroni fotoemessi che rompono le molecole d'acqua, presenti nell'ambiente fotolitografico, generando molecole di ossigeno che si depositano sulla superficie delle ottiche e conseguentemente reagiscono con essa formando uno strato sottile di ossido. Sfortunatamente l'ossido è una tipologia di materiale fortemente assorbente per la radiazione nell'EUV e quindi può degradare di molto l'efficienza delle ottiche di un sistema per la fotolitografia EUV.

Una soluzione adottata per proteggere le ottiche dai fenomeni sopra descritti, e conseguentemente prolungarne il tempo di vita, consiste nella deposizione di due strati protettivi di rutenio e di molibdeno o carburo di silicio sopra le ottiche multistrato. Tale tipo di strati protettivi permettono alle ottiche multistrato di raggiungere gli obbiettivi di tempo di vita utile prefissi dalla "roadmap" della fotolitografia EUV, purtroppo però la loro deposizione sopra una struttura periodica, struttura standard per fotolitografia, ne abbassa di molto l'efficienza.

Nell'ambito di questo lavoro di dottorato sono state realizzate e caratterizzate ottiche multistrato, ricoperte dalle tipologie di strati protettivi descritti prima, disegnate in modo da migliorare la stabilità delle prestazioni rispetto ad ogni possibile cambio delle proprietà ottiche del materiale costituente lo strato protettivo e contemporaneamente massimizzare l'efficienza della riflessione. Tali proprietà derivano dalla differente distribuzione dell'onda stazionaria di queste strutture rispetto le strutture periodiche generalmente utilizzate. Oltre agli effetti appena descritti lo spostamento dell'onda stazionaria ha un altro effetto benefico che è quello di diminuire il numero di elettroni foto-emessi, i quali sono la principale causa di ossidazione delle ottiche in ambiente fotolitografico.

In modo da poter testare sperimentalmente le proprietà appena descritte sono stati depositati alcuni campioni costituiti da questi disegni innovativi (aperiodici) e ricoperti da tre diversi rivestimenti protettivi quali Ru/Mo, Pt/Mo e a-Si//Mo, per poter comparare il reale miglioramento ottenuto sono state depositate anche tre strutture periodiche ricoperte dai medesimi rivestimenti protettivi. Le deposizioni sono state fatte tramite un sistema magnetron sputtering nell'azienda RXOLLC (N.Y. USA) e successivamente i campioni sono stati caratterizzati alla linea BEAR del sincrotrone ELETTRA.

I risultati ottenuti hanno confermato le predizioni, infatti, nel caso delle strutture ricoperte dal rivestimento Ru/Mo le strutture aperiodiche hanno una riflettività più alta e, grazie ad un confronto tra i diversi picchi di riflettività in funzione dei diversi ricoprimenti utilizzati, una sostanziale insensibilità al cambio delle proprietà ottiche del ricoprimento. Inoltre, un'approfondita analisi dei dati ottenuti dalla fotoemissione degli elettroni secondari ha confermato un sostanziale riduzione del numeri di fotoelettroni emessi da parte delle strutture aperiodiche.

Ottiche multistrato per astronomia nell'EUV

Negli ultimi anni telescopi basati su ottiche multistrato ad incidenza normale sono stati impiegati su molte missioni spaziali dedicate all'osservazione del sole nella regione spettrale dell'estremo ultravioletto, come in particolare Fe-IX (17.1 nm), Fe-XII (19.5 nm), Fe-XV (28.4 nm) e He-II (30.4 nm). Esempi di missioni con esito positivo sono SOHO e TRACE. Le prestazioni delle ottiche multistrato in questo campo di applicazione sono principalmente valutate in termini di picco di riflettività per la lunghezza d'onda di una predeterminata riga di emissione e capacità di reiezione delle altre righe.

La coppia di materiali generalmente utilizzata per costituire le ottiche multistrato per osservazioni nell'EUV è Molibdeno/Silicio. Tale tipo di coppia di materiali è una soluzione ben studiata per applicazioni nella fotolitografia, e grazie a ciò in questi ultimi anni è stato sviluppato un notevole background sulla deposizione di ottiche Mo/Si, inoltre, una volta depositata tale coppia di materiali ha un'elevata stabilità e resistenza ai carichi termici.

Purtroppo, strutture multistrato periodiche costituite da Mo/Si, ottimizzate ad esempio per osservare la riga del ferro Fe-XV (28.4 nm), hanno un picco di riflettività relativamente basso rispetto alle altre coppie di materiali utilizzate in questa regione spettrale, inoltre hanno un riflettività a larga banda che può quindi influenzare la diagnostica della riga FeXV a causa del non trascurabile rumore della riga HE II.

Sono state studiate diverse soluzioni a questa problematica, ad esempio è stato proposto un disegno aperiodico delle ottiche multistrato oppure l'utilizzo di altre coppie di materiali quali Mg/SiC, $B_4C/Si/Mo$ oppure B_4C/Si. Purtroppo tali soluzioni non hanno ancora prodotto dei miglioramenti convincenti, inoltre per le coppie di materiali diverse da Mo/Si mancano test e prove di stabilità adeguatamente approfonditi.

Generalmente le ottiche multistrato per missioni spaziali sono protette da dei ricoprimenti costituiti da materiali differenti rispetto quelli utilizzati per l'ottica. Tali ricoprimenti sono in grado di migliorarne le proprietà ottiche e meccaniche, come ad esempio una maggiore resistenza ai rigidi ambienti spaziali oppure

una determinata riflettività nell'UV o nel visibile. In questo lavoro di tesi è stato sviluppato un innovativo metodo matematico per il disegno di ricoprimenti per le ottiche multistrato che, oltre a conferire i miglioramenti ottici e meccanici discussi precedentemente, non influenzano il picco di riflettività della struttura multistrato sottostante ma ne migliorano la reiezione alle altre lunghezze d'onda. La soluzione proposta perciò, oltre a conferire un miglioramento della reiezione di parecchi ordini di grandezza, ha anche un notevole grado di adattabilità.

In questa tesi verrà prima presentato il metodo di disegno dei ricoprimenti discutendone in maniera approfondita tutti gli aspetti teorici. Verranno quindi presentati dei risultati di simulazioni toriche di risposta ottiche multistrato alle quali sono stati integrati questi ricoprimenti, comparandone quindi le prestazioni con le ottiche utilizzate attualmente. Infine verranno presentati i risultati sperimentali e le relative metodologie di analisi, sviluppate in fase di realizzazione e caratterizzazione di tali ottiche, in grado di aiutare a comprendere e correggere gli eventuali errori di deposizione critici che si possono avere. Il risultato finale sono le misure di tali ricoprimenti fatte al sincrotrone ALS (Berkley).

Ottiche multistrato per astronomia nei raggi x

I telescopi per osservazioni nei raggi x utilizzano in genere le configurazioni ideate da Wolter da cui prendono anche la denominazione. In passato gli specchi erano ricoperti da un singolo strato e sfruttavano il fenomeno della riflessione totale. Questo approccio però diventa molto critico nel caso in cui il "range" energetico di osservazione supera i 10 KeV, infatti ad energie così elevate la riflessione totale avviene per angoli di incidenza radente molto piccoli. In conseguenza di ciò tolleranze meccaniche molto restringenti sono richieste in fase di allineamento e nel montaggio ottico.

Molto recentemente la scoperta e sviluppo di ottiche multistrato ha rivoluzionato la "roadmap" dello sviluppo tecnologico di telescopi per i raggi x. Lo sviluppo di ottiche multistrato sempre più performanti in questa regione spettrale è perciò diventato un punto cruciale per l'astronomia nei raggi x. Differenti approcci sono stati usati per trovare strutture multistrato ottimali in termini di riflettività a larga banda. A tale scopo sono stati utilizzati algoritmi di ottimizzazione globali quali gli algoritmi genetici, o algoritmi di "simulated annealing", capaci di cercare soluzioni ottimali in un dominio molto ampio. Alcuni strumenti matematici sono stati inoltre sviluppati per aiutare gli algoritmi di ottimizzazione a convergere verso soluzioni ottimali come ad esempio la distribuzione "powerlaw". Recentemente un notevole passo avanti è stato fatto con la costruzione di un formalismo matematico capace di fornire disegni di ottiche multistrato con una riflettività molto piatta.

In questa tesi di dottorato verranno presentati i risultati preliminari dell'ottimizzazione di strutture multistrato a larga banda.

Ottiche multistrato per la riflessione di impulsi ultrabrevi agli attosecondi

Un'applicazione interessante per l'ottimizzazione di strutture multistrato aperiodiche è lo studio di multilayer per la riflessione di impulsi ultrabrevi. La generazione e la manipolazione di impulsi ultrabrevi di durata inferiore al femtosecondo dà la possibilità di indagare fenomeni che a causa della loro brevissima durata temporale risultavano fino ad oggi inaccessibili. Secondo il modello teorico di Bhor per esempio, l'elettrone dell'atomo di idrogeno compie una rotazione intorno al nucleo in circa 150 attosecondi; quindi per osservare e controllare gli elettroni in movimento bisogna utilizzare impulsi di luce della durata di alcuni attosecondi.

Gli impulsi ultrabrevi possono essere generati selezionando porzioni spettrali di armoniche di ordine elevato generate dall'interazione tra un gas nobile ed un impulso ultrabreve ed ultra intenso. Lo spettro delle armoniche di ordine elevato è caratterizzato da degli "spikes" di intensità in corrispondenza delle armoniche della fondamentale di ordine dispari e può coprire la regione spettrale che và dall'infrarosso all'XUV. Due importanti regioni caratterizzano lo spettro delle armoniche d'alto ordine e sono quella del plateau (si tratta della regione spettrale che va dalla quarta armonica fino generalmente all'XUV ed ha uno spettro piatto) e quella del "cut–off" (è la caduta esponenziale che si ha dopo la regione del plateau). Il confine tra la regione del plateau e quella del "cut–off" dipende dall'intensità dell'impulso ultrabreve che interagisce col gas, sostanzialmente più intenso è l'impulso e più il confine si sposta verso la regione x.

Nella regione spettrale dell'XUV i rivestimenti multistrato sono l'unica ottica in grado di garantire livelli di efficienza adeguati per la riflessione ad incidenza normale, tali ottiche sono perciò guardate con estremo interesse dalla comunità scientifica dell'attofisica. Oltre a garantire adeguati livelli di efficienza le ottiche per impulsi ultrabrevi devono riuscire a controllare e possibilmente correggere la forma dell'impulso in modo da ottenere uno spettro gaussiano ed una fase lineare; essa è infatti la combinazione che a parità di banda spettrale dà un impulso di durata temporale minore.

Le strutture multilayer periodiche sono caratterizzate da una banda di alcuni eV a circa 100 eV. Ciò significa che nel caso di impulsi di circa 100 attosecondi il corrispondente largo "range" spettrale (circa 30 eV) non può essere preservato dopo la riflessione allargando perciò la durata temporale dell'impulso, da qui la ricerca di strutture aperiodiche con riflettività a larga banda. Oltre ad una larga banda spettrale gli impulsi ultrabrevi sono caratterizzati da un andamento della fase in funzione della frequenza che può essere lineare oppure quadratico positivo ("chirped"). Questi due diversi andamenti di fase dipendono dalla regione dello spettro in cui si trova la porzione di armoniche selezionate, infatti nel caso in cui la porzione sia nella regione del "cut–off" la fase è lineare nel caso invece sia nella regione del plateau la fase è "chirped".

La ricerca di multilayer per la riflessione di impulsi ultrabrevi è perciò la ricerca di strutture caratterizzate da una riflettività a larga banda possibilmente in grado di ridistribuire e sfasare le componenti spettrali incidenti in modo da riflettere uno spettro di forma gaussiana.

Utilizzando l'algoritmo sviluppato in questo lavoro di tesi sono state ottimizzate ottiche multistrato per la riflessione di impulsi ultrabrevi, più specificatamente sono state ottimizzate strutture in grado di compensare un fase "chirped" ed in grado di ridisegnare uno spettro rettangolare in forma gaussiana. Le strutture

ottenute sono state poi testate aggiungendo degli errori casuali dell'ordine di 2 Å agli strati e non sono state riscontrate rilevanti criticità assicurando perciò una fattibilità sperimentale delle strutture.

Verrà inoltre presentato in questa tesi un'innovativa metodologia di caratterizzazione sperimentale, sviluppata nell'ambito di questo lavoro di tesi, che permetterà una ricostruzione molto precisa della fase delle ottiche multistrato partendo dal segnale degli elettroni fotoemessi.

Abstract

A suitable throughput in the EUV spectral range can be obtained using a grazing incidence optical configuration, however, for small reflection angles, useful also for limited size of the experimental setup and optic system aberrations reduced, the multilayer reflective coatings have to be used.

A typical multilayer coating consists in a periodic structure realized by the alternating deposition of films of two or more different materials with relatively high optical contrast and low absorption. The multilayer working principle is based on the constructive interference among the electromagnetic wave components reflected at the various interfaces. The films thickness is defined in order to comply this principle for predetermined wavelengths. The choice of the materials is made in order to maximize their optical contrast, i.e. in such a way that their refraction index are as different as possible. In this way, according with the Fresnel law, the amplitude of the electromagnetic wave reflected at each interface is maximized.

In this PhD work have been optimized aperiodic multilayer structures for different applications like: EUV and x-ray astronomy, EUV lithography and reflection of attosecond ultrashort pulses, like those due to high order harmonics of laser pulses generated in the interaction of ultrashort laser pulses with matter. The input parameters are the multilayer thicknesses, materials and layers number, instead the merit function is the multilayer reflection.

Multilayer coating for EUV lithography

Pertaining the design of EUVL multilayers, novel aperiodic structures covered by capping layers resistant to environmental attack have been developed. This multilayer offer superior performance for extreme ultraviolet lithography, in particular an integrated intensity increase of up to 2.18 times that obtained using standard periodic multilayers has been estimated. The a-periodic structures have minimal absorption in the top-most layers, which makes them especially insensitive to both the choice of capping layer material, and to any subsequent capping layer degradation due to oxidation or contamination. This property allows for the use of the most resilient capping layer materials available, thereby leading to significantly improved lifetime. We have produced prototype capped a-periodic coatings and have measured their performance.

Multilayer coating for EUV astronomy

Space optic instrumentation for the sun observation in the Extreme Ultraviolet (EUV) spectral region is often based on multilayer coating technology. Such coatings have not negligible bandwidth, and therefore,

often the detected signal is due to the contribution of different very close spectral lines. In this PhD work we present a study of innovative capping layer structures covering the multilayer coating able to improve the rejection of the unwanted lines and at the same time preserving the reflectivity peak at the working wavelength. The mathematical design method will be presented and discussed. Moreover, theoretical results for some structures designed by the use of the new mathematical tool will be presented and discussed. Experimental results related to periodic Mo/Si multilayer covered by an optimized Mo/Si capping layer able to reflect the Fe-XV line with rejection ratio of some orders of magnitude for the near He-II intense line are presented.

Multilayer coating for x ray astronomy

The configurations adopted in X-ray telescopes are based on the Wolter designs. In the past mirrors have been coated by a single material layer exploiting the external reflection phenomena. This approach can be very critical at energies above 10 keV, since external reflection appears at very low grazing incidence angle, and therefore very tight mechanical constraints in mirror alignment and on optical mounts are required. More recently the discovery and development of multilayer coatings have revolutionized the roadmap of the x-ray telescope's technology. Different mathematical approaches have been used for finding the optimum solution in term of broadband reflectivity. Global optimization algorithms like genetic algorithm or simulated annealing capable of searching the optimum structure inside a very wide domain of possible solutions have been used. Some mathematical tools adopt layer design constraints able to guide the focusing of the algorithms toward specific types of solution, as depth graded multilayer with a powerlaw layer distribution. More recently, a further step has been represented by a math formalism able to provide chaotic layer distribution solutions which have gain of very flat reflectivity.

In this PhD work we show the preliminary results of some broadband W/B_4C multilayer design.

Multilayer coating for EUV attosecond pulses

In the field of attosecond pulses generated by high–order harmonics both the harmonic spectral shape and the spectral phase have to be controlled. In the case of plateau harmonics, the need is to compensate the phase mismatch between different harmonics and obtain a Gaussian reshaping of the spectrum, while, in the case of cut-off harmonics the phase locking has to be preserved for obtaining a Gaussian reshaping of the spectrum. It is worth to be noted that for attosecond experiments it is essential to study optical design capable to comply with the above requirements. For the VUV and XUV harmonics reflection an interesting solution are multilayer mirrors. Typical periodic structures are characterized by energy band coverage usually restricted to few percent of the peak energy i.e., for example, a few eV at about 100 eV. This means that in the case of ultra-short radiation pulses (< femtosecond) the corresponding "wide" spectral features cannot be preserved. In this PhD work we study aperiodic multilayer designed in order to reflect attodsecond pulses.

# Chapter 1: Introduction to the multilayer coatings

During the last decades x-ray research has been involved in several fields ranging from astronomy to photolithography and biology. The development of high efficiency optics is critical because below about 35 nm the reflectivity of materials is close to zero at normal incidence, and consequently, the optical instruments adopt grazing incidence configurations. Grazing incidence instruments are in general extremely complex, have very small acceptance apertures and consequently low luminosity and in addition to this a great problem is posed by the reduction of optical aberrations characteristic of these configurations.

So the development of high efficiency EUV optics in normal incidence configuration would improve both the throughput and the resolution capability of the instrumentation. The solutions to these requirement is the XUV multilayer optics, they are constituted by an alternating sequence of thin films of highly absorbing (absorber) and less absorbing (spacer) materials [1]. The high reflectivity, also at near normal incidence configurations, derives from the interference of the Fresnel components reflected from the interfaces between materials of high and low absorption (see Fig. 1). The sum of the thickness of absorber layer and spacer one is called period (see Fig. 1):

$$period = d_{spacer} + d_{absorber} \qquad (1)$$

and the ratio between the thickness of the absorber layer and the period is called γ:
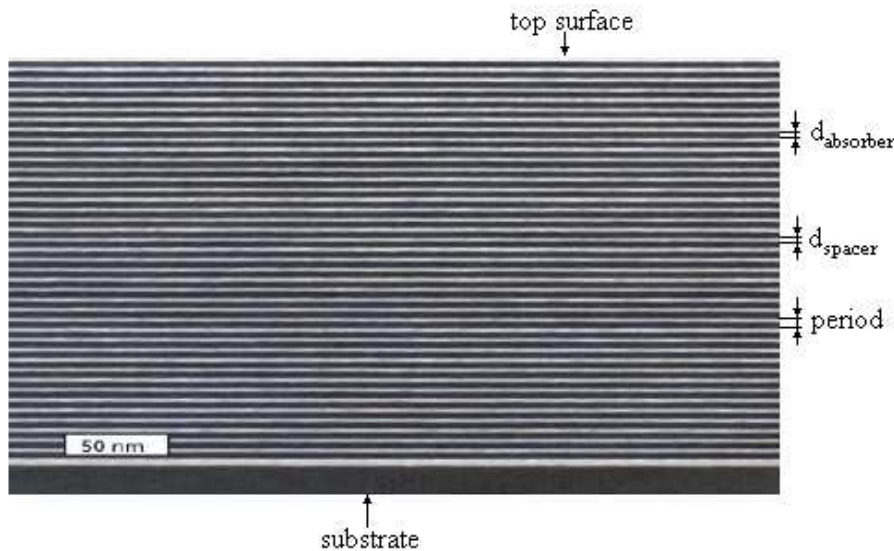
$$\gamma = d_{spacer}/period. \qquad (2)$$

Fig. 1 *Section image of a multilayer, the period, spacer and absorber materials, the top surface and the substrate are shown.*

Typical multilayer designs are periodic, it means that the structures have constant period and γ ratio. In this case the structures can be easily optimized to obtain reflectivity peak at a particular frequency using the Bragg law. Differently the aperiodic (inconstant period and γ distribution along the multilayer stack) designs increases the size of the solution space but increases also the free parameters for structure definition. In fact

the thickness of each layer has to be optimized for matching the relative phase of the various Fresnel components reflected and inter-reflected by multiple paths into the stack, so that in the outgoing waves the various components can interfere constructively or destructively. The optimization and following successful realization of suitable aperiodic stacks for different applications is a problem of great interest for the multilayer community.
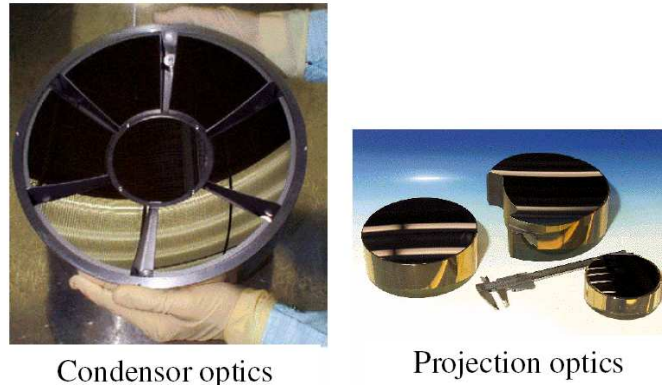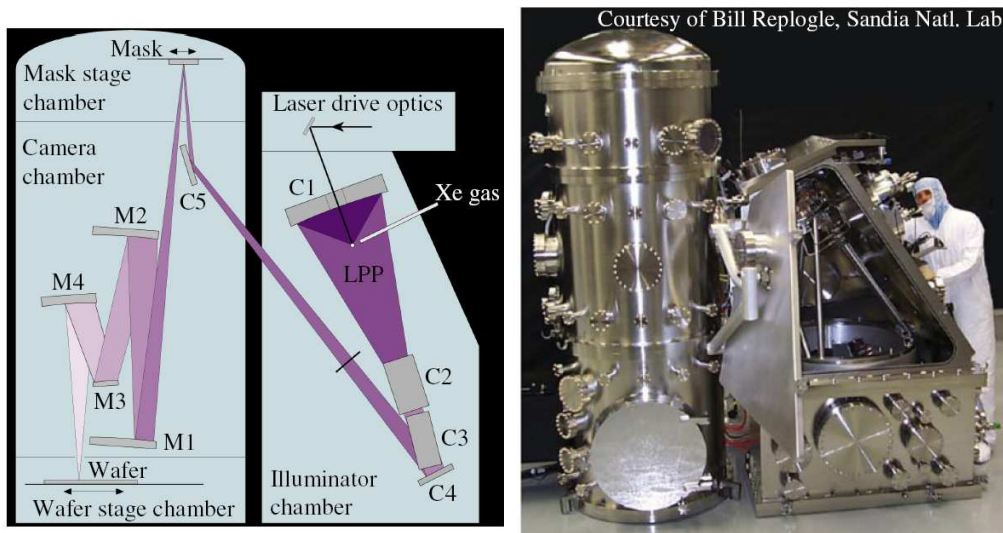

Condensor optics   Projection optics

Fig. 2 Two images respectively of condenser and projection optics used for EUV lithography systems (font: courtesy of Bill Replogle, Sandia National Laboratoires).

Fig. 3 A schematic image (left side) coupled with a photo (right side) of a EUV lithography system. The mirror called C1-C5 belong to the collector optic system, instead, the mirror called M1-M4 belong to the projection optic system. LPP is the acronym of laser produced plasma (font: courtesy of Bill Replogle, Sandia National Laboratoires).

In this PhD thesis the design, realization and characterization of innovative multilayers have been studied and discussed. In the second chapter the different methods related to the calculation and optimization of the multilayer performances has been discussed. A detailed discussion of the recursive model used for the reflection, transmission and standing wave theoretical prediction is presented in this chapter, moreover, in the final part of the chapter an overview of the different optimization methods useful in the multilayer design is introduced.

In order to clarify the exposition of the thesis the innovative contributes involving the quite different application fields have been discussed and contextualized in different chapters. In particular the EUV and x-ray astronomy, attosecond ultra-short pulse reflection and EUV lithography fields and relative innovations has been discussed respectively in the chapters 3,4,5 and 6. In the chapter 7 the conclusions has been exposed.

1.1   Multilayer coating for EUV lithography

In the case of EUV lithography (EUVL) application the multilayer efficiency, 30% loss at each mirror, are somewhat inefficient. This limits the practical number of optical elements that can be used and imposes the use of aspheric surfaces (see Fig. 2), making figure and finish specifications even more severe and difficult to achieve. Respect to the UV lithography, system actually used, the EUVL optics system have some structural differences (see Fig. 3), arising the complexity of the technology employed, like: reflective photomasks, and new types of plasma light sources able to generate the short wavelength EUV light, and the wafers exposed under vacuum in order to minimize EUV intensity losses by absorption due to residual environmental gas.The main goal of the multilayer optics applied to the EUVL systems is to obtain high reflectivity throughput, moreover, other manufacturing goals are to simultaneously meet the stringent figure and finish requirements of the reflecting surface and how to get stable performance without the reflectivity degradation. In particular, regarding this last goal the EUV optics must meet a requirement of less than 1% non-recoverable reflectivity loss during 30000 light-on hours [2], equivalent to 10-year operating lifetime. Because the projection optics cannot be heated to achieve ultra-high vacuum conditions (as this would damage the reflective multilayers), they must operate in an environment with the presence of water vapor and hydrocarbons. Under EUV exposure in these conditions, the optics can be subjected to recoverable and non-recoverable reflectivity losses: water adsorbed on surfaces may be dissociated by EUV photons or by secondary electrons generated by the photons, leading to oxidation of the reflecting surface and a non-recoverable reflectivity loss. The dissociation of adsorbed hydrocarbons can also result in elemental carbon buildup, although this may be removed through reactions with oxygen or hydrogen and evidence suggests that water vapor and hydro-carbon partial pressures can be optimized for a given EUV photon flux such that carbon buildup and oxidation are balanced.

Progress in EUVL optics lifetime can be obtained studying new materials covering multilayer optics and understanding its degradation under EUVL environment. Moreover, because the typical multilayer design is periodic a further throughput improvement can be obtained through aperiodic design obtaining for example a better match with the spectral source. In this PhD framework we have designed and tested a-periodic multilayer structures containing protective capping layers in order to obtain improved stability with respect to any possible changes of the capping layer optical properties (due to oxidation and contamination, for example)-while simultaneously maximizing the EUV reflection efficiency and match with particular spectral sources.

1.2   Multilayer coating for EUV astronomy applications

In the case of multilayer optics applied to EUV astronomy, the high throughput at near-normal incidence angles of these optics has been the enabling technology for solar imaging instruments in this spectral range. In the last decade, narrowband multilayer in normal-incidence telescopes have been flown aboard rockets and satellites to image the Sun at some EUV wavelengths. The main motivation of this approach is the feasibility in producing experimental setup more compact than the grazing incidence optical configuration. Multilayer normal-incidence telescopes were first used to image the Sun from rockets. More recently, the EUV Imaging Telescope (EIT) (see Fig. 4) [3-4] satellite experiment, which is part of the Solar and Heliospheric Observatory (SOHO), was designed to image the Sun in four narrow EUV wavelength bands centered at 17.3, 19.5, 28.4, and 30.4 nm (see Fig. 5). It has a spatial resolution of approximately 5" (pixel size is 2".6). TRACE [5], a second multilayer normal-incidence telescope that was launched in early 1998 as a Small Explorer (SMEX) mission, is designed to observe the Sun with 1" resolution (pixel size is 0".5) in three EUV and four UV wavelength bands. The three EUV bands are centered at 17.3, 19.5, and 28.4 nm. Since the wavelength pass-bands of EIT and TRACE are rather wide, their response to emission arising from a particular temperature regime can, as for grazing-incidence telescopes, be fairly contaminated by the contributes of the near sun lines. The wavelength bands selected for multilayer imaging were chosen to provide peak reflectivity for strong spectral lines that are primarily emitted over a single, rather narrow, temperature interval. Study of the solar spectrum has revealed many such possible wave bands [6]. Thus, a comparison of images obtained in different multilayer bands reveals the solar morphology at different temperatures. This technique works very well for quiet-Sun and active-region structures.
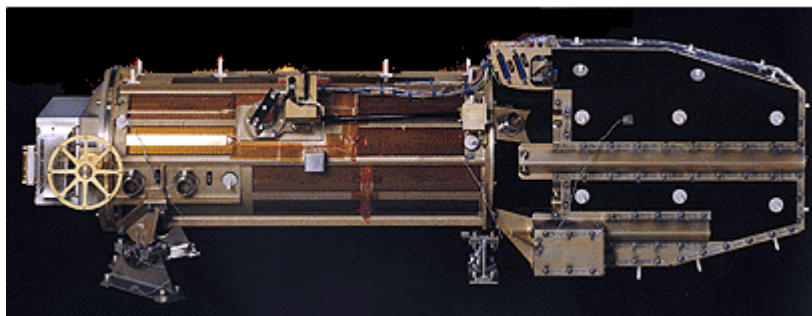
Fig. 4 *A photo of the EIT telescopes flying on board of the SOHO mission* (font: http://umbra.nascom.nasa.gov/eit/).
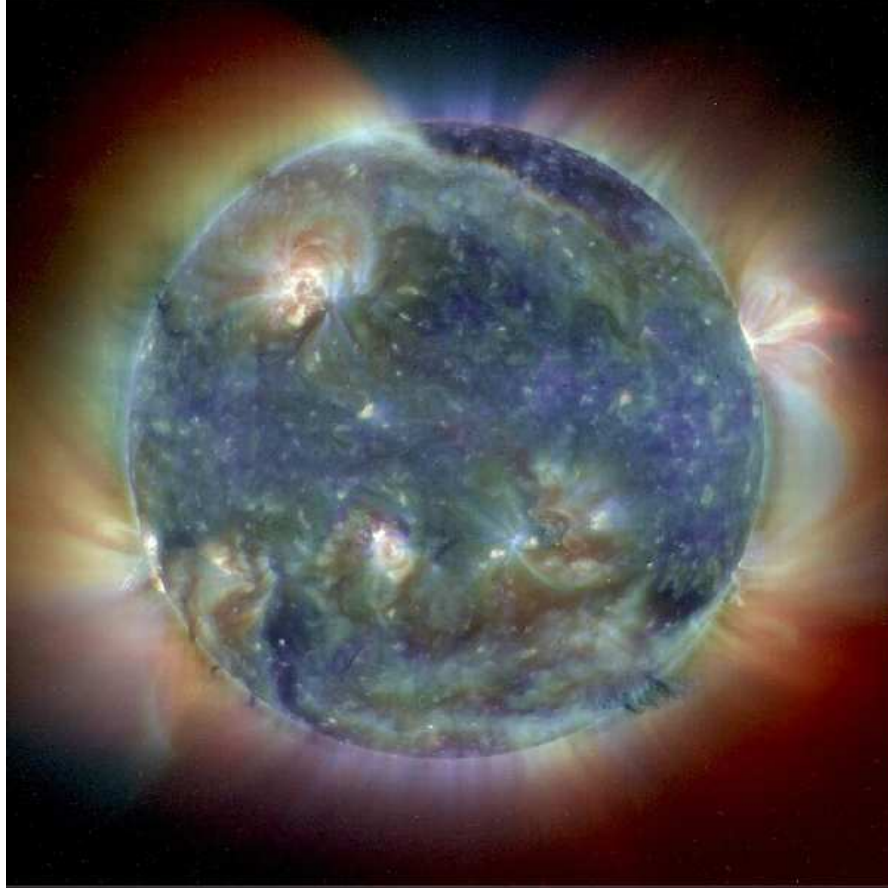
Fig. 5 *"This composite image combines EIT images from three wavelengths (17.1 nm, 19.5 nm and 28.4 nm) into one that reveals solar features unique to each wavelength. Since the EIT images come to us from the spacecraft in black and white, they are color coded for easy identification. For this image, the nearly simultaneous images from May 1998 were each given a color code (red, yellow and blue) and merged into one."*

http://soho.nascom.nasa.gov/gallery/images/trico1.html

Because of their good time stability, Mo/Si multilayer are conventionally used for all the EUV wavelengths, even if, at the longest ones they have relatively low reflectivity peak and spectral resolution with respect to other material couples. A suitable narrower reflectivity multilayer than the periodic Mo/Si case has been obtained through an a-periodic design of Mo/Si structure [7]. Moreover, further enhancement of peak reflectivity can be obtained using other material combinations like Mg/SiC [8], $B_4C/Si/Mo$ [9] or B_4C/Si [8]. Although for some of these structures, test and proof of lifetime stability must be investigated. Study of new capping layer and multilayer design able to improve the spectral filtering of the multilayer reflectivity will be showed and discussed in this thesis, in particular thank to a multilayer design based on the standing wave distribution into the multilayer structure interesting results in term of reflectivity spectral filtering have been obtained.

1.3   Multilayer coating for x ray astronomy applications

Hard x-ray observations allow us to study physical processes that either do not occur at lower energies or are dominated at low energies by thermal emission from the hot (10^7 K) plasma commonly found in high-energy sources. High-sensitivity observations in hard x-ray spectral region have not been carried out because the imaging systems used, collimators and coded aperture masks, cannot satisfy the required sensitivity levels. Focusing telescopes have provided high-sensitivity observations for spectral region lower than 10 keV. The use of focusing in the low energy x-ray band began with the Einstein Observatory (1978 - 1981, 0.1-4 keV) [10]; it had a ratio of detecting to collecting area of 10^3–10^4 and it was hundreds of times more sensitive than its non-focusing predecessors. Subsequently, the energy range of focusing telescopes has been extended to ≈ 10keV with the Chandra X-ray Observatory (CXO) (see Fig. 6) and XMM-Newton (see Fig. 7), both launched in 1999 [11-12]. CXO, with arcsecond imaging performance has a collecting to detecting area ratio of roughly 107.

Fig. 6 *Workers at Eastman Kodak in Rochester, N.Y., test the alignment of the Chandra observatory's High-Resolution Mirror Assembly.* (font: www.nasa.gov/.../chandra/assembly.htm_prt.htm , photo of Eastman Kodak).

Focusing optics have not been used at energies above 10 keV because the optics currently used on x-ray telescopes are difficult to employ in practical hard x-ray telescopes. Today's focusing telescopes are based on total external reflection, in fact in the x-rays, where the refractive indices of materials are smaller than the vacuum refractive index, total external reflection occurs at grazing incidence angles, on the order of several milliradians. The grazing incidence optics used by Chandra, XMM and all previous x-ray focusing telescopes are difficult to use at higher energies because the critical reflection angle, above which reflectance is negligible, is proportional to 1/E. The main problem with total external reflection grazing

incidence optics is that the reduction in the critical angle at higher energies translates directly into a decrease in the field of view of the telescope. In addition, the small grazing angles force the telescope design to employ either small radius optics or a long focal length. Small radius optics are undesirable because they dilute the sensitivity gains of focusing systems. A long focal length (> 30m) increase the power (and hence weight and cost) requirements on the spacecraft.

Reflectance at angles greater than the critical graze angle can, however, be achieved by using depth graded multilayer coatings on the mirror surfaces [13-14]. Typical material couples for the hard-x ray spectral region are tungsten and silicon (W/Si), or platinum and carbon (Pt/C)). Designing suitable aperiodic multilayer (super-mirror) one can obtain broad band x-ray reflectors operating at angles greater than the critical one. Several multilayer mirror telescopes are currently being developed to extend focusing capability to higher energies. These efforts include at least two balloon instruments, "In Focus" [15], being developed by Goddard Space Flight Center and Nagoya University in Japan, and the High Energy Focusing Telescope (HEFT) (see Fig. 8) [16-17], being developed by Caltech, Columbia University, Danish Space Research Institute, and Lawrence Livermore National Laboratory .In addition, the Constellation-X mission concept [18] includes a hard x-ray focusing telescope. The design of performing and feasible aperiodic broadband structures will be treated in this thesis.

Fig. 7 *One of the mirror modules from the XMM-Newton X-ray telescope. This module consists of 58 mirror shells made of gold-plated nickel.* (font:
http://www.esa.int/esa-mmg/mmg.pl?b=b&keyword=xmm%20mirrors&single=y&start=18)
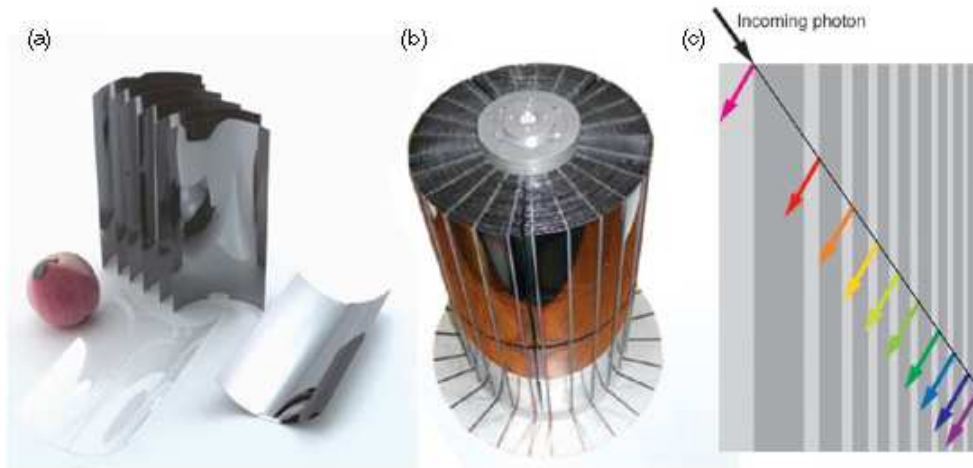
Fig. 8 *" a) The High Energy Focusing Telescope's (HEFT's) optic mirrors are made from glass originally developed for flat-panel computer monitors. The glass is thermally formed and then covered with a multilayer coating composed of alternating layers of materials that vary in thickness. (b) Seventy-two mirror shells are assembled for each of HEFT's three telescopes. (c) The multilayer structure is efficient for a wide range of angles and photon wavelengths (energies). Photons are reflected off the interface between the different materials, thus "tricking" light into seeing more mirrors. The colored arrows indicate the reflectivity from a range of x-ray energies, from the lowest (pink arrow) to the highest (violet arrow). "* (font: https://www.llnl.gov/str/November04/Craig.html)

1.4   Multilayer coating for reflection of EUV attosecond pulses

Generation of ultra-short light pulses of relatively high energy photons has opened a new frontier to matter physics in a very short time scale. Ultrashort pulses can be generated in the interaction with gas jets of femtosecond laser pulses focused at high power density; the ionization of the atoms in the laser field produces a spectrum of laser harmonics extending from the near infrared up to the x-ray region [19]. It has been proved that the high order harmonics (HOH) are emitted in a time corresponding to a short fraction of the fundamental laser period by the electrons accelerated in the laser field. A HOH spectrum is characterized by three main regions (see Fig. 9):

1   the first fall involving the first harmonics

2   a region where the harmonics have the same intensity called plateau regions

3   cut off region, is the region where the harmonic fall down, this limit is related to the intensity of the femtosecond laser pulse interacting with the gas jet.

Correspondingly, by suitably selecting a portion of the HOH spectrum pulses with sub-femtosecond time duration can be obtained [20-21]. In particular, selecting only the HOH cut–off region generated by few optical cycle infrared LASER guide pulse, a single attosecond pulse can be generated. Differently, selecting the discrete HOH spectrum in the plateau region, an attosecond pulses train can be obtained. On the other side preservation of ultra–short time structures can be achieved by compensation of the non–linear phase trend introduced in the reflection processes by usual optical components.

The ultra-short time characteristic of high energy harmonic spectrum has been used in some noticeable experiments. In pump-probe studies the analysis of transient atomic phenomena like the relaxation of core-excited atoms [22] or to the study of the excitation of photoelectrons in the presence of strong light field is analyzed [23-24]. A different use of ultra-short pulses is their use like seeding source for x–ray free electron LASER [25]. In all these applications types the soft x-ray pulse obtained by selecting a portion of the HOH spectrum has to be steered and focused with suitable optics. Attosecond pulses generation from HOH spectra has been obtained through a opportune spectral filtering. Moreover some filters presenting a suitable Group Delay Dispersion (GDD) can compress the transmitted pulse [26].

Considering that suitable designed multilayer coatings can manipulate and lead the attosecond pulses, and therefore give further improvement in the attosecond science employments, in the last years some studies concerning the applications of multilayer coating to the reflection of attosecond pulses have been presented [27].

The design of broadband EUV multilayer for the reflection and (thanks to the phase compensation) compression of attosecond pulses has been studied in this thesis. Some different cases are showed and discussed, moreover, experimental realization and test of such type of structure has been showed.
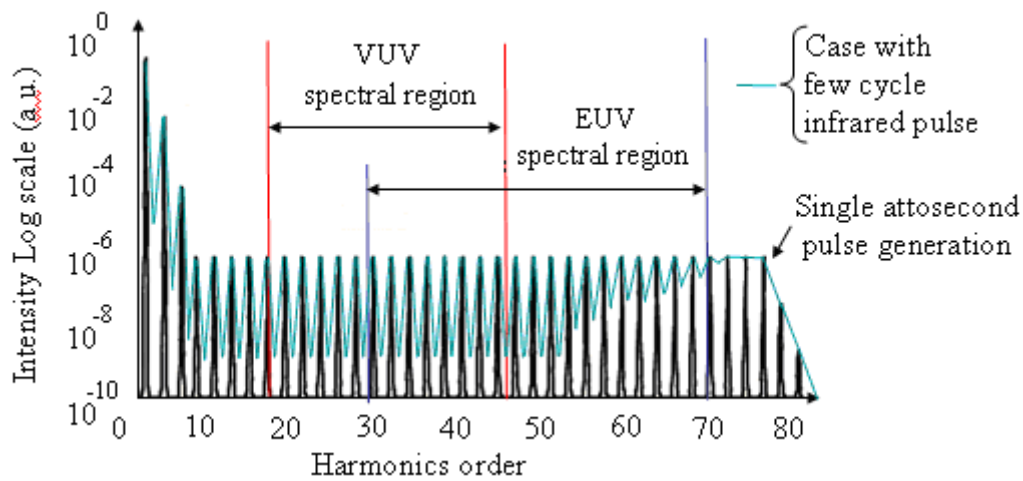
Fig. 9 *A schematic representation of the High Order Harmonics spectrum.*

References

1   Spiller E. Soft X-ray Optics

2   S. Wurm and K. Kemp, "SEMATECH pushes extreme ultraviolet lithography forward," http://spie.org/x8865.xml.

3   Delaboudiniere J.-P., Artzner G. E., Brunaud J., Gabriel A. H., Hochedez J. F., Millier F., Song X. Y., Au B., Dere K. P., Howard R. A., Kreplin R., Michels D. J., Moses J. D., Defise J. M., Jamar C., Rochus P., Chauvineau J. P., Marioge J. P., Catura R. C., Lemen J. R., Shing L., Stern R. A.,

Gurman J. B., Neupert W. M., Maucherat A., Clette F., Cugnon P., Van Dessel E. L. EIT: Extreme-Ultraviolet Imaging Telescope for the SOHO Mission, Solar Phys., 162 291–312, 1995

4   http://umbra.nascom.nasa.gov/eit/

5   http://trace.lmsal.com/

6   Golub L., Hartquist T. W. and Quillen A. C., Solar Phys., 122, 245, 1989.

7   J. Zhu, Z. Wang, Z. Zhang, F. Wang, H. Wang, W. Wu, S. Zhang, D. Xu, L. Chen, H. Zhou, T. Huo, M. Cui and Y. Zhao, "*High reflectivity multilayer for He-II radiation at 30.4 nm*" Applied Optics Vol. 47, issue 13 , pp C310-314, 2008.

8   S. Zuccon, D. Garoli, M.G. Pelizzo, P. Nicolosi, S. Fineschi and D. Windt, "Multilayer coating for multiband spectral observations", in Proceedings of the International Conference on Space Optics (ICSO), ESA-SP (European Space Agency, 2006).

9   J. Gautier, F. Delmotte, M. Roulliay, F. Bridou, M.F. Ravet, and A. Jérome, "*Study of normal incidence of three-component multilayer mirrors in the range 20-40 nm*" Applied Optics Vol. 44, pp 384-390, 2005.

10 http://heasarc.gsfc.nasa.gov/docs/einstein/heao2.html

11 http://heasarc.gsfc.nasa.gov/docs/chandra/chandra.html

12 http://heasarc.gsfc.nasa.gov/docs/xmm/xmm.html

13 F. E. Christensen, A. Hornstrup, N. J.Westergaard, H. W. Schnopper, J. L.Wood, and K. Parker., A graded d-spacing multilayer telescope for high energy x-ray astronomy, Richard B. Hoover editor, Multilayer and grazing incidence X-ray/EUV optics 1546, 160–167. Proc. SPIE, 1992.

14 K. D. Joensen, F. E. Christensen, H.W. Schnopper, P. Gorenstein, J. Susini, P. Hoghoj, R. Hustache, J. L. Wood, and K. Parker. Medium-sized grazing incidence high-energy x-ray telescopes employing continuously graded multilayers. Richard B. Hoover editor, X-Ray Detector Physics and Applications 1736, 239–248, Proc. SPIE, 1993.

15 K. Yamashita, P. J. Serlemitsos, J. Tueller, S. D. Barthelmy, L. M. Bartlett, K. W. Chan, A. Furuzawa, N. Gehrels, K. Haga, H. Kunieda, P. Kurczynski, G. Lodha, N. Nakajo, N. Nakamura, Y. Namba, Y. Ogasaka, T. Okajima, D. Palmer, A. Parsons, Y. Soong, S. M. Stahl, H. Takata, K. Tamura, Y. Tawara, and B. J. Teegarden. Supermirror hard-x-ray telescope. Applied Optics, 37(34),8067–8073, 1998.

16 P. H. Mao, F. A. Harrison, Y. Y. Platonov, D. Broadway, B. Degroot, F. E. Christensen, W. W. Craig, and C. J. Hailey. Development of grazing incidence multilayer mirrors for hard x-ray focusing telescopes. Proc. SPIE, 3114, 526–534, October 1997.

17 C. J. Hailey, S. Abdali, F. E. Christensen, W. W. Craig, T. R. Decker, F. A. Harrison, and M. Jimenez-Garate. Substrates and mounting techniques for the High-Energy Focusing Telescope (HEFT). Proc. SPIE, 3114, 535–543, October 1997.

18   H. Tananbaum, N. White, and P. Sullivan, editors. Proceedings of the High Throughput X-ray SpectroscopyWorkshop. Harvard-Smithsonian Center for Astrophysics, 1996.

19   M. Lewenstein, P. Balcou, M. Y. Ivanov, A. L'Huillier, and P. B. Corkum, Theory of high-harmonic generation by low-frequency laser fields, Phys. Rev. A 49(3), 2117–2132 1994.

20   N. A. Papadogiannis, B. Witzel, C. Kalpouzos, and D. Charalambidis, Observation of Attosecond Light Localization in Higher Order Harmonic Generation, Phys. Rev. Lett. 83(21), 4289–4292 (1999).

21   P. M. Paul, E. S. Toma, P. Breger, G. Mullot, F. Aug, P. Balcou, H. G. Muller and P. Agostini, Observation of a Train of Attosecond Pulses from High Harmonic Generation Science 292(5522), 1689–1692 (2001).

22   M. Drescher, M. Hentschel, R. Kienberger, M. Uiberacker, V. Yakovlev, A. Scrinzi, T. Westerwalbesloh, U. Kleineberg, U. Heinzmann, and F. Krausz, Time-resolved atomic inner-shell spectroscopy, Nature 419, 803–807 (2002).

23   R. Kienberger, M. Hentschel, M. Uiberacker, C. Spielmann, M. Kitzler, A. Scrinzi, M. Wieland, T. Westerwalbesloh, U. Kleineberg, U. Heinzmann, M. Drescher, and F. Krausz, Steering Attosecond Electron Wave Packets with Light, Science 297(5584), 1144–1148 (2002).

24   M. Hentschel, R. Kienberger, C. Spielmann, G. A. Reider, N. Milosevic, T. Brabec, P. Corkum, U. Heinzmann, M. Drescher, and F. Krausz, Attosecond metrology, Nature 414, 509 (2001).

25   G. Lambert, B. Carr, M.-E. Couprie, D. Garzella, A. Doria, L. Giannessi, T. Hara, H. Kitamura, and T. Shintake, Seeding High Gain Harmonic Generation with Laser Harmonics produced in Gases, Proc. of EPAC 363–365 (2004).

26   R. Lopez-Martens, K. Varju, P. Johnsson, J. Mauritsson, Y. Mairesse, P. Salieres, M. B. Gaarde, K. J. Schafer, A. Persson, S. Svanberg, C.-G. Wahlstrom, and A. L'Huillier, Amplitude and Phase Control of Attosecond Light Pulses, Physical Review Letters 94(3),(2005).

27   I. L. Beigman, A. S. Pirozhkov, and E. N. Ragozin, Reflection of few-cycle x-ray pulses by aperiodic multilayer structures, J. Opt. A: Pure Appl. Opt 4, 433–439 (2002).

Chapter 2: General aspects related to the multilayer coatings interaction with radiations

2.1 Optical constants in the EUV spectral region

In the EUV region to describe the radiation we need to use the complex refractive index such as:

$$\tilde{n} = n - i\beta = (1 - \delta) - i\beta \qquad (2.1)$$

where n and β are the material optical constants, β is the imaginary term (*extinction coefficient*) and establish the wave absorption, n is the real term correspond to the *refractive index* , i.e. is related to the change in the wave group velocity when the radiation pass trough the interface between the vacuum and the material.

After to have defined the optical constants, we can now describe an electromagnetic wave with a wavelength in the soft X-ray, with angular frequency ω_0, travelling through a medium with complex refractive index $\tilde{n}$, such as its electric field:

$$E(t) = e^{-j(Kx-\omega_0 t)} = e^{-j\left(\frac{2\pi}{\lambda_0}\tilde{n}x - \omega_0 t\right)} = e^{-x\beta\frac{2\pi}{\lambda_0}} \cdot e^{-j\left(\frac{2\pi}{\lambda_0}nx - \omega_0 t\right)} = e^{-xk_0\beta} \cdot e^{-j(k_0 nx - \omega_0 t)} \qquad (2.2)$$

where K_0 is the wave vector in the vacuum media.

In the equation (2.2) the term $e^{-xk_0\beta}$ takes into account the waves absorption, and the term $e^{-j(k_0 nx - \omega_0 t)}$ is a wave propagating in a media with refractive index n. The dielectric function $\varepsilon(\omega)$ is such therefore $\tilde{n} = \sqrt{\varepsilon(\omega)}$ is the media response at the radiation field. In this function are substantially recorded all the effects of the materials aggregate nature like chemical bound and the collective excitations (phonons, etc); in x-ray fields the energies of this effects are negligible respect the other ones of the incident radiation.

The electronic excitation regard generally the atomic internal shields that is negligibly affected by the field of the other atoms because is shielded by the external shields. The electrons valence are considered free electrons in the radiation interactions in the XUV spectral range, this because they have energy amounts negligible respect the other ones of the incident wave. Considering the previous hypothesis the dielectric function (and consequently the refractive index) depend only by the atomic composition and material density. It is possible therefore write:

$$\tilde{n} = 1 - \frac{r_e\lambda^2}{2\pi} N_a \sum_i n_i f_i$$

$$n = 1 - \frac{r_e\lambda^2}{2\pi} N_a f_1 \qquad (2.3)$$

$$\beta = \frac{r_e\lambda^2}{2\pi} N_a f_2$$

where:

- $r_e = e^2/(mc^2)$ is the classic electron radius

- N_a is the atomic density

- n_i is the atomic number of the i-th element present in the compound

- $f_i = f_{i1} - jf_{i2}$ is the diffusion atomic factor of the i-th element that is given by the ratio among the diffuse amplitude of the atom and the one that should be diffuse by the single atom. The f_1 and f_2 are the atomic scattering factors which account for: f_1 is the real part related to the number of electron not involved in bonds (like they were free in the material), while the f_2 accounts for the absorption.

These equations (2.3) are only approximation which worth only for a wavelengths shorter than a value around 40 nm and longer than 0.041 nm (corresponding to and energy going from 30 eV up to 30 keV). In this region the energy is enough high to consider negligible the interaction with the valence electron and the optical response could be well approximated considering the interaction only without the inner electrons. The macroscopic effect can be seen as the sum of the each atom response. At longer wavelength this approximation cannot be done because the interaction with valence electron became significant. The atomic scattering factors can be retrieved through experimental measures in the cross section of the elementary matter [1] and nowadays many database are available with the atomic scattering factor to obtain both the refractive index and the extinction coefficient, above all worth to mention the "Center for X-Ray Optics" [2] database of the Lawrence Berkley National Lab. and of the "Lawrence Livermore National Laboratory". Nevertheless the optical constants in the EUV are very sensitive as well, explained by the [2,3], to the density of the material which is usually determined by the making process of the material, hence, especially for thin films, an accurate determination of the optical constants or a literature review has always to be made.

2.2 Reflection and transmission of a multilayer coating [3-5]

I have reported the main parts from [5].

First of all, the behavior of a plane electromagnetic wave at an idealize interface has been considered. In Fig. 1 a schematic of the abrupt interface between two semi-infinite media, the complex refraction index $\tilde{n} = n - i\beta$ is given in the two regions as $\tilde{n}_i$ and $\tilde{n}_j$. The incident wave vector, with electric field $\tilde{E}_i$, makes an angle θ_i with respect to the interface normal (the z axis). The amplitude of the reflected and transmitted electric fields, $\tilde{E}'_i$ and $\tilde{E}_j$, respectively, are given by the well-known Fresnel equations:

$$\frac{\left|\tilde{E}'_i\right|}{\left|\tilde{E}_i\right|} = \frac{\tilde{n}_i \cdot \cos\theta_i - \tilde{n}_j \cdot \cos\theta_j}{\tilde{n}_i \cdot \cos\theta_i + \tilde{n}_j \cdot \cos\theta_j} \equiv r^s_{ij} \qquad (2.4)$$

and

$$\frac{\left|\tilde{E}_j\right|}{\left|\tilde{E}_i\right|} = \frac{2 \cdot \tilde{n}_j \cdot \cos\theta_j}{\tilde{n}_i \cdot \cos\theta_i + \tilde{n}_j \cdot \cos\theta_j} \equiv t^s_{ij} \qquad (2.5)$$

for s-polarization (i.e. $\tilde{E}$ perpendicular to the plane of incidence); and
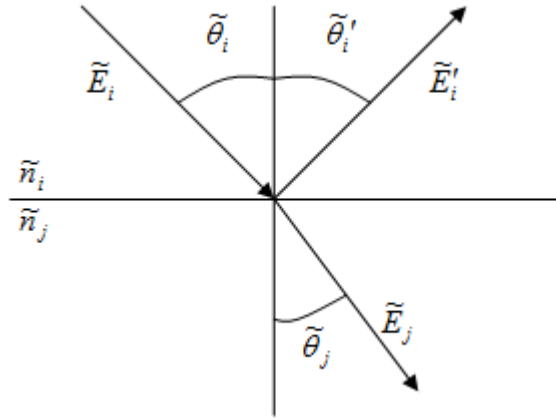
$$\frac{\left|\tilde{E}'_i\right|}{\left|\tilde{E}_i\right|} = \frac{\tilde{n}_i \cdot \cos\theta_j - \tilde{n}_j \cdot \cos\theta_i}{\tilde{n}_i \cdot \cos\theta_j + \tilde{n}_j \cdot \cos\theta_i} \equiv r_{ij}^p \tag{2.6}$$

and

$$\frac{\left|\tilde{E}_j\right|}{\left|\tilde{E}_i\right|} = \frac{2 \cdot \tilde{n}_i \cdot \cos\theta_i}{\tilde{n}_i \cdot \cos\theta_j + \tilde{n}_j \cdot \cos\theta_i} \equiv t_{ij}^p \tag{2.7}$$

for p-polarization (i.e., $\tilde{E}$ parallel to the plane of incidence), where θ_j is the angle of refraction, determined from Snell's law:

$$\tilde{n}_i \cdot \sin\theta_i = \tilde{n}_j \cdot \sin\theta_j. \tag{2.8}$$

Fig. 1 Schematic of the abrupt interface between two semi-infinite media.

In order to account for the loss in specular reflectance due to interface imperfections (i.e., interfacial roughness and/or diffuseness), the case where the change in index across the interface is not abrupt has been considered, but can be described instead by an interface profile function *p(z)* (see Fig. 2).

That is, following the formalism developed by Stearns [6] , *p(z)* as the normalized has been defined, average value along the z direction of the dielectric function, $\varepsilon(\tilde{x})$:

$$p(z) = \frac{\iint \varepsilon(\tilde{x})dxdy}{(\varepsilon_i - \varepsilon_j) \cdot \iint dxdy}, \tag{2.9}$$

Where

$$\varepsilon(\tilde{x}) = \begin{cases} \varepsilon_i, & z \to +\infty \\ \varepsilon_j, & z \to -\infty \end{cases} \tag{2.10}$$

Stearns has shown that in the case of a non-abrupt interfaces, the resultant loss in specular reflectance can be approximated by multiplying the Fresnel reflection coefficients (equations (2.4) and (2.6)) by the function $\tilde{w}(s)$, the Fourier transform of *w(z)=dp/dz*. That is, the modified Fresnel reflection coefficients are

given by $r'_{ij} = r_{ij} \cdot \tilde{w}(s_i)$

(2.11)

where $s_i = 4 \cdot \pi \cdot cos\theta_i / \lambda$, and λ is the light wavelength.

Note that the loss in specular reflectance depends only on the average variation (over x and y) in index across the interface. Consequently, the reflectance can be reduced equally well by either a rough interface, in which the transition between the two materials is abrupt at any point (x,y), or a diffuse interface, in which the index varies smoothly along the z direction (or by an interface that can be described as some combination of the two cases).

The width of each interface profile function is characterized by the parameter σ (see Fig. 2), which is a measure of either an rms interfacial roughness, in the case of a purely rough interface, an interface width, in the case of a purely a diffuse interface, or some combination of the two properties in the case of an interface that is both rough and diffuse; it is the parameter σ (along with the choice of interface profile function) that is specified to account for the effects of interface imperfections using the modified Fresnel coefficient approach.
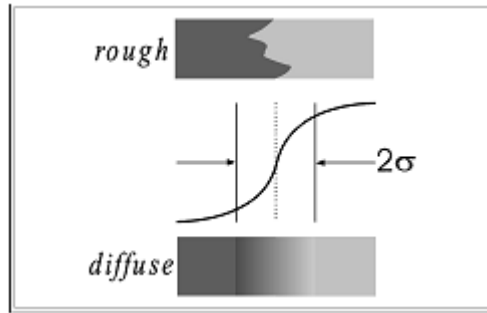
Fig. 2 *Schematic of the differences among the diffusion and roughness for the interfaces.*

The σ parameter can be incorporated in the Fresnel equation simply multiplying the (2.4) and the (2.5) by the Debye-Waller factor:

$$Debye\ Waller\ factor = e^{-2 \cdot \left(\frac{2 \cdot \pi \cdot \sigma_{ij} \cdot cos\theta_i}{\lambda} \right)^2}$$

(2.12)

and obtain the total reflected intensity R summing the square root of the Fresnel coefficient:

$$R = \frac{|r_s|^2}{2} + \frac{|r_p|^2}{2} = \frac{1}{2}R_s + \frac{1}{2}R_p$$

(2.13)

Now, the method for calculate the reflection of a several layer can be easily deduced extending the Fresnel coefficient to a multilayer structures.

First of all to understand when we want to build a multilayer made of two different material we can take into considerations the optical contrast just writing the Fresnel coefficient in the (2.13) for normal incidence i.e. $\tilde{\theta}_i = 0$:

$$R = \frac{(\delta_1 - \delta_2)^2 + (\beta_1 - \beta_2)^2}{4} \tag{2.14}$$

In this way we can see the reflectance value at the materials interface. To get a very high reflectance would necessary to find two materials with different optical constants. From the tabled value of atomic scattering factor for Mo/Si for example we can find out a value of R= 1.9 x 10^{-1} at 41 nm ($\approx$ 30 eV) and of R= 1.6 x 10^{-3} at 13.5 nm. But when we build a multilayer with more than two layer we can improve the overall reflectance by means of the interference effect of the reflected wave at each interface. In an ideal multilayer the materials constituting the interfaces are homogeneous, that means that the sum of the secondary waves diffracted at any point of the material give negligible contributes (see Fig. 3) we can now not consider the Debye-Waller factor).
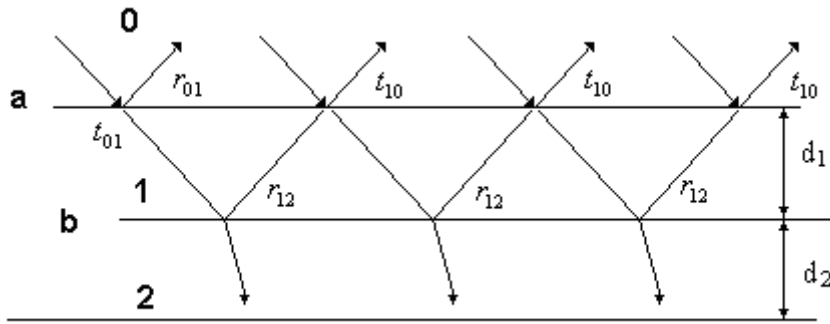
Fig. 3 A schematic behaviour of a three phase optical system: substrate (2), thin film (1), environment (0); or a multilayer made two different materials: material "a" (2), material "b" (1) and environment (0).

We take a multilayer made by the material 1 of thickness d_1 the material 2 with a thickness d_2 with $\tilde{n}_1$, $\tilde{n}_2$ the respective complex refraction index (see Fig. 3) the phase delay Φ of the wave from the interface (01) and that from the interface (12) is:

$$\phi = \frac{2\pi}{\lambda} \tilde{n}_1 t_1 \cos(\theta_1). \tag{2.15}$$

The total reflection of a wave by the thin layer is therefore the sum of the infinite reflections:

$$r = r_{01} + t_{01} t_{10} r_{12} e^{-2i\phi} \sum_{j=0}^{\infty} \left[r_{10} r_{12} e^{-2i\phi} \right]^j \tag{2.16}$$

and solving the geometric series we obtain:

$$r = r_{01} + \frac{t_{01} t_{10} r_{12} e^{-2i\phi}}{1 - r_{10} r_{12} e^{-2i\phi}}. \tag{2.17}$$

Posing $r_a = r_{01} = -r_{10}$ and $r_b = r_{12}$ and using the relationship

$$t_{ij} t_{ji} + r_{ij}^2 = 1 \tag{2.18}$$

we obtain:

$$r = \frac{r_a + r_b e^{-2i\phi}}{1 + r_a r_b e^{-2i\phi}} \qquad (2.19)$$

2.3   Standing wave distribution of a multilayer coating [5]

I have reported the main parts from [5].

When the EUV radiation interacts with a multilayer structure, the superposition of the incident and reflected fields generates a standing wave. This phenomenon can be studied for understanding the suitable thickness of absorbing materials in periodic and aperiodic multilayers.

In order to compute the standing wave intensity as a function of depth in a multilayer stack we consider the interface between the i-th and the j-th layers in a multilayer stack, where we now have both positive-going and negative-going electromagnetic plane waves in both layers. Solving Maxwell's equations in this case, we can show that the positive-going and negative-going field amplitudes at a distance z_i above the interface are given by:

$$E_i^+(z_i) = \frac{1}{t_{ij}} \cdot e^{-i\beta_i(z_i)} \cdot E_j^+(0) + \frac{r_{ij}}{t_{ij}} \cdot e^{-i\beta_i(z_i)} \cdot E_j^-(0) \qquad (2.20)$$

and

$$E_i^-(z_i) = \frac{r_{ij}}{t_{ij}} \cdot e^{-i\beta_i(z_i)} \cdot E_j^+(0) + \frac{1}{t_{ij}} \cdot e^{-i\beta_i(z_i)} \cdot E_j^-(0) \qquad (2.21)$$

respectively, where $\beta_i(z_i) = 2 \cdot \pi \cdot z_i \cdot \tilde{n}_i \cdot \cos\theta_i / \lambda$, $E_j^+(0)$ and $E_j^-(0)$ are the field amplitudes at the top of the j-th layer. Again, a recursive approach can be used to compute the field amplitudes throughout the stack, starting at the bottom-most layer (i=N, j=s) with the field amplitudes in the substrate given as $E_s^+(0)$ and $E_s^-(0)$. The net reflection and transmission coefficients of the film can then be computed from the field amplitudes in the ambient:

$$r = \frac{E_a^-(0)}{E_a^+(0)}, \qquad (2.22)$$

and

$$t = \frac{1}{E_a^+(0)}. \qquad (2.23)$$

Once the transmission coefficient is computed from Eq. (2.23) the field amplitudes versus depth are then rescaled using

$$E^\pm(z) \rightarrow t \cdot E^\pm(z) \qquad (2.24)$$

~i.e., by taking the incident electric field to have unit amplitude and the field intensities for *s* and *p* polarization are computed from

$$I(z) = \left| E^+(z) + E^-(z) \right|^2 . \tag{2.25}$$

2.4   Multilayer structures design [7]

I have reported the main parts from [7] section 1.3 "Optimization techniques".

When there is a problem with one or more independent variables, it is often desirable to maximize or minimize a characteristic merit function (MF), otherwise known as optimization. The location of a maximum or minimum is found and then the maximum or minimum value of the function is calculated.

The solution space for a function to be optimized can be represent two dimensionally as in Fig. 4. If one only looks between points a and b in the Fig. 4, a minimum will be found but it is only a local minimum. From the Fig. 4 one can see that there is a deeper minimum between points b and c. Since this is the point with the lowest value for the function in the solution space, this is the global minimum.

Optimization techniques utilize information about the problem which is encoded in a merit function. As the function is changed in the search for a maximum or minimum, the merit function is recalculated and tells how good the solution is. Thus, if one is searching for a minimum, the best solution will have the highest or lowest merit function.
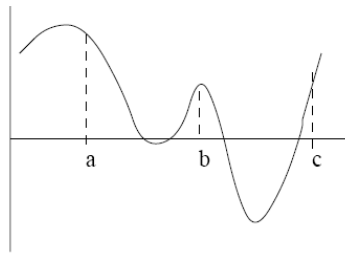
Fig. 4: representative trend of a one dimensional space solution case.

2.4.1   Local optimizers

Local optimization procedures take advantage of the decrease in value of the function near a minimum to converge to a solution. Thus, if the initial starting point is near a local minimum, that will be the solution found and there is no way of knowing about or finding better solutions. Two types of local optimizers use different approaches to take steps in the solution space: those that find the direction in which the value of the function is decreasing by blind searching and those that use information about the gradient of the solution space at a point to find a minimum. An example of this first type and one of the simplest optimization techniques is the downhill simplex method developed by Nelder and Mead and explained in *Numerical Recipes* [8]. The solution space is encoded into a simplex—a multidimensional shape. An initial guess is given and at each step in the process, one of the sides of the simplex is extended, contracted, or reflected through another side to find a minimum value. Successive steps lead to a local minima by following the direction of decreasing value. The algorithm terminates when the step taken is smaller than a

tolerance defined or the decrease in the function value at the last step is smaller than a certain tolerance. This method can be compared to someone walking in a dark cave high up in a mountain. He will feel in different directions with his feet until he finds the step that will take him lower. He then follows this method until he cannot go any lower and hopefully he has made it out of the mountain. Unfortunately, one can get stuck in a local minima, which is not the global minima. Although this method has no allowance for fixing this problem and has to have an initial point in the space given to it, it is very simple to apply.

The second type of local optimization requires the computation of derivatives. An example of this is the conjugate gradient method [8]. This approach allows one to find a local minimum quickly with the calculation of the gradient and one-dimensional sub-minimization. An initial point is chosen and the gradient is computed. Then the conjugate to this gradient is found and the direction is followed while the function is decreasing. This is repeated until a local minimum is found. The conjugate gradient method has relatively fast convergence but is not very useful when the derivative of the function to be optimized is difficult to calculate or does not exist. The simplex and conjugate gradient methods are both local optimization techniques. These methods do not handle discrete variables, discontinuities in solutions, or parameter constraints well.

In optimizing a function, one wants the best solution or global extreme rather than a local extreme.

2.4.2 Global optimizers

A global optimizer is one which samples most of the solution space and is more apt to find the global extreme rather than just a local extreme. Global optimization procedures such as simulated annealing [9-10] and genetic algorithms [11] are able to handle these difficulties well and are less sensitive to an initial guess. These global techniques begin with a random initialization and converge to a solution through a sequence of structured changes in the parameters. The randomness in movements and in the initial population allow global extreme to be found but make these methods inherently very time intensive.

2.4.3 The multilayer design approach

The design of the optimal aperiodic multilayer structure is an optimization problem with many free parameters, that are in general the layers thickness, and with a non linear function (the reflection). Consequently a global optimizers has to be used. In order to design suitable aperiodic ML a Genetic Algorithm (MATLAB toolbox) [12] has been used.

In order to improve the performances of the Genetic Algorithm, the genetic rules, for the choice of the best individuals, has been substituted by some mathematical rules properly studied for the multilayer domain; thank to this substitution the algorithm focuses toward multilayer structures that in addition to the high efficiency have stable performances varying to the layers thickness [13,14]. This mathematical rules permit the algorithm to acquire domain knowledge during the evolution and they are explained into the international patent [15] (will be public starting from April).

2.5   Multilayer fabrication [16]

I have reported the main parts from [16] chapter "Multilayer fabrication".

2.5.1   Deposition methods

Any method for the deposition of the films can be used for the fabrication of coatings for the XUV

region. Compared to coatings for visible light, the thicknesses and the permitted thickness errors are about a factor of 100 smaller, and the number of layers is typically a factor of 10 higher. Therefore, tighter control of the deposition process is required. For many coatings, the quality of the boundaries is the most important parameter for the performance of the a coating. Boundaries have to be sharp within 1/10 of the multilayer period, and the search for deposition processes which produce sharp boundaries has been a major effort in the development of coatings for the x-ray region.

The limits on the quality of the boundaries is of course determined by the size of the atoms, and some of the best boundaries reported in the literature ($\sigma \leq 3$ Å) are close to this limit. Drastic improvements over such a value could only be expected with crystalline multilayer structures, where a perfect crystalline structure is maintained throughout the entire stack.

Perfect boundaries would require that the growth of one atomic plane starts only when the previous plane is completely filled, and that one would be able to switch materials exactly at this moment.

Sputtering	Thermal evaporation
Very stable rates	Deposiotion rate can fluctuate
Thickness control by timing	Needs error compensating in-situ thickness monitor
Substrate holder rotates past sputter source	Shutter in front of sources
Good uniformity requires large deposition system chamber diameter >3 · mirror	Good uniformity over large areas
Might run unattended at high deposition rate	Diameter > mirror diameter
Kinetic energy of deposition usually larger than 100eV can be adjusted	Kinetic energy smaller than 0.5 eV not adjustable
Film surface bombarded by sputter gas ions	Ion polishimg added for smoother boundaries
	Laser plasma source has higher kinetic energy than conventional thermal source, adjustable

Table 1 Main differences between a sputter deposition system and a thermal evaporation system for the fabrication of multilayer x-ray mirrors.

Sputter deposition and thermal evaporation are the most widely used methods for the fabrication of multilayer XUV coatings, and the main differences between these system are shown in Table 1. The biggest

21

advantage of a sputter deposition system is its stability. Gas flow and power to the plasma can be very well stabilized. In the system pioneered by Barbee [17]

The substrates rotate past magnetron sputter sources, producing one film of each material for each rotation of the substrate holder.

Thickness errors well below 0.1 Å per layer have been achieved with accumulated thickness errors below 0.5 Å after the deposition of more than 100 layers.

Thermal evaporation sources cannot be stabilized at t6he level for a variety of reasons: big changes in vapor pressure for small changes in temperature; long time constants in any feedback loop due to the thermal mass of the evaporant and crucible; temperature variation over the evaporant produced by changes in the surface geometry of the evaporant. Evaporation with pulses, eliminates some of these problems, and very good multilayer mirror coatings with over 100 layers have been produced by this method [25]. Chemical vapor deposition induced by laser light has also been used to produce multilayer structures [19-20].

Successful deposition of x-ray mirrors by electron beam evaporation has bee obtained with in-situ measurements of the x-ray reflectivity of the coating during the deposition [21-24] in analogy to optical thickness monitors used for visible light. In such a monitoring system, the top surface of a growing film moves through the standing-wave field that is established in front of the film. The reflected intensity oscillates with a period that corresponds to the period in the standing-wave field assures that thickness errors do not accumulate from layer to layer; an error can always be kept below the requirements. Accumulated thickness error below 3 Å can be routinely obtained in multilayers with periods of 30 Å. In addition, the immediate feedback of an in-situ monitoring system has a great advantage when new material combinations are to be explored. Roughness of the boundaries and diffusion at the boundaries are immediately recognized [22,24].

The kinetic energy of the evaporant is a major difference between deposition n methods. For conventional thermal evaporation, the kinetic energy of the evaporant is determined by the vapor pressure curve of a material, cannot be adjusted, and is below 0.5 eV. An advantage of this low energy is that damage to the growing film is minimized. Crystallization of amorphous films can more easily be avoided for a low-energy deposition process, and amorphous films usually have better boundaries then polycrystalline films. On the other hand, bombardment of the film by higher energy particles can enhance sideways diffusion of the surface atoms and help them to settle in the valleys of the structure, thus producing smoother films. It is often desirable to add an additional source of kinetic energy to the thermal deposition system. Bombardment of the film during or after its deposition with ions has successfully been used to obtain smoother boundaries [25-27]. Higher substrate temperatures in an ultrahigh-vacuum thermal deposition system have also improved the quality of the boundaries for Mo-Si multilayer mirrors [28-32].

Laser evaporation with short light pulses can produce a plasma up to temperatures in the 10^6 degrees range; this temperature can be adjusted by pulse shape and different focusing and can be optimized to produce the smoothest films.

Within the plasma of a sputter deposition system the kinetic energy of the evaporant is usually larger than 100 eV, and in addition, the growing film can be bombarded by secondary electrons and inert gas ions and atoms. Magneton sources can decouple the growing film from the substrate and eliminate many of the negative effects of the high-energy bombardments; the energy of the evaporant can be further reduced by thermalization in an inert gas between the plasma and the substrate [17,33]. For many material combinations (Mo-Si, Rh-C, Ru-C, Ru-Si) optimized sputter deposition system have produced sharper boundaries than thermal evaporation [34].

It appears that sputtering is the method of choice when a large number of similar coatings have to be fabricated routinely. Once the optimum parameters for a material combination are determined, the deposition process can b easily automated. In contrast, the thermal deposition with in-situ monitoring requires more skill from the operator or the computer system that controls the deposition. The x-ray reflectivity is monitored continuously being used for decisions on the deposition process. The signal/noise ratio can be low at the beginning of a deposition run, when the reflectivity is low and longer deposition times per layer are needed. However, the monitor signal gives an immediate feedback on the quality of the growing structure. An increase in the roughness of the growing film is recognized as a smaller signal, and hopefully, the cause for this increase can be corrected. Thermal deposition with in-situ monitoring is the system of choice when a single, large, and expensive substrate, like the mirror of an x-ray telescope, has to be coated. X-ray mirrors with 25-cm diameter have been coated with a thickness control better than 0.5% using thermal evaporation [35-37].

2.5.2   Performance of multilayer systems

The measured performance of a multilayer can be lower than that expected from theory far several reasons:

1)   errors in the layer thickness

2)   uncertainties in the optical constants;

3)   contamination, especially of the spacer layer;

4)   mixing of the coating materials, producing smaller modulation in the optical constants; and

5)   quality of the boundary.

The last two items pose the most severe limitation if one fabricates structures with small periods. One can reduce the effect of the boundary quality on the performance by producing coarse multilayer coatings (large period) and by reaching the desired wavelengths by rotation to normal incidence. With this method one can explore the performance limit posed by the available optical constants first and can also, with one

23

coating, explore a large range of possible wavelengths by changing the incidence angle. In a second experiment, ano can produce a coating with a smaller period, and can recognize the influence of the boundary quality when comparing it with the coarser one. The drop in reflectivity for the finer coating is due to the quality of the boundaries.

2.5.3 Substrates

Requirements on the quality of the substrates for multilayer x-ray mirrors are more demanding than those for visible light; the roughness of the substrate should be smaller than 1/10 of the multilayer period. In addition, the requirements smoothness extend to considerably higher spatial frequencies. The capability for polishing and testing of surfaces [38-41] has drastically improved during the last decade; polished substrates are commercially available with roughness values $\sigma \approx 1$ Å over a range of spatial frequencies from mm^{-1} to 1 μm^{-1}. Roughness of substrate for the high spatial frequencies above 10 μm^{-1} that are important for x-rays can be obtained from x-ray reflectivity measurements; well-polished mirror substrates have roughness values below 4 Å in this range. The performance of multilayer mirrors is presently more limited bu the properties of the deposited films than by the substrate [42].

References

1   http://www-cxro.lbl.govr(ICSO), ESA-SP (European Space Agency, 2006).

2   Gullikson E.M., Charpet 13. "Vacuum Ultraviolet Spectroscopy." s.l. : Academic Press, 1998.

3   Born Wolf., *Optics.*

4   Spiller E., Charpter 14. "Vacuum Ultraviolet Spectroscopy". s.l. : Academic Press, 1998.

5   D. L. Windt, "*IMD—Software for modeling the optical properties of multilayer*"; Computers in physics **12**, 360-370 (1988).

6   Stearns D. G.; J. Appl. Phys, Vol. **65**, p. 491 (1989).

7   Shannon L.; "The Use of Genetic Algorithms in Multilayer Mirror Optimization"; Submitted to Brigham Young University in partial fulfillment of graduation requirements for University Honors (March 1999).

8   William H. Press, et. al, "Numerical Recipes in C: the Art of Scientific Computing", New York, Cambridge University Press, 1992.

9   T. Boudet, P. Chaton, L. Herault, G. Gonon, L. Jouanet, and P.Keller; "*Thin-film designs by simulated annealing*"; Applied Optics **35**, 6219-6226 (1996).

10   A. B. Djuriˇsi´c, J. M. Elazar, and A. D. Raki´c; "*Simulated-annealing-based genetic algorithm for modeling the optical constants of solids*" *Applied Optics* **36**, 7097-7103 (1997).

11   J. M. Johnson and Y. Rahmat-Samii; "*Genetic Algorithms in Engineering Electromagnetics*"; *IEEE* Antennas and Propagation Magazine **39**, 7-21 (Aug 1997).

12   Christopher R. Houck, Jeffery A. Joines and M. G. Kay; "A Genetic Algorithm for Function Optimization: A Matlab Implementation"; http://www.ise.ncsu.edu/mirage/GAToolBox/gaot/ .

13   M. Suman, F. Frassetto, P. Nicolosi and M.-G. Pelizzo, "*Design of a-periodic multilayer structures for attosecond pulses in the EUV*" Appl. Opt. **46**(33), 8159-8169 (2007).

14   M. Suman, M.-G. Pelizzo, P. Nicolosi, and D. L. Windt; "*Aperiodic multilayers with enhanced reflectivity for extreme ultraviolet lithography*"; Appl. Opt. **47**, 2906-2914 (2008).

15   M. Suman, M.-G. Pelizzo, P. Nicolosi, and D. L. Windt; PCT/EP2007/060477.

16   E. Spiller; "Soft X-Ray Optics"; SPIE-The international Society for Optical Engineering (1994).

17   T.W. Barbee Jr., "*Multilayers for x-ray optics*", Opt. Eng. **25**, 893-915 (1986).

18   S.V. Gapanov, F. V. Garin, S. A. Gusev, A. V. Kochemasov, Y. Y. Platonov, N. N. Salashenko and E. S. Gluskin, "*Multilayer mirrors for soft x-ray and VUV radiation*", Nucl. Instrum. And Meth. **208**, 227-231 (1983).

19   S. Masataka, S. Seki, Y. Ishino, H. Nagata and Y. Suzuki; "*Fabrication and evaluation of x-ray multilayer mirrors prepared by laser-induced chemical vapor deposition technique*"; Jpn. J. Apll. Phys. **31**, 1219-1224 (1992).

20   Y. Yamada, K. Mutoh, T. Iwabuchi and T. Miyata; "*Fabrication of tungsten carbon multilayers for soft x-ray optics using excimer laser induced chemical vapor deposition technique*"; Jpn. J. Apll. Phys. 1 Regul. Pap. Short Notes, **31** 982-986 (1992).

21   E. Spiller, A. Segmüller, J. Rife and R.-P. Haelbich; "*Controlled fabrication of multilayer soft x-ray mirrors*"; Appl. Phys. Lett. **37**, 1048-1050 (1980).

22   E. Spiller; "Experience with the in situ monitor system for the fabrication of x-ray mirrors"; Proc. SPIE **563**, 367-375 (1985);

23   M. P. Bruijn, P. Chakraborty, H. W. van Essen, J. Verhoeven and M. J. van der Weil, "*Autmatic electron beam deposition of multilayer soft x-ray coatings with laterally graded d spacing*"; Opt. Eng. **25**, 916-921 (1986).

24   J. P. Chauvineau; "*Soft x-ray reflectometry applied to the evaluation of surface roughness variation during the deposition of thin films*"; Revue Phys. Apll. **23**, 1645-1652 (1988).

25   E. Spiller; "*Enhancement of the reflectivity of multilayer x-ray mirrors by ion polishing*"; Opt. Eng. **29**, 609-613 (1986).

26   E. j. Puik, M. J. van der Wiel, H. Zeijlemaker and J. Verhoeven; "*Ion etching of thin W layers: enhanced reflectivity of W-C multilayer coatings*"; Appl. Surface Science **47**, 63-76 (1991).

27   A. Kloidt, H. J. Stock, U. Kleinenberg, T. Dohring, M. Propper, B. Schmiedesskamp and U. Heinzmann; "*Smoothing of interfaces in ultrathin Mo/Si multilayers by ion-bombardment*"; Thin Solid Films **228**, 154-157 (1993).

28   J. Slaughter, M. Burkland, P. Kearney, A. Lampis, Z. Milanovic, D. Schulze, C. Falco, J. Roberts, J. Kerner and E. Salomon; "*Multilayer mirrors for 182 Å*"; Proc. SPIE **1160**, 235-241 (1989).

29   M. Sudoh, R. Yokyama, M. sumiya, M. Yamamoto, M. Yanagihara and T. Namioka; "*Soft x-ray multilayers fabricated by electron-beam deposition*"; Opt. Eng. **30**, 1061-1066 (1991).

30   A. Kloidt, K. Nolting, U. Kleinenberg, B. Schmiedesskamp, U. Heinzmann, P. Müller and M. Kühne; "*Enhancememnt of the reflectivity of Mo/Si multilayer x-ray mirrors by thermal treatment*"; Appl. Phys. Lett. **58**, 64-67 (1991).

31   E. Louis, H. J. Voorma, N. B. Koster, L. Shmaenok, R. Schlatmann, J. Verhoeven, Y. Y. Platonov, G. E. van Dorssen and H. A. Padmore; "*Enhancememnt of reflectivity of multilayer mirrors for soft x-ray projection lithography by temperature optimization and ion bombardment* "; Proc. Microcircuit Eng. **23**, 215-218 (1994).

32   B. Schmiedesskamp, A. Kloidt, H. J. Stock, T. Döhring, M. Pröpper, S. Rahn, K. Higers, B. Heidemann, T. Tappe, U. Heinzmann, M. K. Krumrey, P. Müller, F. Scholze and K. F. Heidemann; "*Electron-beam deposited Mo/Si and Mo multilayer x-ray mirrors and gratings*"; Opt. Eng. **33**, 1314-1321 (1994).

33   T. W. Barbee, Jr., "*Multilayer optics for the soft x-ray and extreme ultraviolet*"; MRS Bulletin **15(2)**, 37-44 (1990).

34   S. Ogura, M. Niibe, Y. Watanabe, M. and T. Iizuka; "*Comparison among multilayer sift x-ray mirrors fabricated by electron beam, dc-, rf- magneton sputtering and ion bema deposition*"; Proc. SPIE **984**, 140-148 (1988).

35   C. J. Hayden and E. Spiller; "*Large area coatings with uniform thickness fabrication in a small vacuum chamber*"; Appl. Opt. **28**, 2694-2696 (1989).

36   E. Spiller and L. Golub; "*Fabrication and testing of large area multilayer coated x-ray optics*"; Appl. Opt. **28**, 2969-2974 (1989).

37   E. Spiller, J. Wilczynski, L. Golub and G. Nystrom; "The *normal incidence soft x-ray, λ=63.5 Å telescope of 1991*"; Proc. SPIE **1546**, 168-174 (1991).

38   S. R. Lange; "*Very high resolution profiler for Diamond turning groove analysis*"; Proc. SPIE **1160**, 263-270 (1989).

39   B. E. Truax; "*Absolute interferometric testing of spherical surfaces*"; Proc SPIE **966**, 263-270 1989.

40   J. M. Bennett and L. Mattson "Introduction to Surface Roughness and scattering"; Optical Soc. Am. Washington (1990).

41   P.C. Barker; "*Advanced flow-polishing of exotic optical materials*"; Proc. SPIE **1160**, 23-270 (1989).

42   E. Spiller, D. G. Stearns and M. Krumrey; "*Multilayer x-ray mirrors: Interfacial roughness, scattering, and miage quality*"; J. Appl. Phys. **74**, 107-118 (1993).

Chapter 3: Innovative design of EUV Multilayer reflective coating for improved spectral filtering in solar imaging

3.1   Introduction

In recent years telescopes based on near normal-incidence multilayer mirror technology have been employed in many missions dedicated to the Sun observation in EUV wavelengths, as in particular Fe-IX (17.1 nm), Fe-XII (19.5 nm), Fe-XV (28.4 nm) and He-II (30.4 nm).

Examples of successful missions are SOHO (EIT) [1] and TRACE [2]. The performances of the multilayer optics in this applications are mainly evaluated in terms of peak reflectivity at working wavelength and rejection capability of unwanted lines.

The Mo/Si material couple is conventionally used into the multilayer stack, also at these relatively long wavelengths, for their high stability, even if they have relatively low reflectivity peak with respect to other material couples. Moreover, in case of a Mo/Si periodic structure optimized at 28.4 nm, the reflectivity curve is quite spectrally broad and includes the strong HeII line, that can affect diagnostic with the Fe line signal. A suitable narrowband solution which cuts down the HeII reflection has been obtained through an a-periodic ML structure design [3]. Moreover, further enhancement of peak reflectivity can be obtained using other material combinations like Mg/SiC [4], $B_4C/Si/Mo$ [5] or B_4C/Si [4]. Although for some of these structures, test and proof of lifetime stability must be investigated.

In this PhD work has been developed an innovative method for designing suitable capping layer covering the multilayer structure which do not affect the reflectivity peak while rejecting unwanted emission, for example from relatively close lines. The capping layer solution can be adopted both in case of periodic and a-periodic multilayer, made by different materials. The capping layer can be realized using a ML structure of different materials, for example to get additional mechanical or optical properties, as the capability of surviving in harsh environmental space conditions or to suitably reject visible/UV spectral ranges.

In this chapter both the mathematical tool and the theoretical results for some optimized structures will be presented and discussed. In conclusion experimental results related to periodic Mo/Si multilayer covered by an optimized Mo/Si capping layer able to reflect the Fe-XV line with rejection ratio of some orders of magnitude for the near He-II intense line will be presented.

3.2   Design of multilayer coating with improved spectral filtering

The innovative basic idea is to take advantage of the e.m. field standing wave configuration generated in the multilayer structure by the superposition of incident and reflected fields. As already pointed out in [6], the last protective layer in a multilayer structure can be   grown at the node-position of the standing wave field intensity distribution in the multilayer. In fact, by suitable design of the last uppermost layers it is possible to shift the standing wave distribution at the top of the multilayer. In this way the performance of the structure result essentially insensitive to the cap-layer characteristics.

Let's now consider two wavelengths, the first λ_{peak} is the "useful" wavelength and the second λ_{noise} is the wavelength to be rejected. ML (multilayer) is the coating sub-structure constituted by the repetition of two or more materials designed in order to obtain the best reflectivity peak at the λ_{peak} wavelength and CL (capping layer) is the structure made of last layers covering the ML, which is designed in order to preserve the λ_{peak} wavelength signal and suppress the λ_{noise} wavelength signal (see Fig. 1).
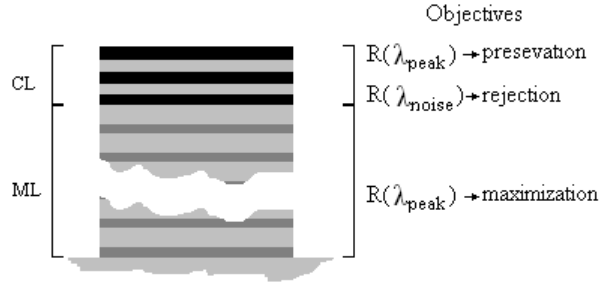
Fig. 1 *A schematic view of the conceptual subdivision between CL and ML and of their performance.*

The CL structure, like the ML structure, is constituted by a sequence of absorber and spacer materials (see Fig. 1), the materials can be the same or different from the ones in the ML, in any case their thickness must be suitably optimized.

The optimization design sequence of an optimal structure consists of the following steps (see Fig. 2):

1) design of the ML (periodic or a-periodic) in order to have the maximum reflectivity peak at λ_{peak}

2) computation of the standing wave in the ML structure for λ_{peak} wavelength, and also computation of the standing wave in the ML structure at λ_{noise} wavelength

3) optimization of the thicknesses and the number of the CL layers by growing the absorber layers into the λ_{peak} standing wave nodes in order to preserve the reflectivity at the λ_{peak} wavelength and as close as possible to the anti-nodes of the λ_{noise} standing wave in order to efficiently reject the contribution at this wavelength

4) finally we optimize the CL layers and the ML period and γ parameters in order to improve the ratio $R(\lambda_{peak})/R(\lambda_{noise})$ while keeping high peak reflectivity.

By Positioning the absorber layers into the standing wave node we minimize the detrimental radiation extinction effect at the λ_{peak} wavelength almost preserving the same reflectivity peak of the ML structure. At the same time, due to the different standing wave behavior at different wavelengths, we can have an higher radiation extinction at the λ_{noise} wavelength than at the λ_{peak} one.
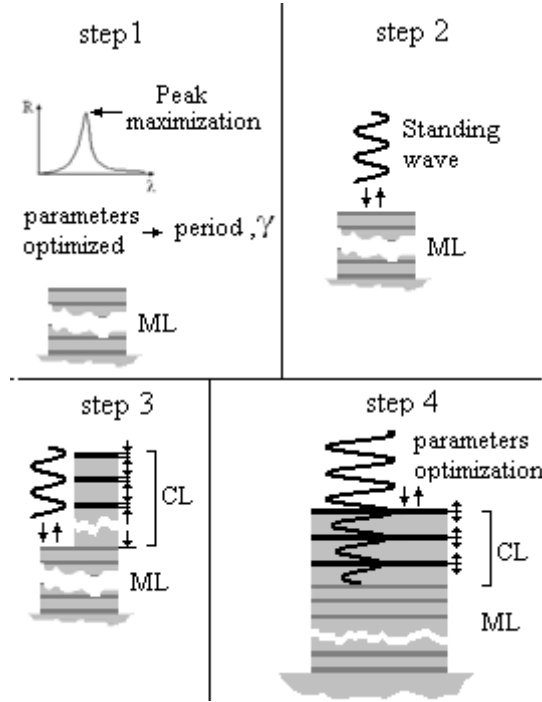
Fig. 2 *A schematic of the sequence of steps followed for the multilayer optimization, here , for clarity, only the standing wave at λ_{peak} is shown. Step 1, ML design; step 2, Fields computation; step 3, CL design; step 4, optimization.*

Case	ML materials	CL materials	λ_{peak}	λ_{noise}
1	Mo/Si	W/Si	33.5	30.4
2	Mo/Si	Pt/Si	28.4	30.4
3	Mo/Si	Cr/Si	28.4	30.4
4	Mo/Si	Mo/Si	28.4	30.4

Table 1: *column 1, the index of the different cases, column 2 and 3, respectively the ML and CL materials, in column 4 and 5, respectively the λ_{peak} and λ_{noise} wavelengths in nm.*

3.3   Simulation of some applications

Different structures have been designed for reflecting the 33.5 nm or the 28.4 nm lines while rejecting the strong 30.4 nm one. These structures are based on Mo/Si ML structures with different CL, and are reported in Table 1. In this section we show and discuss the theoretical simulations, performed with IMD program [7]. The considered cases can be very interesting for example for GOES-R mission [8].

3.3.1   Case 1

Mo/Si ML with W/Si CL working at 33.5 nm with high rejection at 30.4 nm have been designed. The W absorption coefficient is reported in Fig. 3, it shows a very high extinction at both wavelengths of interest, in addition thin W layer deposition has been already tested for ML structures for X-ray mirrors.

In Table 2 the structure of the optimized multilayer is reported. In Table 3 and in Fig. 4 the performance of the optimized structure is compared with the performance of a standard Mo/Si periodic multilayer. The new

design shows a peak reflectivity loss of 2.6% in absolute percentage with respect to the standard periodic ML but with a considerably improved, about two orders of magnitude, rejection ratio.
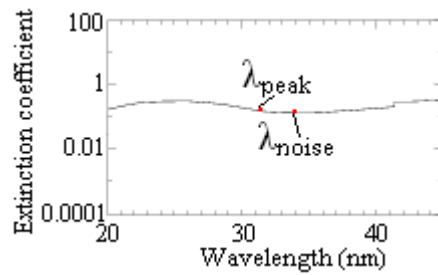
Fig. 3 *The behavior of the W extinction coefficient in the 20-45 nm spectral range.*
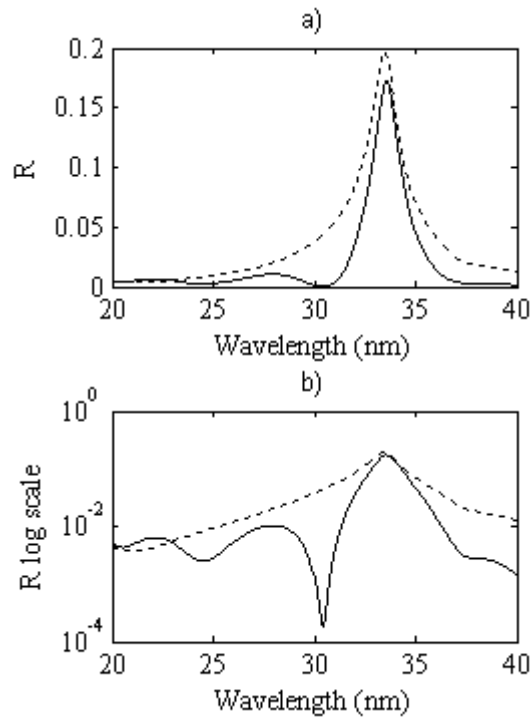
Fig. 4 *In the case a) The reflectivity behavior of the optimized multilayer with a W/Si CL, continuous curve, compared with the performance, dashed line, of a standard periodic multilayer optimized only for the λ_{peak} wavelength. In the case b) the same data of the case a) reported in log scale. The reflectivity is optimized and calculated at 5° normal incidence.*

CL Structure	Value
W	2.0 nm
a-Si	16.5 nm
W	2.2 nm
a-Si	16.5 nm
W	2.0 nm
ML structure	Value
Period (a-Si/Mo)	18.2 nm
Ratio	0.89
Period number	35

Table 2 *The structure of the optimized multilayer for case 1.*

	$R_{33.5 \, nm}$	$R_{30.4 \, nm}$
Standard periodic	0.197	0.044
Optimized ML+W/Si CL	0.171	$1.79*10^{-4}$

Table 3 *Columns 2 and 3, respectively the reflectivity at the λ_{peak} and λ_{noise} wavelengths for the case 1.*

3.3.2   Case 2

The next three cases are based on Mo/Si ML structures with different CL, designed in order to reflect at 28.4 nm with the highest rejection at 30.4 nm.

In this case a Pt/Si CL has been designed. Pt has been chosen because it is a very suitable CL absorber material for this spectral region (see Fig. 5).

CL Structure	Value
Pt	2.2 nm
a-Si	13.4 nm
Pt	2.0 nm
a-Si	12.8 nm
Pt	2.0 nm
a-Si	11.6 nm
Mo	2.0 nm
ML structure	Value
Period (a-Si/Mo)	15.3 nm
Ratio	0.87
Period number	35

*Table 4.* *The structure of the optimized multilayer for case 2.*

The structure is reported in Table 4, in Table 5 and in Fig. 6 the performance of the optimized multilayer are compared with a Mo/Si periodic multilayer designed in order to reflect the 28.4 nm wavelength. In this case we have obtained a reflectivity loss of 4% in absolute percentage but with improved rejection of about three orders of magnitude.

	$R_{28.4\ nm}$	$R_{30.4\ nm}$
Standard periodic	0.25	0.045
Optimized ML + Pt/Si CL	0.21	$6.7*10^{-5}$
Optimized ML + Cr/Si CL	0.2	$3*10^{-5}$
Optimized ML + Mo/Si CL	0.196	$2.62*10^{-5}$

Table 5 *Columns 2 and 3, respectively the reflectivity at the λ_{peak} and λ_{noise} wavelengths for cases 2,3,4.*
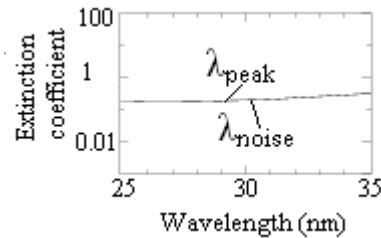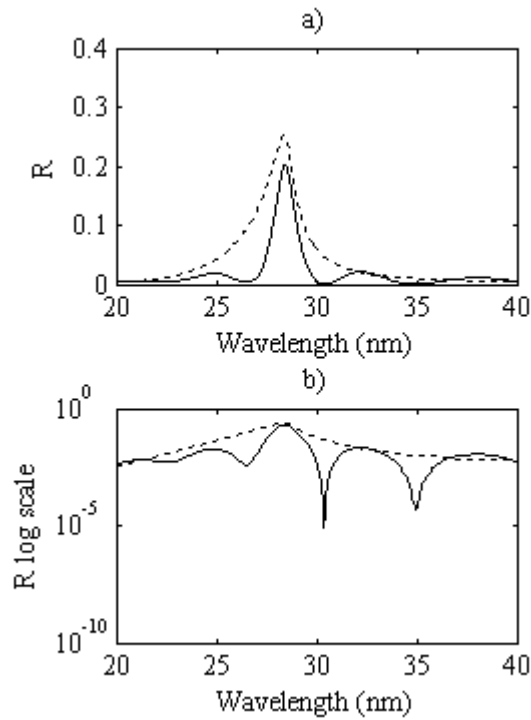

Fig. 5 *Pt extinction coefficient in the 25-35 nm spectral range.*
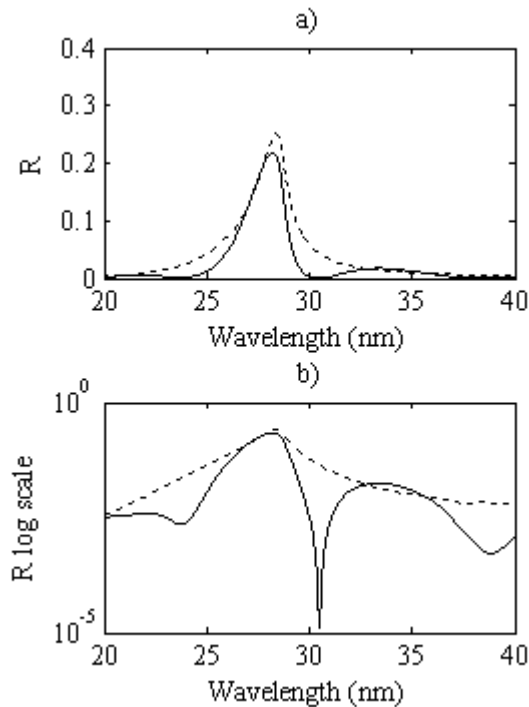
Fig. 6 *In the case a) The reflectivity behavior of the optimized multilayer with a Pt/Si CL, continuous curve, compared, with a standard periodic multilayer optimized for the λ_{peak} wavelength, dashed line. In the case b) the same data of the case a) reported in log scale. The reflectivity is optimized and calculated at 5° normal incidence.*

CL Structure	Value
Cr	3.2 nm
a-Si	12.3 nm
Cr	3.05 nm
a-Si	12.6 nm
Cr	2.9 nm
a-Si	12.8 nm
Cr	2.7 nm
a-Si	13.1 nm
Cr	2.5 nm
a-Si	12.1 nm
Mo	2.0 nm
ML structure	Value
Period (a-Si/Mo)	15.2 nm
Ratio	0.87
Period number	35

Table 6 *The structure of the optimized multilayer for case 3.*

Fig. 7 *In the case a) The reflectivity behavior of the optimized multilayer with a Cr/Si CL, continuous curve, compared with, a standard periodic multilayer optimized for the λ_{peak} wavelength, in dashed line. In the case b) the same data of the case a) reported in log scale. The reflectivity are optimized and calculated at 5° normal incidence.*

3.3.3   Case 3

33

The next two cases have been chosen in order to have an easier deposition procedure, i.e. with a lower number of sputtering target materials.

In this case a Cr/Si CL has been adopted. A Cr adhesion layer between the substrate and the multilayer can be grown in order to avoid any adhesion failures, moreover, the Cr layer tends to absorb surface contaminants on the substrate, and it also has tensile stress which balances the large compressive stresses in the multilayer. The high stress in the multilayer is due to high gamma ratio (γ) value of the Si/Mo coatings optimized for this spectral region.

In this case the Cr material has been used both like CL absorber layer and adhesion layer, this in order to permit the deposition of an optimized multilayer structure by utilizing a magnetron sputtering deposition system with only three cathodes.

Cr doesn't show the best property as candidate for the CL structure, in particular the absorption is lower than for the Pt or Mo cases. For this reason in the optimization process the Cr layers are slightly displaced with respect to the 28.4 nm standing wave nodes. The new positions give the best ratio value between the standing wave area into the CL structure at the 28.4 nm and 30.4 nm wavelengths.

The resulting structure is reported in Table 6, we highlight the high number of CL layers necessary to obtain a high enough rejection, due to the low absorption of Cr. The resulting performance is reported in Table 5 and in Fig. 7

3.3.4   Case 4

In this last case only Mo and Si have been taken into account as possible materials both for the ML and CL structures.

CL Structure	Value
a-Si	14.7 nm
Mo	2.2 nm
a-Si	57.75 nm
Mo	2 nm
ML structure	Value
Period (a-Si/Mo)	151.5 nm
Ratio	0.868
Period number	35

Table 7 *The structure of the optimized multilayer for case 4.*
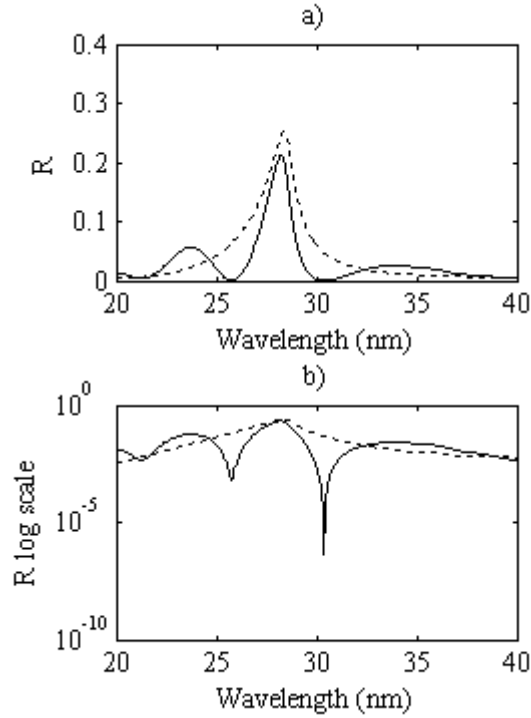
Fig. 8 *In the case a) The reflectivity behavior of the optimized multilayer with a Mo/Si CL, continuous curve, compared with the performance, of a standard periodic multilayer optimized for the λ_{peak} wavelength, dashed line . In the case b) the same data of the case a) reported in log scale. The reflectivity are optimized and calculated at 5° normal incidence.*

Mo has a relevant absorption coefficient in this spectral region, it assures a good time stability coupled with Si, only one Mo layer for the CL structure placed in an optimal position that corresponds to a standing wave node for the 28.4 nm wavelength and standing wave anti-node for the 30.4 nm wavelength has been chosen. The multilayer structure is shown in Table 7, in Table 5 and in Fig. 8 the optimized multilayer performance is compared with the standard periodic multilayer.

3.4   Experimental results

In this section the experimental results are presented. Samples deposition has been performed at RXO with magnetron sputtering technique [10] and characterized by the RXO laser plasma facility [11] and at the ALS synchrotron.

In the first step the sample Mo/Si ML + Cr/Si CL (sample 1) showed in table 6 has been realized. Because of the noticeable mismatch among the experimental and the theoretical results both a single-layer Cr film (sample 2), and a Si/Cr (sample 3) periodic multilayer have been deposited and characterized. In fact the cause of mismatch noticed in the sample 1 has been attributed to an intermixing at the Si-Cr interfaces, and consequently to a Si and Cr systematic thickness errors. The Cr film thickness cames out within 2% of the target thickness and the Si/Cr multilayer was within 4% of the target but the XRR results indicated that the relative Si/Cr thickness ratio was a little off, suggesting that there is indeed some intermixing going on.

According to the information obtained by the characterization of the sample 2 and 3 another multilayer Mo/Si ML + Cr/Si CL (sample 4) has been deposited and characterized with the Si-Cr deposition rates corrected in order to compensate the intermixing. Unlike our expectations the multilayer reflectivity peak has been reduced. In order to understand the instability and the mismatch with respect to the theoretical predictions showed by the samples 1 and 4 some data fittings have been performed varying to various parameters trough IMD program [7]:

1) Si, Cr and Mo layer thicknesses (see Fig. 9 and 10)

2) interdiffusion at the interfaces.

From these simulations we have concluded that there is not a clear indication of what went wrong during deposition, but also that the structure proposed in the section case 3 has some intrinsic weakness. In some simulation cases the thickness errors are definitely exceedingly larger than the deposition uncertainty, however in others they are not so large.
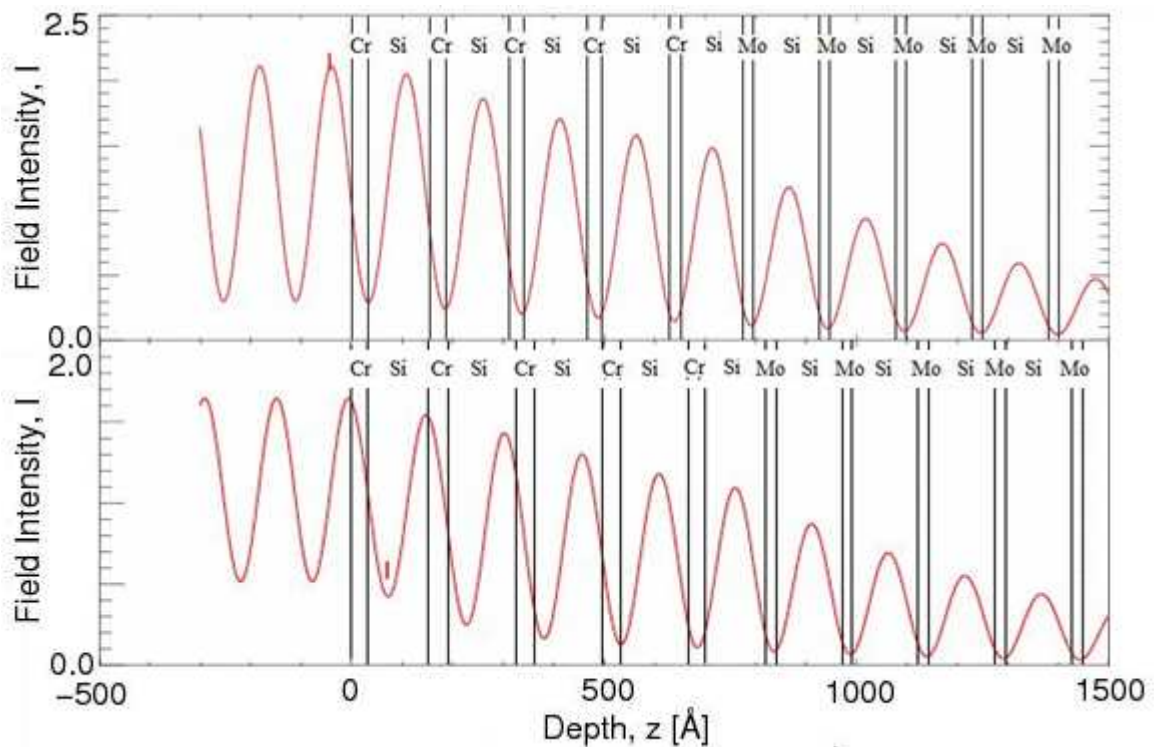
However, from the standing wave distribution it can be seen that the layers mainly affecting the performance of the coating coincide with an anti-node of the standing wave field (see Fig. 11). This condition can be due to both systematic and casual layers thickness errors that can result in a critical shift of some absorbing layers. In conclusion, it seems that this structure design is to critical and correspondingly has very stringent manufacturing requirements. The reason can be due to the various Cr absorbing layers, some of them being located in unstable positions not corresponding exactly to nodes of the standing wave.
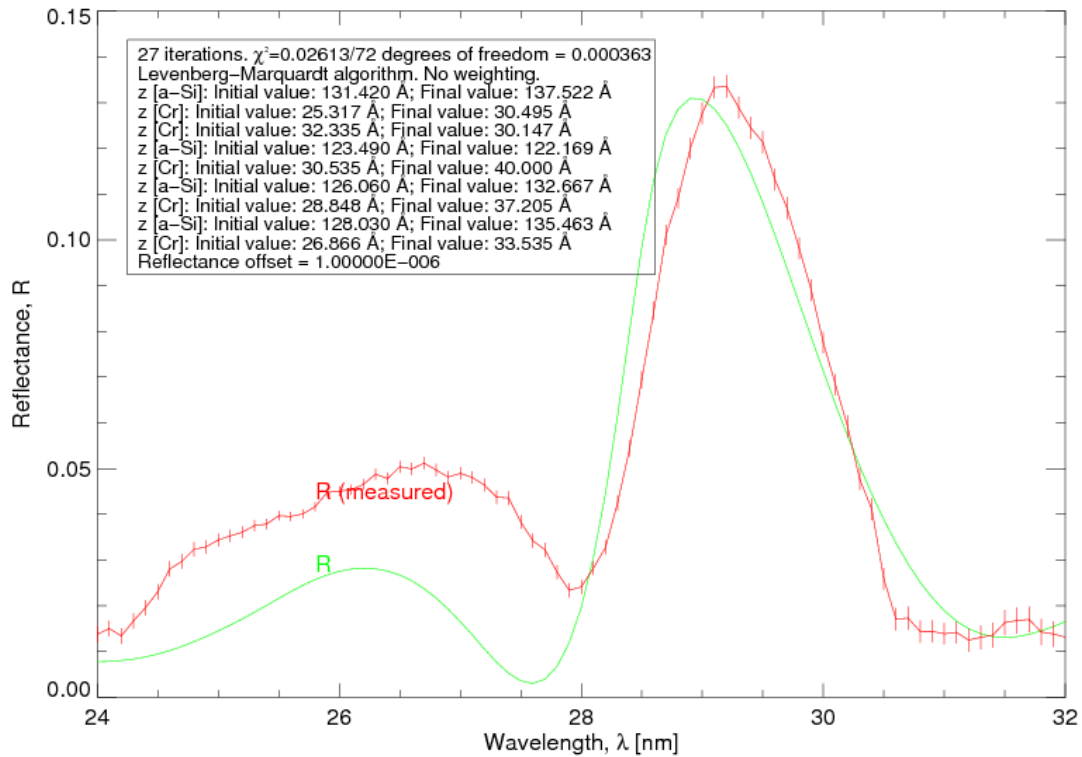
Fig. 9 Experimental results, including the error bar, for the structure sample 1, dotted curve, with the result of a fitting where the free parameters are the CL thickness layers.
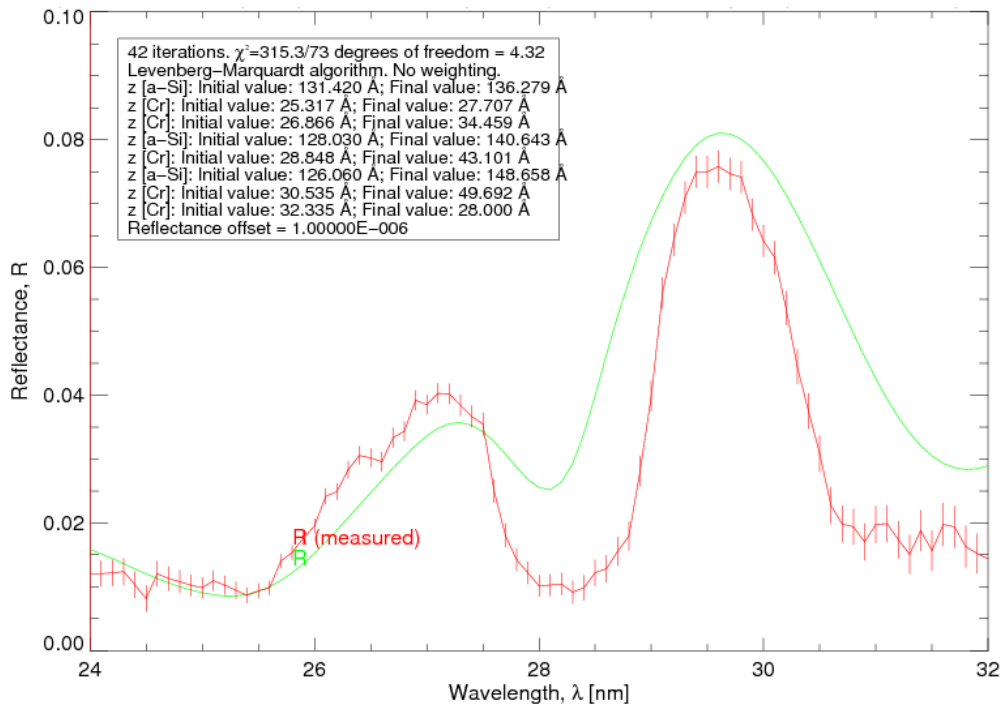
Fig. 10 Experimental results, including the error bar, for the structure sample 4, dotted curve, with the result of a fitting where the free parameters are the CL thickness layers.

Fig. 11 The standing wave distribution of the sample 1, case a) the simulation of the nominal structure (see table 6, and case b) of the nominal ML structure plus CL layers thickness obtained by the fitting showed in Fig. 11

| CL Structure	Value
a-Si	15.4 nm
Mo	3.55 nm
a-Si	41.2 nm
Mo	3.55 nm
ML structure	Value
Period (a-Si/Mo)	153 nm
Ratio	0.768
Period number	40

Table 8 *The structure of the re-designed multilayer using optical constants of Tarrio et al.[9], see text.*

In order to avoid the experimental difficulty of the Mo/Si ML + Cr/Si CL structures, a sample Mo/Si ML + Mo/Si CL has been deposited. In the first attempt (sample 5) the experimental result was different from the theoretical prediction. However using the optical constants experimentally measured and reported by Tarrio et al. [9], instead of the optical constant provided by IMD program, the theoretical simulation fit the experimental results in better way. Therefore, a new structure has been designed accordingly to the Tarrio's optical constants (see Table 8). A prototype of this sample has been deposited (RXO) and tested. The reflectivity has been measured with a laser plasma facility [11].

In Fig. 12 the experimental results for the a-periodic optimized structure, dotted curve, compared with the theoretical simulation. In Fig 13, instead, a comparison among the experimental results of both periodic and aperiodic structures.
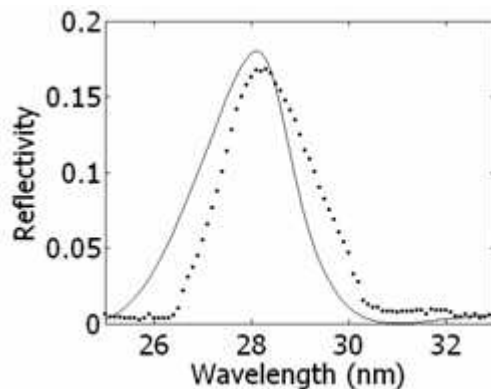
Fig. 12 *Experimental results (included the error bar) for the a-periodic optimized structure of table 8, dotted curve, compared with the theoretical simulation.*
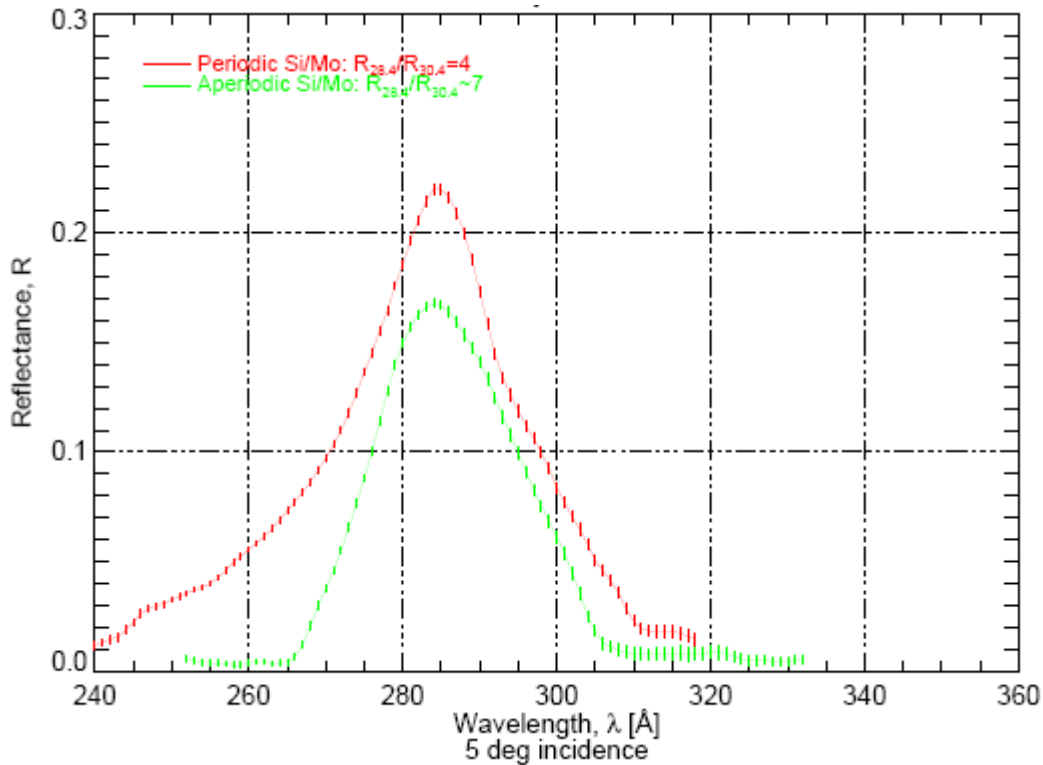
Fig. 13 *Experimental results (included the error bar) for the a-periodic optimized structure of table 8, green curve, compared with the periodic structure, red curve.*

The good agreement between theoretical and experimental results is noticeable. Simulations show that the critical parameter of this multilayer is the thickness of the second 41.2 nm thick Si layer (see table 8), a relative error of only a few percent can affect considerably the final performance, resulting in lower reflectivity peak and shifting of peak and rejected wavelengths. In order to accurately measure the rejection ratio at the 30.4 nm wavelength a measurements has been performed at ALS synchrotron. The measurements performed by laser plasma facility are, in fact, limited by the signal to noise ratio.

In Fig. 14 the result of the ALS measurements show a reflectivity peak of about 0.19 and a minimum reflectivity value of about 10^{-5} at 32.5 nm. However the experimental curve shows some important differences with respect to the computed one. The reflectivity peak is higher and slightly shifted of about 0.1 nm and the minimum of the R curve is at longer wavelengths, furthermore an additional minimum appears on the short wavelength side.

We have tried to approach the problem working on the critical thickness of the second 41.2 nm thick Si layer. The determination of the Si thickness error has been approached in two different way:

1) fitting of the experimental curve obtained by changing the thick of the critical Si layer in the capping structure

2) optimizing the phase of the ML structure inducing a standing wave shift into the CL

This shift has the effect of a stronger absorption at different wavelengths than expected and also to get a higher peak reflectivity at the working wavelength, therefore thank to this simulations we have estimated an error of about 2 nm the thickness of the second last Si layer.

In conclusion an innovative method for the design of multilayer structures with improved spectral filtering performance have been presented [12]. Structures with high rejection at the strong 30.4nm HeII line have been designed. Preliminary samples have been realized and tested, obtaining good agreement with simulations and demonstrating actual feasibility. Moreover a method for check and, eventually adjust, the thickness of the critical layer has been developed.
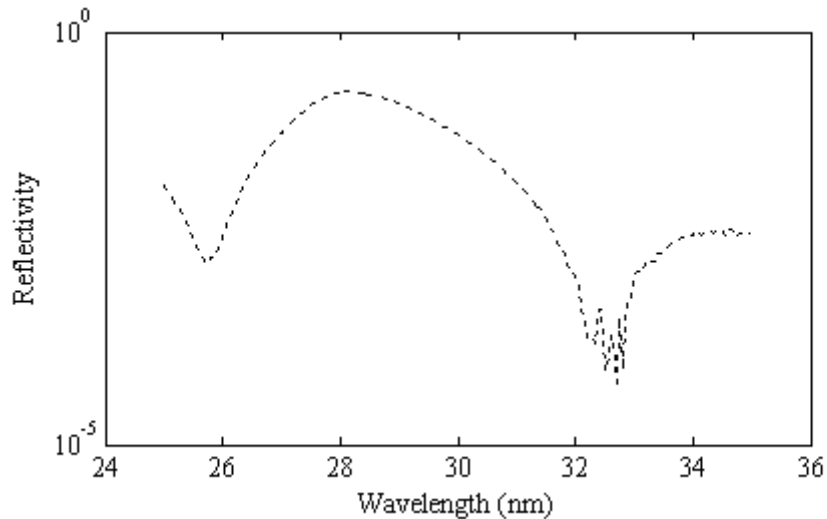

Fig. 14 Experimental results obtained by ALS measurements for the a-periodic optimized structure of table 8.

References

1   http://umbra.nascom.nasa.gov/eit/

2   http://trace.lmsal.com/

3   J. Zhu, Z. Wang, Z. Zhang, F. Wang, H. Wang, W. Wu, S. Zhang, D. Xu, L. Chen, H. Zhou, T. Huo, M. Cui and Y. Zhao, "*High reflectivity multilayer for He-II radiation at 30.4 nm*" Applied Optics Vol. 47, issue 13 , pp C310-314, 2008.

4   S. Zuccon, D. Garoli, M.G. Pelizzo, P. Nicolosi, S. Fineschi and D. Windt, "Multilayer coating for multiband spectral observations", in Proceedings of the International Conference on Space Optics (ICSO), ESA-SP (European Space Agency, 2006).

5   J. Gautier, F. Delmotte, M. Roulliay, F. Bridou, M.F. Ravet, and A. Jérome, "*Study of normal incidence of three-component multilayer mirrors in the range 20-40 nm*" Applied Optics Vol. 44, pp 384-390, 2005.

6   M. Suman, M.-G. Pelizzo, P. Nicolosi, and D. L. Windt**, "***Aperiodic multilayers with enhanced reflectivity for extreme ultraviolet lithography*", Applied Optics, Vol. 47, Issue 16, pp. 2906-2914.

7   D. L. Windt, Computers in Physics, 12, 360-370 (1998).

8   http://www.goes-r.gov/

9   C. Tarrio, R. N. Watts, T. B. Lucatorto, J. M. Slaughter, C. M. Falco, "*Optical constants of in situ-deposited films of important extreme-ultraviolet multilayer mirror materials*", Applied Optics, Vol. 37, pp.4100-4104 (1998).

10   www.rxollc.com/

11   D. L. Windt and W. K. Waskiewicz, "*Multilayer facilities for EUV lithography*", Journal of Vacuum Science Technology B 12, 3826-3832 (1994).

12   M. Suman, M. G. Pelizzo, D. L. Windt, G. Monaco, S. Zuccon, and P. Nicolosi; "*Innovative design of EUV multilayer reflective coating for improved spectral filtering in solar imagin**g***",   in Proceedings of the International Conference on Space Optics (ICSO), ESA-SP (European Space Agency, 2008).

Chapter 4: Multilayer coating for x ray astronomy applications

4.1   Introduction [1]

I have reported the main parts from [1].

The configurations adopted in X-ray telescopes are based on the Wolter I designs [2].

In the past mirrors have been coated by a single material layer exploiting the external reflection phenomena [3,4]. This approach can be very critical at energies above 10 keV, since external reflection appears at very low grazing incidence angle, and therefore very tight mechanical constraints in mirror alignment and on optical mounts are required. More recently the discovery and development of multilayer coatings have revolutionized the roadmap of the x-ray telescope's technology and the future missions like for example Simbol-X [5] and XEUS [6,7,8].
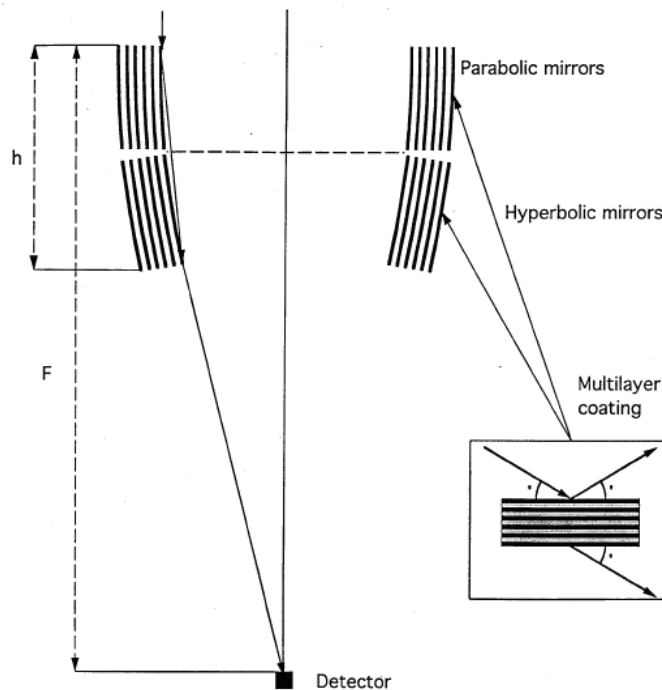
Fig. 1 *Section of a grazing incidence Wolter I optics, composed from many nested shells. The incidence angle is different for each shell. This design has been successfully employed for several soft X ray missions with monolayer mirror shells, but it can be used with multilayer coated shells to focus hard X rays.*

In the Wolter I configuration a single mirror is shaped following a double-profile (parabola-hyperbole) rotational symmetric surface. The grazing incidence double-reflection happens first on the parabolic surface, then on the hyperbolic one. The grazing incidence angle θ on a shell is given by the formula:

$$\theta = \frac{1}{4} \cdot \arctan g \left(\frac{D}{F} \right) \tag{4.1}$$

where D is the shell diameter and F is the focal length (see Fig. 1). In general, astronomical X-ray optics are formed by a number of nested confocal mirror shells in order to increase the collecting area of the system. According to equation (4.1), the incidence angle monotonically increases from the inner to the outer shells.

Since the maximum effective angle is inversely proportional to energy (this happens in both total and Bragg reflection configurations), harder X-rays are in general reflected by the innermost shells.

Since the reflectivity curve as a function of the photon energy of a given depth-graded multilayer mirror depends on the incidence angle a shell-by-shell global optimization [9] of the whole system would be highly desirable to get the best performances of the system.

The ideal behavior of an x-ray Wolter telescope is a relatively high and flat effective area. The effective area (A_{eff}) is:

$$A_{eff} = A_{projected} \cdot E^2 \cong 8 \cdot \pi \cdot F \cdot L \cdot R_\theta^2(E) \cdot \theta^2 \cdot E^2 \qquad (4.2)$$

where $A_{projected}$ is the geometric area projected by the shell, E is the energy, θ is the grazing incidence angle, F is the focal length, L is the length of the mirror and R is the reflectivity performances.

4.2   Broadband multilayer design [1]

I have reported the main parts from [1].

Different mathematical approaches have been used for finding the optimum solution in term of broadband reflectivity. Global optimization algorithms like genetic algorithm [10], simulated annealing [11] or iterated simplex [1] capable of searching the optimum structure inside a very wide domain of possible solutions have been developed. More recently, a further step has been represented by a math formalism able to provide chaotic layer distribution solutions which have gain of very flat reflectivity [12].

In this application field the study are in a preliminary phase, some W/B$_4$C [13] structures have been designed and the optimization algorithm used is the Genetic Algorithm provided with the mathematical tools [14] mentioned in the Chapter 2 (see section 2.5.3).

The strategy used is:

step 1)   optimization using the powerlaw [1,15] design constraint

step 2)   chaotic optimization starting from the optimal structure obtained in the precedent step (in this context the term chaotic is intended to mean that the values of the thicknesses can not be described by or do not follow any particular order or trend).

In the first step the bi-layer thickness variation has been designed following the powerlaw constraint [1,15]:

$$d_i = \frac{a}{(b+i)^c} \qquad (4.3)$$

with i bi-layer index from bottom to top and a, b, c parameters to be determined. Also the Γ ratio (between the thickness of the high density material and the total one) of each bi-layer is optimized with parameters according to a linear variation law:

$$\Gamma_i = m \cdot i + \Gamma_1, m = \frac{\Gamma_N - \Gamma_1}{N - 1} \tag{4.4}$$

where Γ_N, Γ_1 are respectively the Γ ratios of the first and last bilayers of the stack (in this way the total number of parameters to be optimized are five). Mathematical parameters limits are given by *a,c > 0, b < 1*, $\Gamma_N,\Gamma_1>0$. No other limits are imposed, letting parameters free to vary in the whole parameter space. For the evaluation of the multilayer reflectivity (which is the parameter determining the effective area of a given mirror shell) the classical recursive formalism by Parrat [16] has been used, with the reflectivity reductions due to the roughness computed by the Nevot-Croce approach [17].
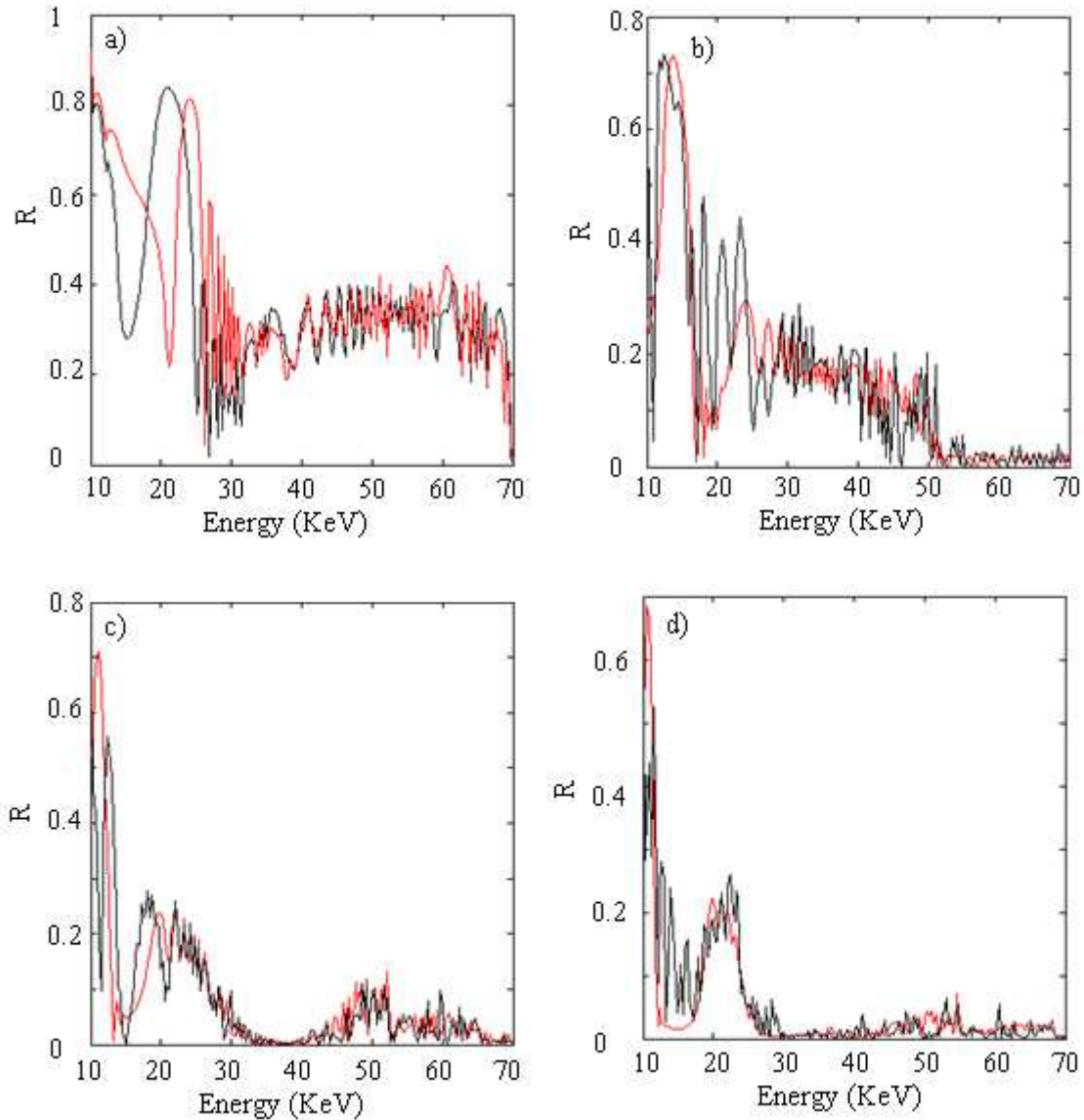
Fig. 2 *The reflectivity behaviours of the optimized multilayer; in black line the reflectivity behaviour of the structures designed with the powerlaw constraints and in red line the reflectivity behaviour of the structure designed into the step 2). In the cases a), b), c) and d) respectively the optimal results at the incidence angles 0.2°, 0.3°, 0.4° and 0.5°.*

A minimum possible d-spacing 20 Å has been fixed, while for all multilayers an interfacial microroughness of 3.0 Å was used. Both values seem to be realistic taking into account the current

technological achievements in the field of thin film deposition techniques under vacuum with super-polished substrates.

In the second step the thicknesses layer has been optimized into a range 20-d_{max} Å without any other constraints. The parameter d_{max} depends on the incidence angle and the energy range of the optimization run, the resultant structures are generally chaotic

4.3   Simulation of some results

In this section some results of the W/B$_4$C multilayer [13] optimization will be showed and discussed. In table 1 and 2 the input parameters used for the optimization of W/B$_4$C multilayers.

In the case reported in table 1 four multilayer structures have been designed at the incidence angles 0.2°, 0.3°, 0.4° and 0.5° in order to maximize the reflectivity area into the range 10-70 KeV, these parameters can be interesting for example for the XEUS mission [7]. In Fig. 2, a), b), c) and d) the reflectivity behaviors respectively at the incidence angles 0.2°, 0.3°, 0.4° and 0.5° have been reported. In any cases in red line the reflectivity of the multilayer designed with the powerlaw constraints and in black line the reflectivity of the chaotic optimized multilayer.
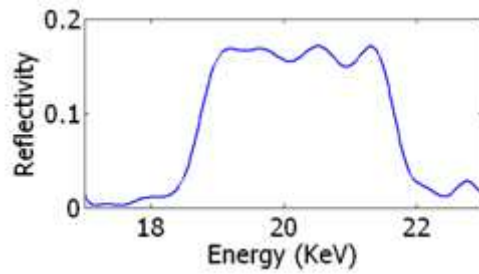
Fig. 3 The reflectivity behaviour of the multilayer optimized under the input parameters of the table 2.
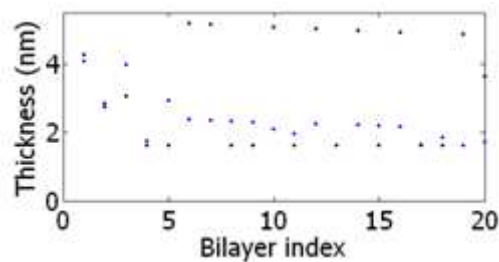
Fig. 4 The layers thickness of the optimized multilayer structure with the input parameters reported in table 2: in blue W, in black B$_4$C. The abscissa represents the increasing period number starting from the most external to the internal layer.

The chaotic design gives a noticeable improve to the reflectivity into the spectral region 15-20 KeV respect the powerlaw design, in the other spectral regions the behaviour is substantially similar. Further analysis will be applied with respect to the stability varying to the layers thickness in order to understand if

the chaotic structure, designed by the optimization algorithm developed in this PhD work, have an high efficiency and stable performances.

Incidence Angle	Optimization parameters
0.2°	Period number = 222 d_{max} = 220 Å Energy range = 10-70 KeV Roughness = 3 Å
0.3°	Period number = 235 d_{max} = 250 Å Energy range = 10-70 KeV Roughness = 3 Å
0.4°	Period number = 319 d_{max} = 275 Å Energy range = 10-70 KeV Roughness = 3 Å
0.5°	Period number = 333 d_{max} = 300 Å Energy range = 10-70 KeV Roughness = 3 Å

Table 1: *in the first column the incidence angle and in the second column the parameters used for the optimization.*

Incidence Angle	Optimization parameters
0.5°	Period number = 20 d_{max} = 50 Å Energy range = 19-21 KeV Roughness = 3 Å

Table 2: *in the first column the incidence angle and in the second column the parameters used for the optimization.*

In the case reported in table 2 the merit function is the maximum reflectivity area coupled with flat responses [12] in a predetermined spectral range into the 18-22 KeV energy range. In Fig. 3 the reflectivity behaviour of the optimized structure and in Fig. 4 its layer thicknesses are showed. The thicknesses trend is chaotic.

4.4   Conclusions

W/B4C multilayer structures have been designed in order to maximize the reflectivity area in a predetermined spectral region. The multilayer structures has been designed using an innovative optimization algorithm developed in this PhD work, the performances is comparable with the state of the art [1]. Now a method for test and compare the solution stability will be developed and performed in order to understand if the chaotic structures are more stable respect the thickness errors than the powerlaw structures.

References

1   V. Cotroneoand G. Pareschi; "*Global optimization of X-ray multilayer mirrors with iterated simplex method*"; Proc. SPIE **5536**, 49-60 (2004).

2   L. P.Van Speybroeck, R. C. Chase; *Appl. Opt.,* **12**, 24 (1972).

3   http://heasarc.gsfc.nasa.gov/docs/chandra/chandra.html

4   http://heasarc.gsfc.nasa.gov/docs/xmm/xmm.html

5   http://www.asdc.asi.it/simbol-x/

6   G. Pareschi, O. Citterio, M. Ghigo, F. Mazzoleni, and D. Spiga; "New X-ray Missions"; Memorie della Società Astronomica Italiana; supplementi vol. **3**, 323 (2003).

7   V. Cotroneoand G. Pareschi; "*Soft (0.1 – 10 keV) and hard (> 10 keV) X-ray multilayer mirrors for the XEUS astronomical mission*"; Proc. SPIE **5168**, (2003).

8   "*The XEUS Telescope*", ESA SP-**1253**, (2001)

9   T. Okajima, et al., "*Supermirror Design for the XEUS X-ray Telescope*", ASP Conference Proceedings Vol. **251**, p.582 (2001).

10   P. Charbonneau; "*An introdution to Genetic Algorithms for numerical optimization*", *NCAR Technical Note 450+IA* – online at: http://www.hao.ucar.edu/public/research/si/pikaia/tutorial.html

11   X. Cheng, Z. Wangì, Z. Zhang, F. Wang, L. Chen; "*Design of X-ray super-mirrors using simulated annealing algorithm*"; Optics Communications **265** 197–206 (2006).

12   C. Morawe, E. Ziegler, J.-C. Peffen, I. V. Kozhevnikov; "*Design and fabrication of   depth-graded X-ray multilayer*"; Nuclear Instruments and Methods in Physics Research A 493 189–198 (2002).

13   D. L. Windt, E. M. Gullikson and C. C. Walton; "*Normal-incidence reflectance of optimized W_B4C x-ray multilayers in the range 1.4 nm < λ< 2.4 nm*"; Optics Letters **27**(24) (2002).

14   M. Suman, M.-G. Pelizzo, P. Nicolosi, and D. L. Windt; PCT/EP2007/060477.

15   K. Joensen, et al.; "*Design of grazing-incidence multilayer supermirrors for hard-x-ray reflectors*", Appl. Opt., **34**, 7935 (1995).

16   L.G. Parrat, Phys. Rev., **45**, 359 (1954)

17   L.G. Nevot and P. Croce, Phys. Appl., **15**, 761 (1980)

Chapter 5: Design of aperiodic multilayer structures for attosecond pulses in the extreme ultraviolet spectral region

5.1   Introduction

Multilayer coatings are the only way to have high efficiency EUV optics working in normal incidence configuration. Typical periodic structures are characterized by energy band coverage usually restricted to few percent of the peak energy i.e., for example, a few eV at about 100 eV. This means that in the case of ultra–short radiation pulses ($<$ fs) the corresponding "wide" spectral features cannot be preserved.

The design of aperiodic reflecting multilayer structures for attosecond physics in the extreme ultraviolet spectral region is studied in this chapter. The multilayers are designed for different spectral XUV range and with different reflectance and phase design goals like high total spectral reflectivity coupled with very wide bandwidth, spectral phase compensation, and amplitude reshaping. Furthermore, to take into account manufacturing tolerances, solutions stable with respect to random layer thickness variations or materials interdiffusion [1], are selected thank to the use of the algorithm developed in this PhD work and described into the chapter 2 (see section 2.5.3).

Recently, Morlens *et al.* [2] have studied the second order constant chirping of the plateau harmonics phase in the case in which only the short electron quantum trajectories contribution is considered.

This work demonstrates the possibility of compensating this chirping using an opportune broadband aperiodic multilayer in the 70–100 eV energy range. In a different work, Morlens *et al.* [3] have measured a three elements broadband multilayer in the 35–50 eV range. Differently, Wonisch *et al.* [4] have designed and analyzed a broadband aperiodic multilayer characterized by a substantially linear phase. This work is particularly interesting for isolating attosecond pulse, for example, in pump–probe experiments. In the cited papers aperiodic structures are designed by applying optimization procedures. An important limitation is generally due to the very low efficiency of the reflecting structures, affecting the experiment throughput and consequently the signal to noise ratio of the acquired data. Moreover, an experimental characterization of multilayers with chirped phase has been performed by Aquila et al [5].

In this chapter will be discussed the design results obtained by the optimization of multilayer structures for attosecond pulses and the innovative experimental characterization, developed in this PhD work, in order to extrapolate the phase behavior by the electrons photoemission signals.

5.2   Broadband multilayer design

Depending on the dualism between the time and frequency domains a generic merit function has been defined through the sum of single merit functions defined, respectively, in each domain. Furthermore the merit functions in the time and in the frequency domain have been selected, respectively, in order to optimize the duration and the intensity of the reflected wave. The intensity of the reflected wave in the time domain, $I(t)$, is calculated from the incident electromagnetic field $E_i(t)$, according to the following equations:

$$I_i(f) = E_i(f) \cdot E_i(f)^*$$
$$E_i(f) = FT\left(E_i(t)\right)$$
$$E_r(f) = E_i(f) \cdot r_{ML}(f) \tag{5.1}$$
$$E_r(t) = IFT\left(E_r(f)\right)$$
$$I_r(t) = E_r(t) \cdot E_r(t)^*$$

where $E_i(f)$ is the incident pulse electromagnetic field in the frequency domain, $I_i(f)$ is the correspondent incident intensity. $E_i(t)$ is related to $E_i(f)$ through Fourier transform functional, $r_{ML}(f)$ is the multilayer amplitude reflectivity, and correspondingly $E_r(f)$ is the electromagnetic reflected amplitude in the frequency domain. The applied procedure evaluates the multilayer reflectivity by applying a recursive reflectance model approximation for taking into account multiple reflections at the interfaces [6,7].

To simulate actual structures a 1 nm thick cap layer of SiO_2 and a roughness value at interfaces of 0.5 nm have been assumed. The former has been considered to simulate the deposition of a last additional Si layer that oxidizing acts as a protective cap layer, while the roughness value is meant to take into account both roughness and interdiffusion and silicide composite formation at Mo–Si interfaces.

5.3 Design for EUV spectral range

Experiments in the ultrashort time regime can generate or deal with radiation pulses with very different characteristics, non uniform spectral components distribution, and phase frequency chirping. In the following some typical cases representative of a wide range of experimental conditions are considered. They are listed in Table 1; essentially, Gaussian and rectangular intensity spectral distributions coupled with linear or chirped phase behavior have been considered.

Cases	Input (Frequency Domain)		Output Requirements
	Intensity	Phase	
a)	Gaussian	Linear	Highest efficiency/limited time broadening ($\leq$155 as)
b)	Gaussian	Chirped	Highest efficiency/shortest duration
c)	Rectangular	Linear	Highest efficiency/limited time broadening ($\leq$155 as)
d)	Rectangular	Chirped	Highest efficiency/shortest duration
e)	Rectangular comb	Chirped	Highest efficiency/shortest duration

Table 1 Test Cases Description: Input Refers to the Characteristics of the Incident Radiation in Terms of Intensity and Phase Behavior; the Output Requirements Are Those Optimized in the S_W Evaluation Process

The optimized multilayer response is designed according to suitable and different requirements in the various cases. For a Gaussian attosecond input pulse with linear phase trend, case a), representative of an ideal attosecond pulse, reflection has to be accomplished without deformation.

Instead a pulse with chirped phase, case b), has been considered as representative of an ideal case useful to study the pulse compression through phase compensation. Cases c) and d) have the same, linear and chirped, respectively, phase behavior, but rectangular spectral amplitude as a general approximation of a HOH spectrum. The pulse is reflected without any time broadening, case c), or is compressed, in case d). Finally, case e) corresponds to the spectrum of case d) multiplied by a HOH comb and spectrum filtered by 150 nm thick Zr mm.

The Gaussian intensity is described according to:

$$E_i(f) = e^{-2 \cdot \sigma^2 \cdot \pi^2 \cdot (f-f_0)^2} \cdot e^{i \cdot l \cdot (f-f_0)^2} \qquad (5.2)$$

where σ=55 as. The last complex exponential term represents the chirp contribution, with the parameter l set zero in the case of linear phase trend or 0.3 fs^2 for chirped pulses. Both Gaussian and rectangular intensity time distributions correspond to the envelope of 90 eV carrier frequency pulses.

The coating reflectivity is computed assuming an angle of incidence of 20°, and S polarized waves and 0.5 nm rms roughness value at interfaces. The main parameters characterizing the performances of the designed coating structures, which have been evaluated for the various cases, are the time duration of the pulses and the compression ratio corresponding to the ratio between the duration T_{refl} of the reflected pulse and T_{inc} of the incident pulse, and the throughput P corresponding to the ratio between the intensity of the reflected and incident pulses.


5.3.1   Case a)

Single ideal attosecond pulses are very interesting for pump–probe experiments. In this example a Gaussian intensity pulse with linear phase behavior is considered. The merit function has been defined in order to realize a coating structure with the highest reflectivity and maximum allowed time broadening value of ($\leq$155 as), the first for optimizing the system throughput, the second for having a limited additional time broadening of the reflected pulse. Furthermore the procedure, as already explained, has been designed in order to search for a relatively stable solution, i.e., not critically affected by layer thickness variations. This has been conceived in order to take into account manufacturing tolerances that can affect the thickness of the layers and so the practical feasibility of the coating. This latter constraint has been applied to all structures considered in the following cases. The multilayer structure consists of only 12 layers; this low number is due to the achievement of linear phase constraint on a suitably large spectral range and consequently causes a relatively low peak reflectivity. In Fig. 1 the reflectivity curve (continuous curve) and the spectral phase of the designed structure (dashed–dotted curve) are shown. The reflectance does not reach such high values characteristic of a periodic structure but it shows a relatively wide bandwidth.

Its not uniform waving shape does not affect significantly the reflected temporal pulse shape. This behavior is due to the absence of constraints for the merit function, which was defined simply in order to get the highest reflectivity independently on the spectral shape, and allowing for some limited time broadening. In Figs. 2(a) and 2(b), respectively, the time shape of the incident and reflected pulses is reported, showing

that the reflected pulse essentially complies with time broadening requirements. This result is due to the large bandwidth of the reflectivity curve, spanning between 75 and 105 eV with a mean value of 0.066. Comparison with results obtained by Wonish *et al.* [4] with a different optimization method shows a significant throughput improvement (more than a factor of 2) although coupled with a slightly higher time broadening. However, it has to be noted that our simulations take into account 0.5 nm roughness, contrary to the calculations reported in the cited reference, where the effect of roughness at various layer interfaces has not been taken into account.
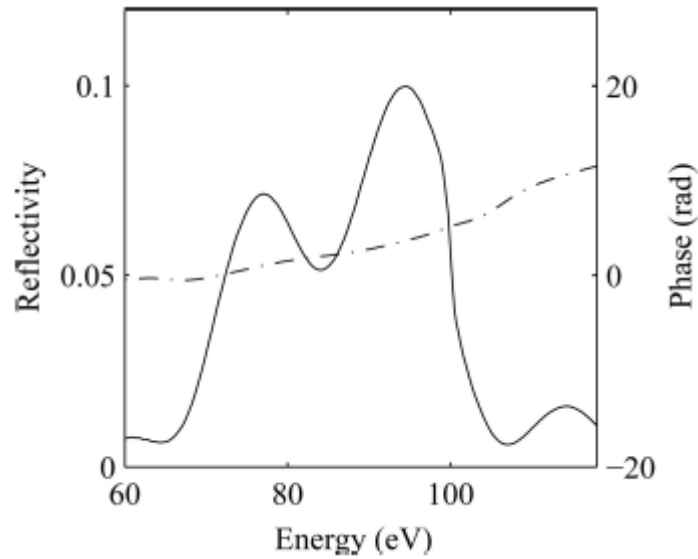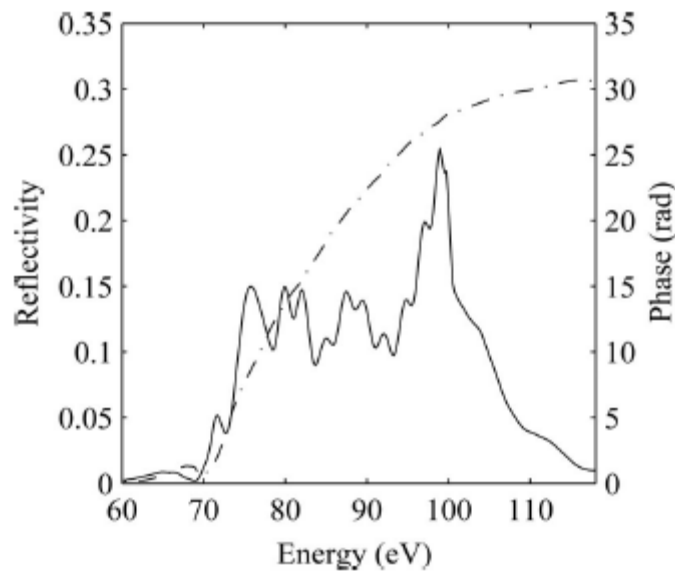

Fig. 1 *Case (a): characteristics of an optimized multilayer used to reflect, minimizing deformation, an ideal Gaussian pulse with linear phase. Continuous curve, spectral reflectivity curve; Dashed–dotted curve, phase behavior.*
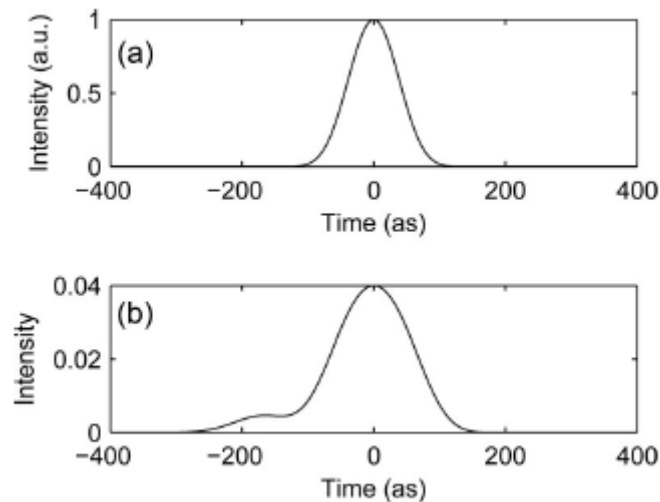
Fig. 2 *Case (a): (a) incident pulse, (b) reflected pulse.*

5.3.2   Case b)

The incident pulse is assumed Gaussian with positive second order phase chirp. It has been considered in order to study the mechanism of time compression by reflection through phase compensation. Pulses characterized by marked second order constant phase chirp can be generated by filtering the HOH plateau spectral region. In fact, by spatial filtering with an iris diaphragm the HOH spectrum, it is possible to select those harmonics due to short electron quantum trajectories contributions. Morlens *et al.* have considered this case in designing a structure for the 60–90 eV spectral range [4]. They report a reflectivity value of ~0.1 with a further estimated 20% reduction due to interface layer roughness. The merit function has been selected in order to get the highest reflectivity and reduced pulse time duration. The results reveal the possibility of obtaining pulse compression without relevant attenuation. It is worth noting, that similar phase compensation can be obtained filtering the harmonic spectrum with a Zr filter but with the drawback of only $0.6 \cdot 10^{-5}$ transmission due to the needed large film thickness. The designed multilayer structure consists of 70 layers, their thickness always larger than approximately 2 nm, demonstrating the technical feasibility of this coating.


Fig. 3 *Case (b): characteristics of an optimized ML designed to compress an ideal Gaussian pulse, with constant second-order positive GDD. Continuous curve, spectral reflectivity curve; dashed–dotted curve, phase behavior.*

In Fig. 3 continuous and dashed–dotted curves correspond, respectively, to the spectral reflectivity and the phase. The reflectivity mean value is ~0.15 and the bandwidth extends from 75 to 105 eV. The reflectivity amplitude remains relatively high in the whole spectral bandwidth; consequently, the resulting efficiency does not depend critically on the spike structure of the spectrum corresponding to the harmonic odd order from 49 to 67. Furthermore, phase compensation can synchronize the spectrum up to the 73rd harmonic. The phase presents a marked second order chirp. The effect on the reflected pulse is evident in Fig. 4, where the chirp of the incident pulse and of the reflected one are reported. The latter is almost linear in the whole bandwidth between 75 and 115 eV. In the figure the phase of the coating is reported, too, to

clarify its effect. The incident and reflected pulses are reported in Fig. 5, the energy is reflected with high efficiency, ~13%, and the FWHM is reduced from 458 to 129 as. The energy and the time compression of reflected pulse result higher and shorter, respectively, than those reported by other authors [2].
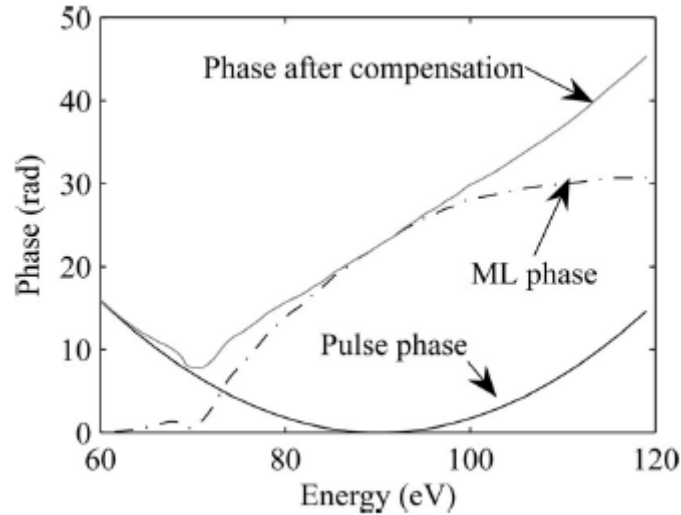

Fig. 4 Phase compensation referred to in case (b): continuous dark curve; pulse phase; dashed–dotted curve; ML phase; continuous gray curve, phase of the reflected pulse.
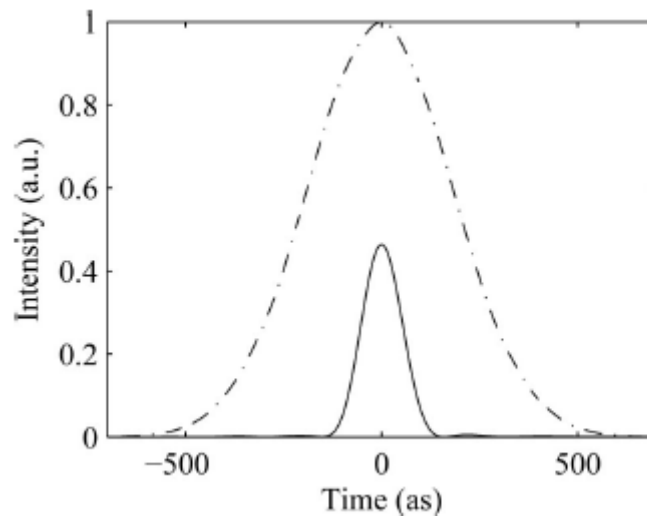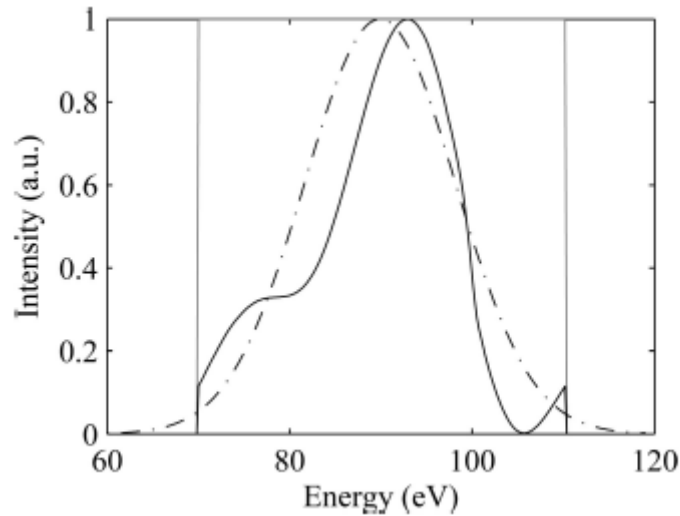

Fig. 5 Case (b): dashed–dotted curve, incident pulse; continuous curve, reflected pulse.

5.3.3   Case c)

In this case the incident pulse has intensity distribution with rectangular shape and linear phase trend. It is conceived as correspondent to an attosecond pulse, like one that can be obtained by filtering the proper HOH spectrum cutoff region, where the harmonics are phase locked [8]. In particular when a few femtoseconds driving laser pulse is used for harmonics generation, the cutoff presents mainly continuous spectral distribution correspondent to a single attosecond pulse. Since the harmonics are emitted in a time correspondent to a fraction of the driving laser pulse, they can be used for pump and probe experiments in the attosecond regime.
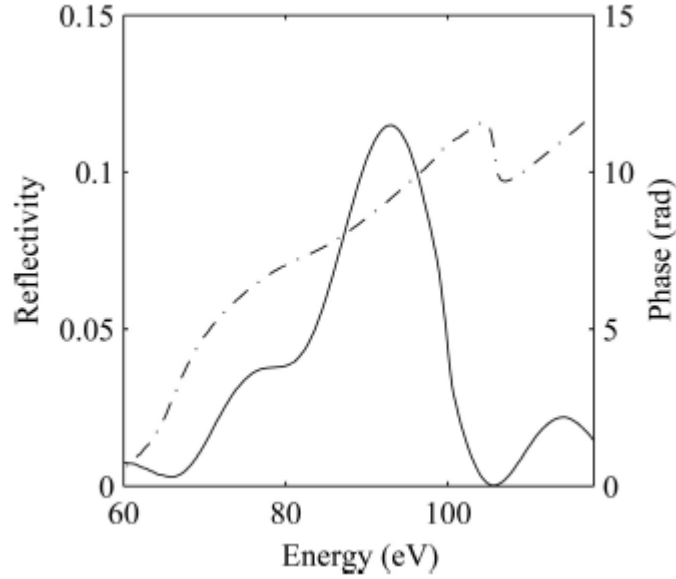
Fig. 6 *Case (c): characteristics of an optimizedMLused to reflect, minimizing deformation, an ideal pulse with rectangular spectrum and linear phase. Continuous curve, spectral reflectivity curve; dashed–dotted curve, phase behavior.*


Fig. 7 *Case (c): continuous gray curve, incident pulse; continuous dark curve, normalized reflected pulse; dashed–dotted curve, Gaussian spectrum (for comparison, see text).*

The requirements of high time resolution, i.e., single pulse with very short duration, and high signal to noise ratio, force the design of the optical system, in this case the reflective coating. Accordingly, it has to satisfy high throughput requirements coupled with limited time broadening (≤155 as), since the intensity of the HOHs is orders of magnitude weaker than the fundamental one. This is accomplished by operating amplitude reshaping of the intensity of the harmonics spectral features in order to produce strong single attosecond pulses. The reflectivity and phase behavior, respectively, of the optimized coating multilayer structure are reported in Fig. 6. The resulting normalized spectrum is reported in Fig. 7; there the spectral distribution of incident pulse and of an ideal Gaussian one are reported as well. Indeed, the resulting

55

structure of the multilayer coating is designed in order to generate, by reshaping the incident amplitude through reflection, as nearly as possible a Gaussian spectral distribution, in agreement with transformation rules (Gaussian curve is the function that exhibits the best relationship between spectral width and time duration, i.e., $\sigma_{time} \cdot \sigma_{freqeuncy}$) in Fig. 8 the incident and reflected pulses are reported versus time. The reflected pulse results slightly stretched from 102 to 143 as, while the 5% throughput is due to the low number of layers.

Results, obtained with different techniques, are presented by Wonisch *et al.* [4]. In this paper a shorter time duration of the reflected pulse (97 as) is reported. Nevertheless, in our solution we have looked for short time duration coupled with high reflectivity and accordingly a higher throughput level (5% versus 3%) has been obtained. Furthermore this result has been achieved taking into account 0.5 nm roughness at layer interfaces in the multilayer structure.
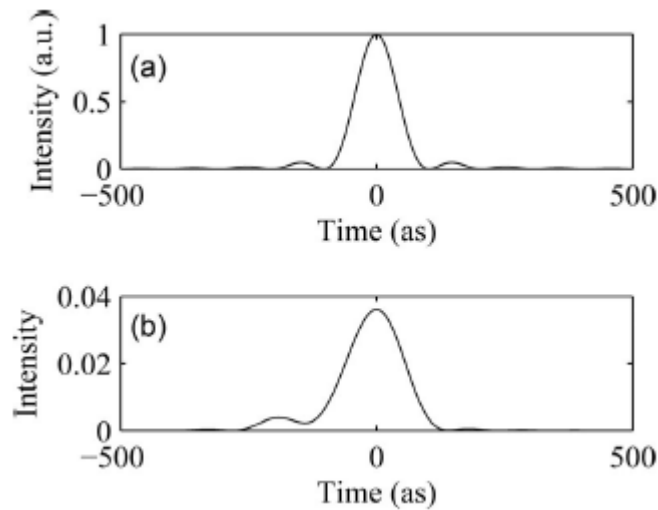

***Fig. 8*** *Case (c): (a) incident pulse, (b) reflected pulse.*

5.3.4   Case d)

The example illustrates the achievement of compression by reflection through both phase compensation and spectrum reshaping. In this case the spectral amplitude distribution is continuous differently from the next (e) case where a more realistic train of attosecond pulses is simulated with an ideal HOH spectrum. In Fig. 9 with continuous and dashed–dotted curves, the spectral reflectivity and the phase curves, respectively, are reported. The phase presents marked second order chirp and the reflectivity envelope a Gaussian trend. The effect of the two compression mechanisms, spectral reshaping and phase compensation, are illustrated in Fig. 10, where the normalized reflected pulse shows a marked spectral reshaping with the Gaussian spectral envelope, and in Fig. 11, where the phases of incident and reflected pulse are compared with that of the multilayer structure. The result shows that photons are reflected with high efficiency, ~15%. The incident and reflected pulses versus time are reported in Fig. 12. The first one manifests an exotic double peak although the inverse Fourier transform of a rectangular spectrum is a "sinc" function, and the presence

of a marked second order chirp produces a bimodal pulse shape. From Fig. 12 the pulse time duration shortening from 602 as to 140 as can be derived.
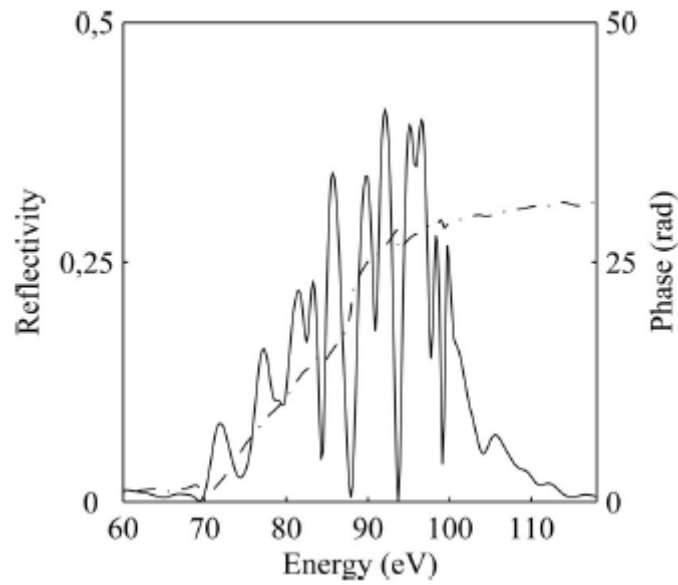
*Fig. 9* *Case (d): characteristics of an optimized ML used to compress an ideal pulse presenting rectangular spectral feature and second order chirping. Continuous curve, spectral reflectivity curve; dashed–dotted curve, phase behavior.*
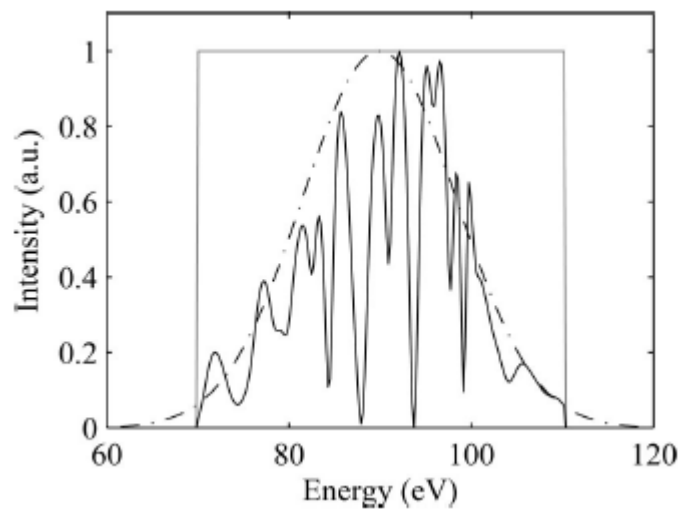
Fig. 10 *Case (d): continuous gray curve, incident pulse spectrum and continuous dark curve, normalized reflected one, are compared to a dashed–dotted curve, Gaussian spectrum.*
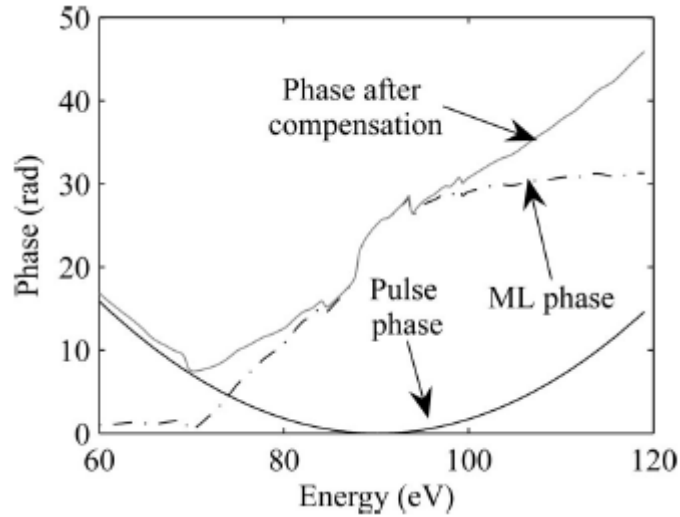
Fig. 11 *Case (d): continuous dark curve; pulse phase; dashed–dotted curve, ML phase correction; continuous gray curve, phase of the reflected pulse.*
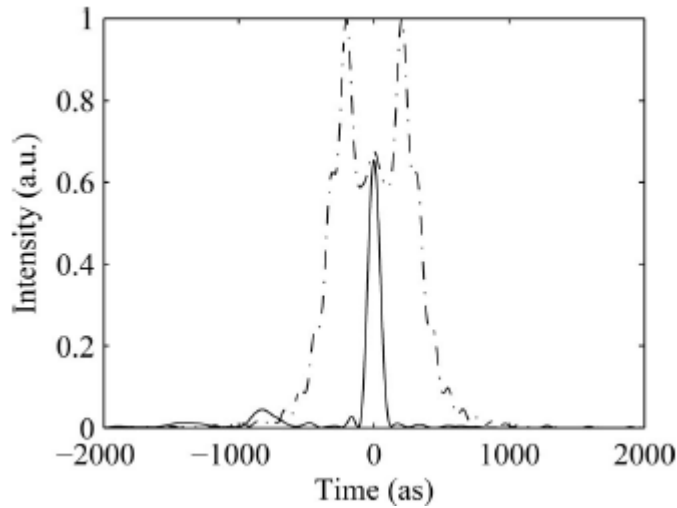

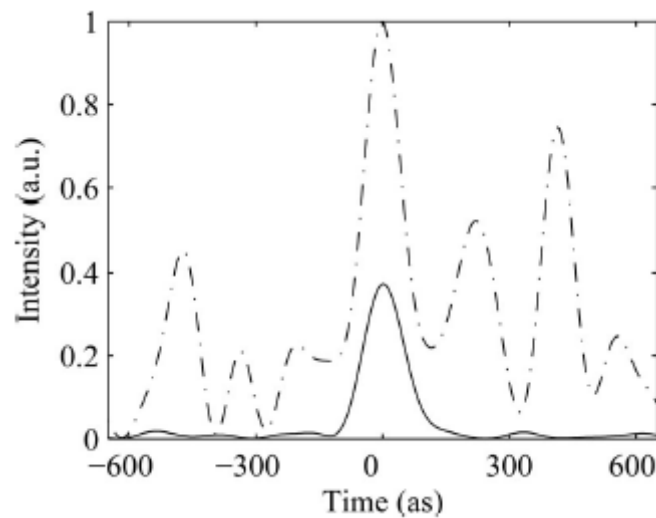**Fig. 12** *Case (d): (dashed–dotted curve) incident and (continuous curve) reflected pulses in time domain.*

5.3.5   Case e)

This last case presents the optimization process involving a comb spectrum representative of an ideal HOH spectrum. In Fig. 13(a) the spectrum of harmonics with the phase behavior showing a positive second order chirp is reported. The spectrum is filtered by a 150 nm Zr film chosen to suppress the strong contribution of fundamental and low order harmonics. The considered phase chirping can be explained as for case (b), for example, by selecting the harmonics emission due to short electron quantum trajectories with relatively narrow aperture. The merit function requirements have been set in order to get the highest efficiency with the shortest time duration pulse. The group delay dispersion introduced by the Zr filter has been taken into account in the coating structure optimization process. In Fig. 13(a) the resulting multilayer spectral reflectivity and phase behavior are reported as well. The former follows the harmonics structure; however, it performs amplitude reshaping of the harmonics spectral components in order to comply with merit function constraints. The resulting integrated spectral efficiency is quite high, reaching ~14%. In Fig.

13(b), the reflected harmonics spectrum and resulting phase are reported. It is evident the phase linearization performed by multilayer. In Fig. 14 the incident and reflected pulse train are reported versus time. It is noticeable the achieved time compression, from ~375 as, up to 143 as for each pulse.
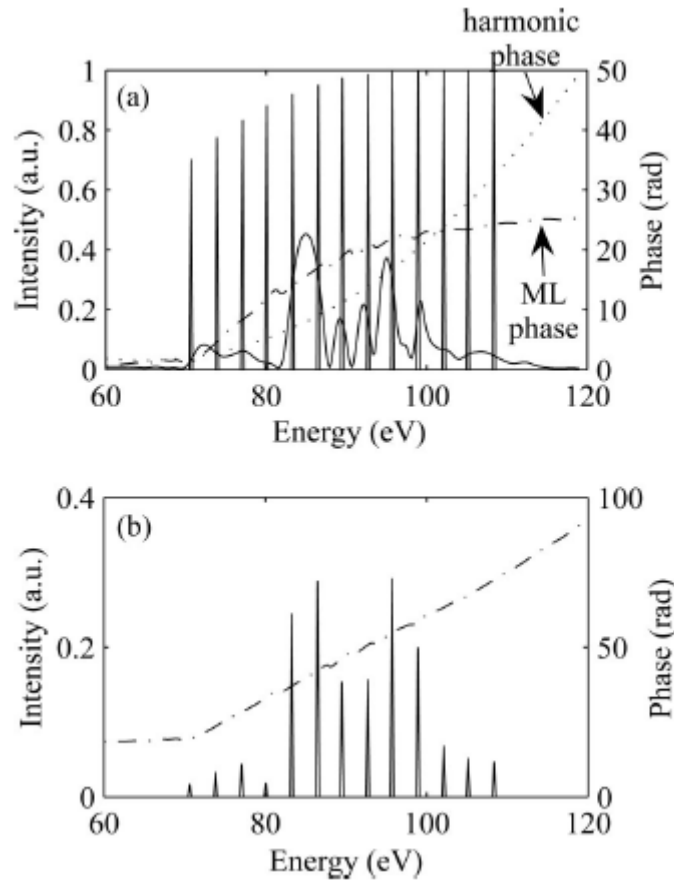
Fig. 13 *Fig. 14. Case (e): (a) continuous curves, incident spectrum and ML reflectivity; dotted curve, phase behavior of incident spectrum; and dashed–dotted curve, ML phase. (b) Continuous curve, spectrum; and dashed–dotted curve, phase of the reflected pulse.*

Fig. 14 *Case (e): (dashed–dotted curve) incident and (continuous curve) reflected pulse in time domain.*
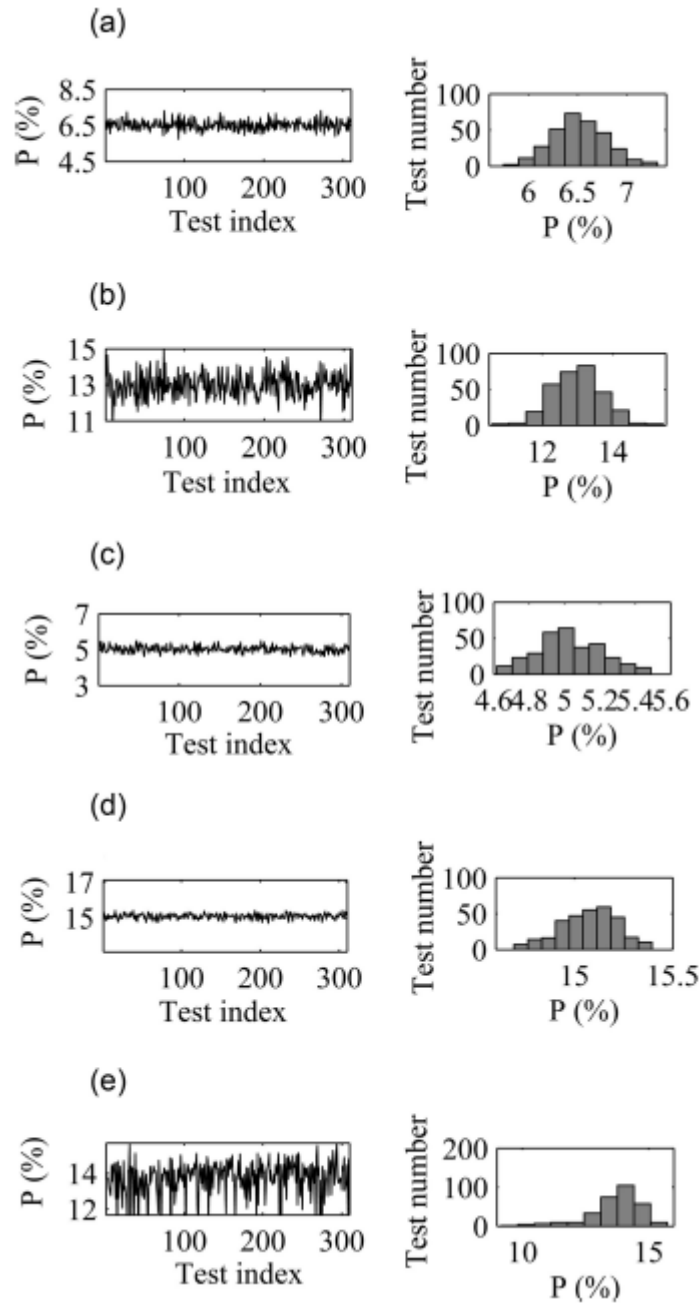
Fig. 15 *Cases (a)–(e) stability analysis. The plots in the left column report the P values corresponding to different perturbed versions of the nominal structures. The right column shows the same results with histogram plots. Each row refers to one of the five considered cases.*

5.3.6   Multilayer Design Stability Test

As already noted, the searching procedure, implemented through the algorithm with evolutive strategy, is designed to look for stable multilayer structures, i.e., not critically dependent on layers thickness deposition errors. In Figs. 15 and 16 the values of the throughput (*P*) and the time duration (*T*) parameters obtained by randomly varying (in the range ±2 Å) the layers thickness of the nominal structures presented in Section 3

60

are reported. The throughput, *P*, is defined as the reflected photon percentage, while the time duration, *T*, is defined according to the following standard formula,
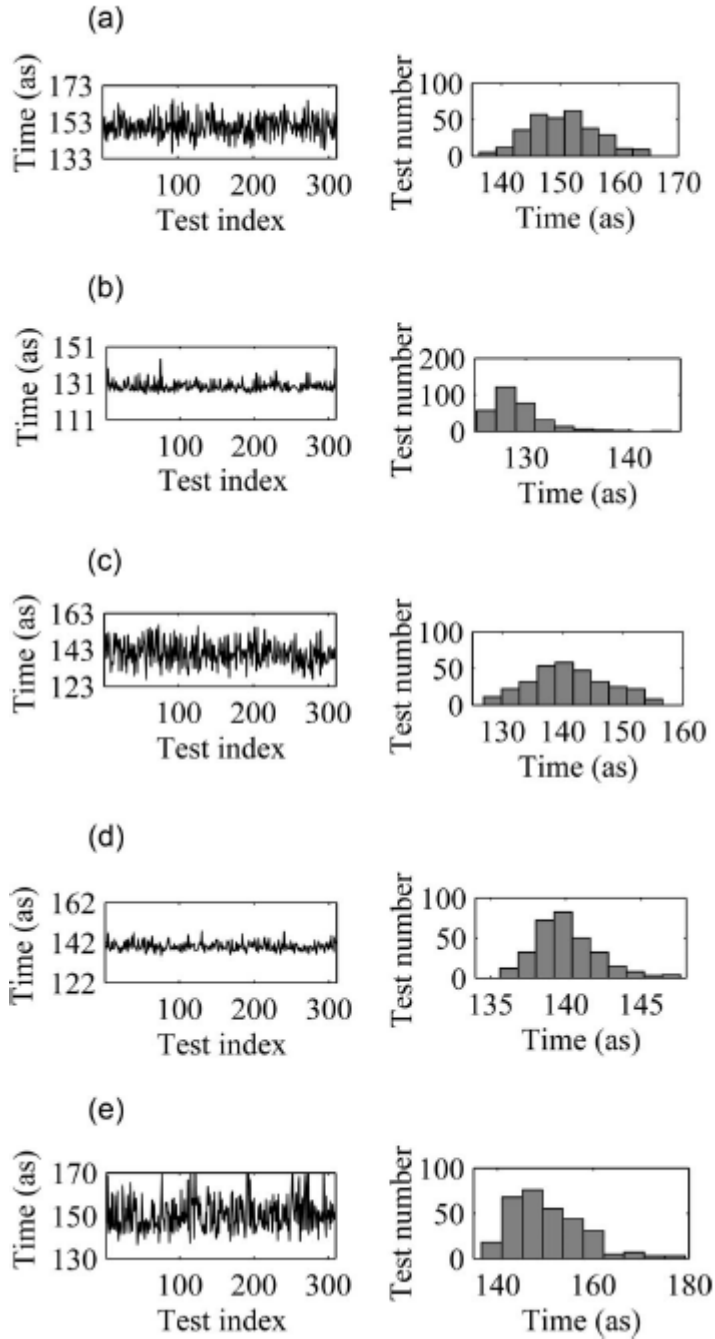
$$T = \frac{\int I(t)dt}{\max[I(t)]}.$$

(5.3)

Fig. 16 *Cases (a)–(e) stability analysis. The plots in the left column report the T values corresponding to different perturbed versions of the nominal structures. The right column shows the same results with histogram plots. Each row refers to one of the five considered cases.*

Case a)   Case b)   Case c)   Case d)   Case e)

		Performances				
	T	94	458	102	602	375
	Increments of reflectivity	152	129	143	140	143
	Reflectivity area (%)	52	103	46	132	116
	P (%)	6.55	13.00	5.00	15.2	14.3
	R Range (eV)	75-105	75-105	70-110	70-110	70-110
	Mean	0.07	0.13	0.05	0.15	0.12
	Layers ratio	0.167	0.73	0.167	1.00	0.73
		Stability				
T	χ_{norm}^2	0.78	4.93	0.9	2.18	5.4
	σ	5.8	2.6	6.6	2.1	7.6
	T	152.7	131	143	142	150.4
P	χ_{norm}^2	0.12	0.23	0.96	1.00	8.3
	σ	0.27	0.7	0.18	0.14	1.04
	P	6.5	13.0	5.0	15.1	13.7

Table 2 *Test Cases Description: Input Refers to the Characteristics of the Incident Radiation in Terms of Intensity and Phase Behavior; the Output Requirements Are Those Optimized in the S_W Evaluation Process*

The number of considered test samples is 310. In Figs. 15 and 16 on the left side the P and T values, respectively, are reported, the abscissa indicating the test index. The correspondent confidence interval at one standard deviation σ is reported in Table 2, where the results of the simulations are summarized and will be discussed in the next section. In Fig. 15, left side, the full ordinate range scale has been set 4% of the average P value, while in Fig. 16, left side, it has been set 40 as. In the two figures on the right side the same information is presented with histogram plots. Figure 16 shows that the (c) and (d) cases, correspondent to rectangular spectral shape, result the most stable in terms of efficiency. Instead in Fig. 16 it is interesting to note that cases (b) and (d), where the main goal is time compression by phase compensation, result more stable than the other ones. A "chi square" test has been performed to verify how much the statistical distribution of the test samples approximates a normal distribution. This value is reported in Table 2. From the χ^2 value and the noticeable asymmetry of the histograms one can conclude that the (c) and (d) cases (see Fig. 15) are the most stable in terms of efficiency. The χ^2 values relative to Fig. 15 are quite near a normal distribution for all cases; however, the efficiency of structures designed for pulses with rectangular spectral shape results obviously more stable. The efficiency stability result is noteworthy for case (e) where the reflectivity curve shape is tailored on a highly discontinuous spectral distribution. In Fig. 16 and χ^2 values

reported in Table 2 one can observe that the (b) and (d) cases represent a stable and relatively high maximum for the time response of the multilayer structure. Since any random change in the multilayer structure is associated to an increment of the pulse duration we can deduce that solutions for these cases can be considered very close to real maxima. Differently, the (a) and (c) cases have been obtained as local maxima of the complex merit function, that is, they could even not correspond to local maxima for the merit function factor defined on the time domain.

5.3.7 Results Summary

In Fig. 18 the designed multilayer structures are reported. Table 2 summarizes the previously described results. In the first section the calculated performances are reported; T is the time duration, already defined, for the incident and reflected pulses. The reflectivity area ("Refl. Area") represents the ratio between integrated reflectivity of the optimized structure and that one of a constant 48 period multilayer optimized for reflection at the central energy (90 eV). It is noteworthy that the efficiency for cases (b), (d), and (e) is equal to or higher than a standard optimized periodic multilayer; P is the efficiency parameter of the multilayer, already defined, and reported in Fig. 15 for stability evaluation. For the reflectivity parameter R, the bandwidth range and the mean value are reported. The percentage of reflected photons is definitely high for all structures, reaching 15% for case (d) in agreement with the wide bandwidth and average R value. The "layers ratio" represents the ratio between the number of layers of the computed structure N_{lay} and a periodic multilayer (48 period, N_{lay}=96). As already noted, higher efficiency corresponds to a greater number of layers.

The higher efficiency, P, characterizing the (a) case with respect to the (c) case, is due mainly to the fact that the necessary spectrum reshaping in case (c), in order to produce the Gaussian curve tails, causes some lost of photons.

Differently, it is not possible to perform a straightforward comparison between the (b) and (d) cases because of the different used layers number. Concerning temporal modifications, cases (c) and (d) exhibit a higher T_{inc}/T_{refl} ratio, with respect to the (a) and (b) ones. This is related to the further pulse temporal reshaping induced by the spectral reshaping. In the second section of Table 2 the statistical parameters χ^2, standard deviation σ, and average values for P and T parameters derived from the already discussed stability test are reported.

5.4   Design for VUV spectral range

In this section we show and discuss the results of some multilayer designs in the VUV spectral region. Mo/Si multilayer at these relatively low energy have relatively low reflectivity peak with respect to other material couples. In particular, further reflectivity enhancement can be obtained using other material combinations like $B_4C/Si/Mo$ or Mg/SiC.
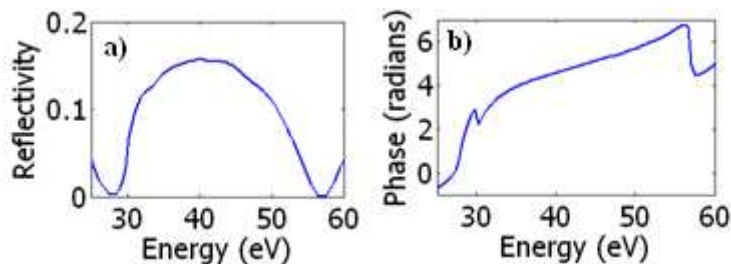
Fig. 17 *The reflectivity (case a)) and the phase (case b)) behaviors of an optimized $B_4C/Si/Mo$ multilayer.*

In the case of B$_4$C/Si/Mo multilayers (see Fig. 17) we have obtained a quite flat reflectivity in a relatively broad band but the second order phase chirp is less marked than the Mo/Si cases showed in the previously section (see section 5.3), the Mg/SiC (see Fig. 18) case, instead, have a second order phase chirp comparable with the Mo/Si cases showed in the previously section (see section 5.3) but have a narrower and lower reflectivity than the B$_4$C/Si/Mo case.
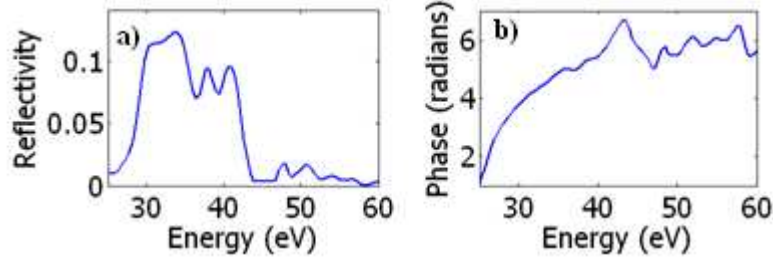
Fig. 18 *The reflectivity (case a)) and the phase (case b)) behaviors of an optimized Mg/SiC multilayer.*

## 5.5   Experimental characterization

In order to obtain the multilayer phase behavior by electrons photoemission signals, or total electron yields data (TEY) an innovative method developed in this PhD work, will be discussed.

The superimposition among the incoming and outcoming radiation originate a standing wave pattern into the multilayer structures and the TEY data has been assumed proportional to the standing wave intensity at the multilayer surface [5,9]. Thank to this approximation the formula describing the TEY signal becomes:

$$TEY(E) = C(E) \cdot I_0 \cdot (1 + R(E) + \sqrt{R(E)} \cdot e^{j\phi(E)})$$
(5.4)

where *C* carries the materials dependence of the *TEY* data, I_0 is the intensity of the incident radiation (the incoming radiation intensity has been normalized according to ring current and therefore constant varying to the energy values), *R* is the reflectivity and *Φ* is the multilayer phase.

In order to obtain the multilayer phase by the TEY signal the term $C \cdot I_0$ has to be deduced and two methods have been used for this purposes. The first one is the more precise method but it cannot be used in the spectral region where there is an absorption edge; for this reason in the restricted spectral region where there is the silicon absorption edge (see Fig. 19) the second method has been used. The innovation of these methods, in particular of the first one, is the insensitivity respect the multilayer materials morphology near to the surface samples.
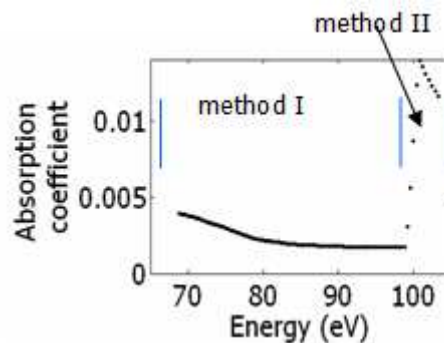
In fact when the multilayer has been exposed to an air environment at the top surface there is the formation of a non compact carbon film and a silicon oxide layer (see Fig. 20). In particular, the Carbon film can be quite difficult to control its consistence and thick because it is very irregular varying along the sample surface, moreover, the exposure to an EUV radiation of the sample in high vacuum condition over 10^{-7} mbar can give further change of the Carbon layer morphology [10,11]. In conclusion for an accurate deduction of the TEY data the experimental conditions in which we deduce the *C* term has to be the same as much as possible.
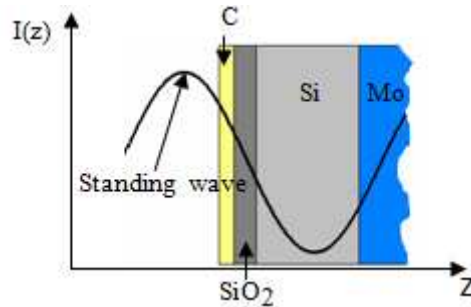
Fig. 20 *A schematic of the materials composition near the surface sample, the first layer is a very thin non compact carbon film due to the samples exposure to an air environment, the second one is a silicon oxide layer and then the Si-Mo alternated layers.*

5.5.1   Deduction of the C term (method I)

This method is based on the TEY data detected in two different incidence angles, where θ is the incidence angle that we need deduce the reflectivity and phase behavior and θ_1 is an angle slightly different from θ. Obtaining the information by these two signals we are insensitive to the samples surface morphology.

Into the approximation of $\theta_1 \rightarrow \theta$ the formula

$$E_{i+1} = E_i \cdot \frac{\cos\theta}{\cos\theta_1}$$ (5)

express the relationship between the energies with the same reflectivity and standing wave at the different incidence angles θ and θ_1 (see Fig. 21)

$$\begin{cases} R(E_{i+1},\theta_1) = R(E_i,\theta) \\ \phi(E_{i+1},\theta_1) = \phi(E_i,\theta) \end{cases}.$$ (6)
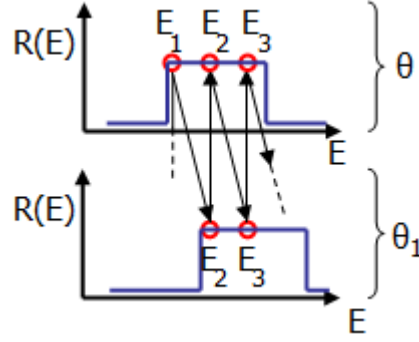
Fig. 21 *A schematic of the first relation (6) in the case of rectangular reflectivity.*

It worth to be noted that the same standing wave distribution means the same multilayer phase Φ.

Now, if we divide the TEY data detected at the different incidence angles θ and θ_1 and at the two different energies E_i and E_{i+1} linked by the formula (5)

$$\frac{TEY(\theta_1, E_{i+1})}{TEY(\theta, E)} = \frac{C(E_{i+1}) \cdot I_0 \cdot (1 + R(E_{i+1}, \theta_1) + 2 \cdot \sqrt{R(E_{i+1}, \theta_1)} \cdot \cos\phi(E_{i+1}, \theta_1))}{C(E_i) \cdot I_0 \cdot (1 + R(E_i, \theta) + 2 \cdot \sqrt{R(E_i, \theta)} \cdot \cos\phi(E_i, \theta))} \tag{7}$$

thank to the relations (6) we obtain a relationship, named $kost_i$, between the C terms at the energies E_i and E_{i+1}:

$$\frac{TEY(\theta_1, E_{i+1})}{TEY(\theta, E)} = \frac{C(E_{i+1})}{C(E_i)} = kost_i \tag{8}$$

In order to consider the different values of the area illuminated by the impinging radiation the previously formula can be corrected adding another term

$$C(E_{i+1}) = kost_i \cdot C(E_i) \cdot \frac{\cos(\theta)}{\cos(\theta_1)} \tag{9}$$

Finally thank to a recursive application of this formula we can reconstruct the relationship between the C terms at the different energies, but now, this relationships need to be tuned with an absolute reference.

The absolute references can be obtained by the TEY behavior at the incidence angle θ (see Fig. 22), in fact at the energies where we have a maximum o minimum value of the TEY signal there is a node or an anti-node of the standing wave distribution at the sample surface and consequently a π or a $\pi/2$ value of the multilayer phase Φ. Finally thank to this information the absolute reference can be obtained at one of these specific energies.
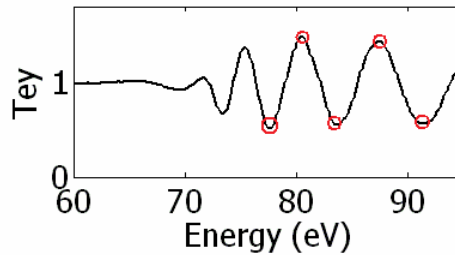
Fig. 22 *The sample I TEY signal, black line, with red circle the energies where we obtain the information of the multilayer phase.*

In this subsection the second method used to obtain the C trend is discussed. The incidence angle θ_1 is an angle where the multilayer have a reflectivity close to zero value in all the considered spectral range (E_{start}-E_{end}):

$$R(E_{start}\text{-}E_{end})\approx0. \tag{10}$$

Usually θ_1 is quite different respect the nominal one θ ($\theta_1>>>\theta$). Thank to the reflectivity approximation the TEY data detected at the incidence angle θ_1 can be approximated in this way:

$$TEY(E,\theta_1) = C(E,\theta_1)\cdot I_0 \cdot (R + 2\cdot\sqrt{R}\cdot\cos\phi+1) \cong C(E,\theta_1)\cdot I_0 \tag{11}$$

and finally we obtain the C term at θ incidence angle

$$C(E,\theta)\cdot I_0 = TEY(E,\theta_1)\cdot\frac{\cos\theta_1}{\cos\theta} \tag{12}$$

where the term ($\cos\theta_1/\cos\theta$) considers the different values of the area illuminated by the impinging radiation. The C term has been adjusted considering the non-zero escape depth of electrons using a correction factors for this effect [12].

5.6   Conclusions

Multilayers with high reflectivity, suitable phase compensation, and spectral amplitude reshaping can be designed by the optimization algorithm developed in this PhD work [13]. In addition the multilayer performances are not critically dependent on the structure parameters. Some test samples relative to a wide range of experimental conditions have been considered to prove the performances of the multilayer structures. The results show that multilayer structures can be designed accomplishing high reflectivity levels, pulse time preservation, or compression. Moreover, an innovative experimental method for the characterization of these optics by the electrons photoemission signals has been developed [14,15].

References

1   A.L. Aquila, F. Salmassi, F. Dollar, Y. Liu, and E.M. Gullikson; "*Developments in realistic design for aperiodic Mo/Si multilayer mirrors*"; Optics Express **14** (21), (2006);

2   A.-S. Morlens, P. Balcou, P. Zeitoun, C. Valentin, V. Laude, and S. Kazamias, "*Compression of attosecond harmonic pulses by extreme-ultraviolet chirped mirrors*", Opt. Lett. **30**(12), 1554–1556 (2005).

3   A.-S. Morlens, R. Lpez-Martens, O. Boyko, P. Zeitoun, P. Balcou, K. Varj, E. Gustafsson, T. Remetter, A. L'Huillier, S. Kazamias, J. Gautier, F. Delmotte, and M.-F. Ravet, "*Design and characterization of extreme-ultraviolet broadband mirrors for attosecond science*", Opt. Lett. **31**, 1558–1560 (2006).

4   A. Wonisch, U. Neuhusler, N. M. Kabachnik, T. Uphues, M. Uiberacker, V. Yakovlev, F. Krausz, M. Drescher, U. Kleineberg, and U. Heinzmann, "*Design, fabrication, and analysis of chirped multilayer mirrors for reflection of extreme-ultraviolet attosecond pulses*" Appl. Opt. **45,** 4147–4156 (2006).

5   A. Aquila, F. Salmassi, and E. Gullikson; "*Metrologies for the Phase Characterization of Attosecond EUV Optics* "; Optics Letters **33**(5), 455-457 (2008).

6   E. A. Spiller, Soft X-Ray Optics (SPIE, 1994).

7   "Center for X-ray Optics," http://www.cxro.lbl.gov/.

8   Y. Mairesse, A. de Bohan, L. J. Frasinski, H. Merdji, L. C. Dinu, P. Monchicourt, P. Breger, M. Kovacev, T. Auguste, B. Carré, H. G. Muller, P. Agostini, and P. Salières; "*Optimization of attosecond pulse generation*"; Phys. Rev. Lett. **93,** 163901 (2004).

9   A. Miyake, M. Amemiya, F. Masaki, and Y. Watanabe; "*Phase measurement of reflection of EUV multilayer mirror using EUV standing waves*"; J. Vac. Sci. Technol. B **22**(6), (2004).

10   J. Hollensheada and L. Klebanoff, "*Modeling radiation-induced carbon contamination of extreme ultraviolet optics*" J. Vac. Sci. Technol. B **24**, 64-82 (2006).

11   M.E. Malinowski, C. Steinhaus, W.M. Clift, L.E. Klebanoff, S. Mrowka, R. Soufli "*Controlling contamination in Mo/Si mutilayer mirrors by Si surface capping modifications*", Proc. SPIE **4688,** 442-453 (2002).

12   T. Ejima, "Formulae of Total Electron Yield for Multilayers: Extension of Pepper's Method," Jpn. J. Appl. Phys. Vol. **42**, 6459 (2003).

13   M. Suman, F. Frassetto, P. Nicolosi, and M.-G. Pelizzo; "*Design of aperiodic multilayer structures for attosecond pulses in the extreme ultraviolet*"; Applied Optics **46** (33), 8159-8169 (2007).

14   M. Suman, M. G. Pelizzo, D. L. Windt, G. Monaco, S. Zuccon, P. Nicolosi; "*Realization and characterization of XUV multilayer coating for attosecond pulses*", **92**[th] OSA (Optical society of America) annual meeting, Rochester (NY), USA 18-23th October.

15   M. Suman, Maria Guglielmina Pelizzo, D. L. Windt, G. Monaco, M. Gastaldi, P. Nicolosi; "Realization and characterization of XUV multilayer coating for attosecond pulses", Short Wavelength Laboratory Sources (Cost meeting), Dresden (De) 27th November.

Chapter 6: Multilayer coating for EUV lithography

6.1   Introduction

The multilayer structures typically used for EUV lithography (EUVL) consist in a Molybdenum and amorphous Silicon periodic repetition [1] . Because the system throughput (i.e., number of patterned wafers per hour) critically depends on the intensity of the radiation beam used to project the image of a mask on the photo-resist-coated wafer, high reflectivity is a crucial goal for photolithographic applications.

Since the optical system typically consists of 9-10 reflective elements, it is clear how even a very small change of the coating reflectivity can affect significantly the final performances of the system.

The typical multilayer structure used in EUV photolithography is made of a periodic multilayer structure tuned for peak reflectivity near 13.5nm. Typical structural parameters are a period of about 7 nm, and a Γ value of about 0.6.

The use of a thin interlayer of a different material, for example B_4C, is a well established technique that can be used to avoid interdiffusion at the interfaces. Peak reflectivity of approximately 70% has been obtained using B_4C interlayers [2], compared with 68-69% peak reflectance obtained in multilayers without any B_4C interlayers.

The multilayer (ML) optics in a EUVL system can be subdivided in four main groups: the collection optics, the condenser optics, the projection optics, and the mask. Each group has specific lifetime demands and different conditional environments. The main contamination sources affecting projection optics are carbon surface deposition and oxidation. The condenser optics used with a laser–plasma source are exposed to an environment quite different from that of the projection optics and, thus, require different solutions for lifetime improvements [3], since the direct effects of the plasma source can be sputtering, implantation, carbon deposition, oxidation due to debris contamination, and high heat load [4]. The topic of the EUVL multilayer designed and experimentally characterized in this PhD work is the development of multilayer coatings designed in order to improve the performances and lifetime of the projection optics for EUVL.

An important part of the EUVL multilayer coating is the capping layer, in a basic Molybdenum/Silicon multilayer, the highest peak reflectivity is obtained if the last layer is Molybdenum. However, this Molybdenum layer oxidizes in air and the formation of an oxide top surface degrades the peak reflectivity considerably [5]. Therefore Silicon is preferred as capping layer, since, after forming an oxide film, it becomes stable over time. However, in the EUVL harsh environment the degradation of the multilayer coating protected by the Silicon oxide capping layer is too fast respect the projection optics very stringent requirements for the operative conditions (of the order of 30000 exposure hours) [6].

The multilayer projection optics degradation is caused by hydrocarbon contamination or by the growth of an oxide layer on the top surface due to environmental contaminants present in the operating environment. Carbon contamination has been analyzed by J. Hollensheada and L. Klebanoff [7], who show that it originates from radiation-induced direct dissociation of carbon composite molecules. Contamination by

heavier hydrocarbons is most problematic, as light hydrocarbons can be removed by heating the optics up to about 30°C. Oxidation of multilayers in a photo-lithographic apparatus, which can be in fact a much more serious problem, is mainly due to the presence of water vapor in the residual gas. The oxidation depends on the interaction between EUV photons and the multilayer material: EUV photons cause primary electron emission by photoelectric effect and the primary electrons in turn generate secondary electrons by interaction with the atoms of the multilayer materials. The mean free path of secondary electrons in the materials is only a few nanometers, so only those electrons generated in the top few layers [8-10] can reach the vacuum. Free radicals created by secondary electrons having sufficient energy can bond to the capping layer atoms and form oxides on the surface, or diffuse into or through the top layer and cause oxidation, a schematic explanation of this phenomena is showed in Fig. 1.
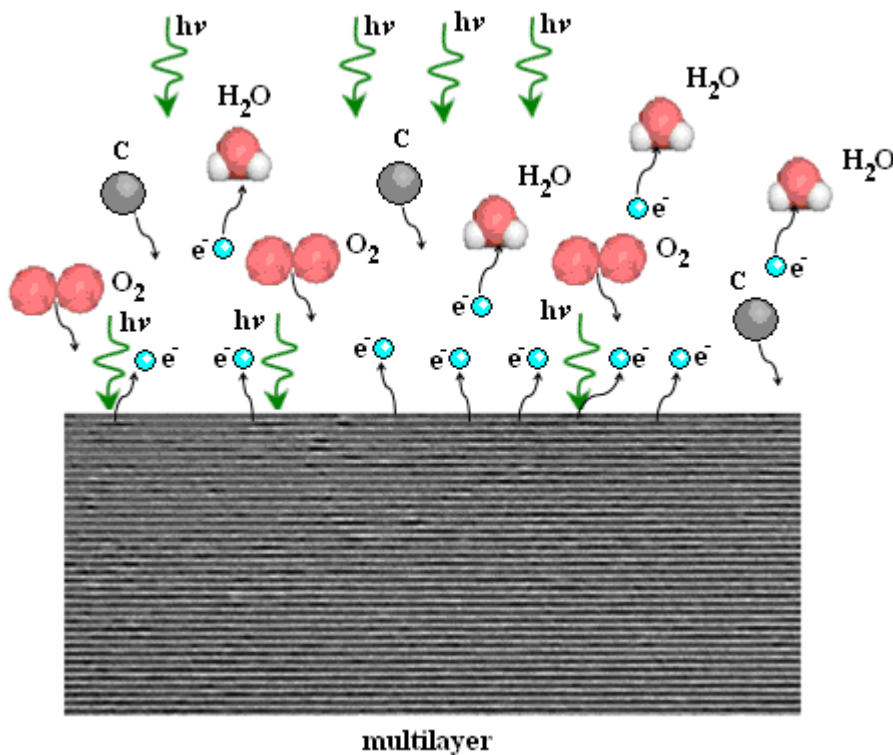
Fig. 1 *A schematic of the phenomena involving the multilayer surface in the EUV lithography environment. The "e^{-}" are the photo-emitted electrons, the "hv" are the photons of the impinging radiation, the "H$_2$O" are the water molecule and with C the carbon atoms are be represented.*

To overcome the problem of surface contamination and oxidation, the use of protective capping layers such as Ru has been investigated [10-12]. An extensive analysis of the critical parameters affecting the EUV-induced damage of Ru capping layer has been performed by Hill et al. [12].

In the last years innovative capping layers consisting of two layers have been proposed in [4]. A top layer protects the structures from the environment, while the second one acts as a diffusion barrier between the top and the multilayer structure beneath. Material combinations considered include Ru/B$_4$C and Ru/Mo. Structures with Ruthenium layers thicker than 2.3nm have been demonstrated to be quite stable against environmental agents [4], however if they are deposited on an optimized periodic structure will significantly

reduce the reflectivity of the coating. Even a reflectivity reduction of only 1% can result in an overall 18% reduction for a ten element optical system, such as those now being developed for EUV lithography.

In past works, aperiodic structures have been designed first to offer best performance in term of peak reflectivity and the incorporation of a capping layer was considered subsequently. By using this approach, solutions have not always offered significantly higher performance with respect to periodic structures: for example the performance of a periodic or an aperiodic multilayer structure with an a-SiO$_2$ capping layer are quite similar.

Only more recently has the need to protect the structure by a resistant capping layer lead to the optimization of the structure as a whole. Some commercial tools are available to optimize thin layer structures, as for example TFCalc [13]. TFCalc can allow optimization of some parameters of the structures using a global optimization procedure, but only by assuming ideally smooth interfaces. Aperiodic Molybdenum/amorphous Silicon solutions, with possibly the insertion of a third needle layer, have been optimized under some proposed capping layers. In the proposed design typical thickness of the capping layers considered are of the order of 1.5-1.7 nm and last layer under the capping is amorphous Silicon. In the case of a two component Molybdenum/amorphous Silicon multilayer (without the needle layer) the optimization results in a gradual, smooth variation of the layer thickness of the two materials, while the period remains constant, around 7 nm.

Different possible materials can be in principle selected as capping layer for aperiodic structures if the choice is based on the refractive index properties [11]. However, in addition to optical properties requirements, capping layer materials need to meet additional criteria for acceptable performance, as stated above. In particular, they have not to inter-diffuse with the material underneath and they have to be oxidation resistant in a water-vapor environment.
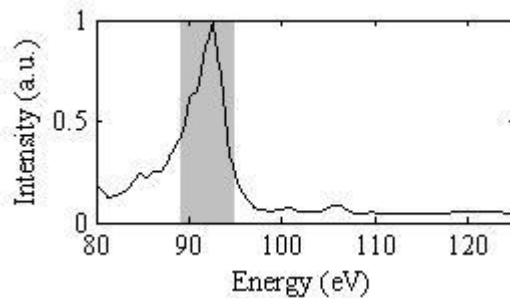
Fig. 2. The typical spectrum emitted by a tin laser plasma, the shadowed area corresponds to the spectral components utilized by multilayer optics for the EUV lithography.

6.2 Aperiodic optimized multilayer properties

The specific merit function used in order to maximize the reflected EUV flux is $\int R(\lambda)^M * I(\lambda) d\lambda$, where $I(\lambda)$ is the source spectrum, $R(\lambda)$ is the reflectivity of the structure, and M is number of mirrors in the apparatus; in this work we have assumed M=10, and a Sn laser-produced plasma source has been assumed.

(Comparable coatings could also be developed for other sources as well.) In Fig. 2 we show the typical spectrum emitted by a Sn laser plasma.

Three different examples of optimized a-periodic solution are reported in Tab. 1, ML1, ML2, ML3, together with the parameters related to standard periodic multilayers ML4 and ML5 and periodic multilayers with outermost Si layer optimized, according to ref. [11], ML6 and ML7 used for comparison. All structures have been optimized for a 10° incidence angle. ML1 has a capping layer of RuO_2/Mo while ML2 and ML3 of RuO_2/B_4C where RuO_2 has been considered in order to take into account the oxidation of the uppermost Ru layer. The structure ML2 has been optimized by keeping constant beside the capping layer also the B_4C interlayer thicknesses, while these latter have been left free parameters in the optimization of the structure ML3. ML4 and ML5 have standard periodic structures, while ML6 and ML7 are standard periodic structures with the last a-Si layer thickness underneath the capping layer optimized.
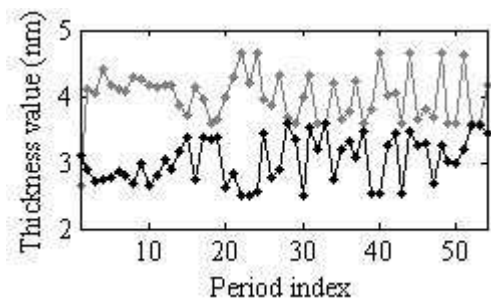
Fig. 3. A-periodic structure layers thickness: in gray a-Si, in black Mo. The abscissa represents the increasing period number starting from the most internal to the external layer.
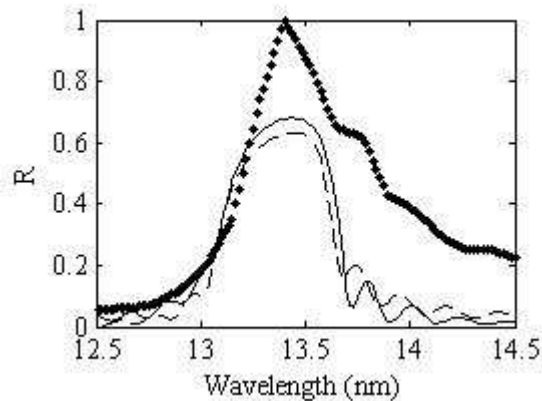
Fig. 4. ML1 and ML4 structures reflectivity curves: continuous curve, ML1 and dashed curve, ML4. In dotted line the Sn spectrum relative intensity is reported.

The layer distribution of ML1 is reported in Fig. 3 as an example, from which the chaotic distribution of the thickness (in this context the term chaotically is intended to mean that the values of the thicknesses can not be described by or do not follow any particular order or trend) is clear. In Fig. 4 its corresponding reflectivity curve is reported together with the one of a standard periodic structure ML4 and the normalized Sn source spectral emission distribution; a rms roughness of 0.5 nm at each interface has been used in all

simulations. It is clear both the increase of the peak reflectivity and the better match with the radiation spectrum on the low wavelength wing of the reflectivity curve. Although the peak reflectivity improvement is of only about 3% absolute, the final improvement for a multi-element optical system is considerable. The performances of a lithographic apparatus with ten subsequent mirrors are estimated in term of percentage of reflected spectrum as:

$$MF = 100 \cdot \frac{\int R(\lambda)^{10} \cdot I(\lambda) d\lambda}{\int I(\lambda) d\lambda}$$

where MF is the merit function of the system.
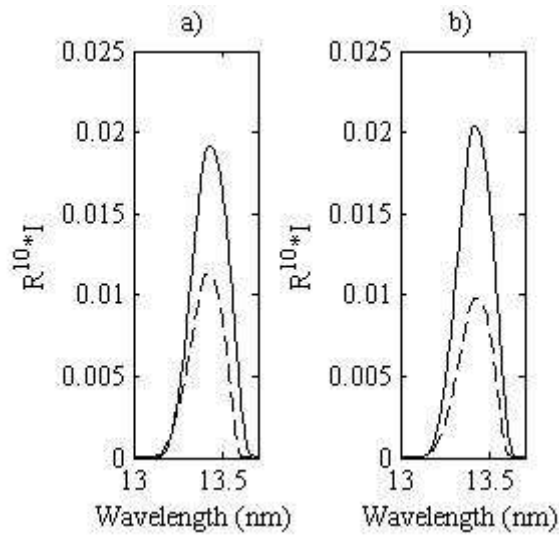
Fig. 5. Intensity after ten reflection of Sn spectrum are presented for the a-periodic ML1 and period periodic ML4 structures in Fig.5 a), while in Fig.5 b) the same results for the a-periodic ML2 and periodic ML5 structures; in both figures, in dash dotted line the performances of the periodic structures while in continuous line the ones of the a-periodic structures are reported. I is the spectrum of the source normalized to the peak emission, which is plotted in Fig. 4.

In Fig.5 the intensity computed after ten reflections of Sn spectrum is reported: in Fig 5 a) for the a-periodic ML1 and periodic ML4 structures, while in Fig. 5 b) for the a-periodic ML2 and periodic ML5 structures; in both figures, in dash dotted line the performances of the periodic structures (ML4 and ML5), while in continuous line the ones of the a-periodic structures (ML1 and ML2) are reported. The calculations show an improved performance of a factor 1.79 for the structure ML1 with respect to a standard periodic multilayer (structure ML4), similarly a factor respectively of 2.15 and 2.18 has been obtained for the structures ML2, ML3 with respect to a standard periodic multilayer structure ML5. The performance of the design proposed by Singh and Braat [11] has been also evaluated, the results, not reported in Fig. 6 for clarity, show that the structure ML6, is better than ML4 by a factor 1.75 while the ML7, has higher reflectivity than ML5 by a factor 2.10.

	Material types	Thickness
ML1		
Cap layer	RuO_2/Mo	2.3 nm /2.0 nm
A-periodic structure	a-Si min/max	2.41 nm /4.29 nm
	Mo min/max	2.68 nm /3.55 nm
ML2		
Cap layer	RuO_2/ B_4C	2.3 nm /2.0 nm
A-periodic structure	a-Si min/max	1.9 nm /4.0 nm
	B_4C	0.4 nm
	Mo min/max	2.5 nm /3.0 nm
	B_4C	0.25 nm
ML3		
Cap layer	RuO_2/ B_4C	2.3 nm /2.0 nm
A-periodic structure	a-Si min/max	1.9 nm /3.9 nm
	B_4C	0.23 nm /0.39 nm
	Mo min/max	2.37 nm /3.38 nm
	B_4C	0.22 nm /0.42 nm
ML4		
Cap layer	RuO_2/Mo	2.3 nm /2.0 nm
Periodic structure	a-Si	4.19 nm
	Mo	2.79 nm
ML5		
Cap layer	RuO_2/ B_4C	2.3 nm /2.0 nm
Periodic structure	a-Si	3.86 nm
	B_4C	0.25 nm
	Mo	2.47 nm
	B_4C	0.4 nm
ML6		
Cap layer	RuO_2/ B_4C	2.3 nm /2.0 nm
Periodic structure	a-Si	3.86 nm
	Mo	2.47 nm
ML7		
Cap layer	RuO_2/ B_4C	2.3 nm /2.0 nm
Last Si layer	a-Si	2.075 nm
Periodic structure	a-Si	3.88 nm
	B4C	0.25 nm
	Mo	2.47 nm
	B4C	0.4 nm

Table 1. *Structural parameters of ML1, ML2, ML3 and ML4.*

Let's to discuss the reported results. The optimum structures have an a-periodicity which is distributed through all the layer thicknesses. The superposition of the incident and reflected wave electromagnetic fields results in a standing wave field distribution in the ML structure. As an example, the standing wave for the structure ML2 is reported in Fig. 6, together with the one for the periodic structure ML4. The figure shows that the a-periodic structures are characterized by having the property that the capping layer is spatially shifted with respect to the position of the standing-wave node at the top of the ML. A similar effect can be obtained reducing (optimizing) the last Si layer [11], like in the case of ML6 and ML7. As a result of this design, the energy absorption in the top layers of the ML is reduced. This has multiple effects: reflectivity improvement, slowing down of oxidation and relative insensibility to the capping layer optical properties, with the final result of improved lifetime of the coating. In the following we will discuss each of these effects.
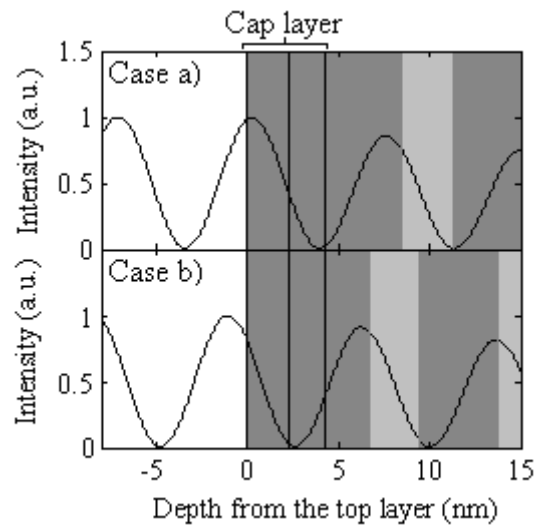

Fig. 6 *Standing wave pattern into the structures ML4 (case a)) and ML1 (case b)).*

The reflectivity improvement derives from the fact that EUV radiation can penetrate deeper into the structure, allowing more layers contributing to the final reflectivity; moreover differently from the multilayers where only the last Si layer is optimized, the chaotic thickness distribution of the more internal layers allows a slight further improvement of the reflectivity by obtaining a larger reflectivity bandwidth and a better match with the relatively stronger long wavelength side of the source spectrum, Fig 4.

The standing wave shift with a minimum of the field into the capping layer should lead to a reduction of the photons absorbed in the top layers of the multilayer structure and, as above mentioned, because of the oxidation dependence from the secondary electron generated at the surface of the multilayer the mechanism of oxide formation would be slowed down [8].

The shift into the capping layer of the standing wave field minimum has also the effect of reducing the criticality of the capping layer optical properties for the final performance. This can be extremely important in photolithography applications, where the harsh environmental conditions can affect the capping layer

optical properties, for example through oxidation and/or carbon deposition. In conclusion this result, by making the reflective performance of the ML structure less sensitive to the capping layer properties, can further contribute to final lifetime improvement of the optics.
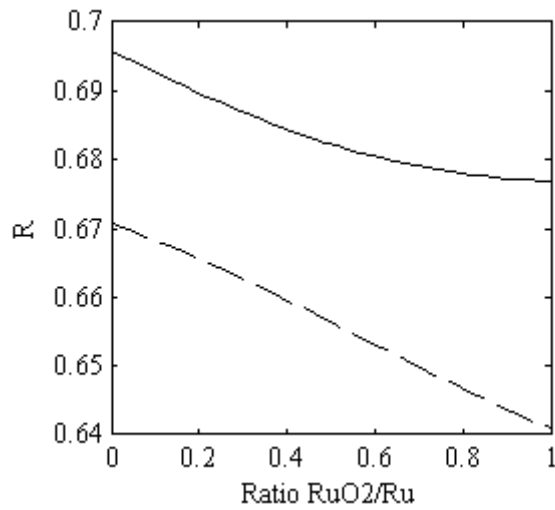
Fig. 7 Reflectivity peak as a function of the capping layer oxidation, in continuous line ML1 case and in dashed line ML4 case.
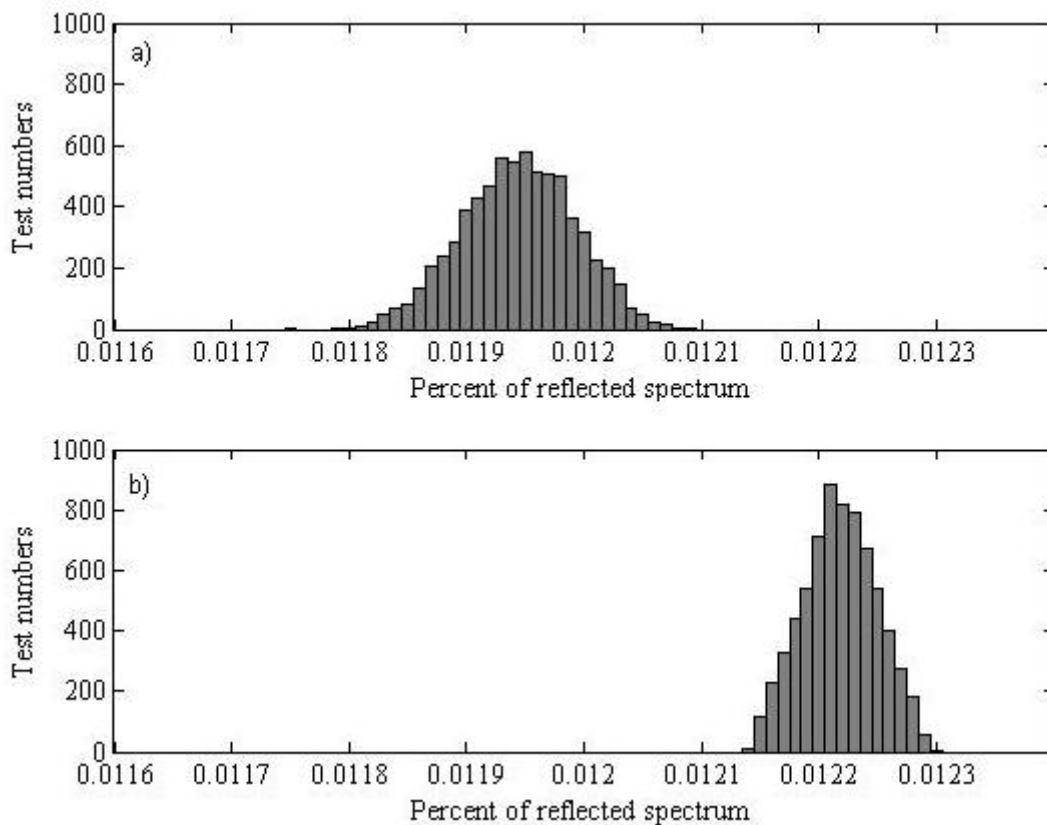
Fig.8 Histogram of the thickness deposition error tests for ML1 and ML4 structures.

In addition this opens the possibility to study new capping layer solutions, in fact new materials can be explored even some which could have been neglected, due to their relatively high absorption. Last but not

least a further relevant aspect is related to the possibility of optimizing the performance of the a-periodic structure by taking into account the oxidation of the uppermost layer. In Fig. 7 the peak reflectivity versus the oxide fraction of the uppermost Ru layer is reported for the a-periodic ML1 structure and the corresponding periodic one, ML4. It is clear that the reflectivity decrease due to oxidation is definitely lower for the a-periodic structure than for the periodic one.

Structures	Mean percentage of reflected spectrum	Standard deviation
ML1	0.4108	0.00106
ML6	0.4016	0.00170

Table 2. Second order statistical analysis.

Some tests have been performed to compare the sensitivity to layer thickness errors occurring during deposition of a-periodic structures with standard periodic ones with outermost Si layer optimized. The structures ML1 and ML6 have been considered for comparison, since they show quite similar performance. In order to do so, the percentage of reflected spectrum, calculated as eq. (1), has been evaluated for 7000 different structures. These have been derived from the nominal ones by a random, with uniform probability distribution, variation of each layer thickness within ±0.01nm (which is a typical error during a deposition process). A second order statistical analysis (see table 2 and Fig. 8) of the results confirms that ML1 is more stable to random layer thickness variation than ML6, with a factor 2/3 narrower standard deviation.

This result can be justified by the fact that the redistribution of the interferential optical paths in the chaotic structures is more stable than the periodic case, in fact the optimization algorithm has been structured for focus toward stable MLs domain regions. Moreover, by observing Fig. 8 we can argue that with ±0.01nm range of deposition errors the performance of the structure ML1 is always higher than that one of ML6.

6.3   Experimental results

In order to experimentally test the improved performance expected from our simulations, prototype Mo-Si multilayer structures, both standard periodic and aperiodic, have been designed, fabricated and tested. The periodic multilayers have been designed without modifying the last a-Si layer thickness in order to experimentally test the properties deriving from the standing wave shift.

In the design optimization procedure a RuO_2/Mo capping layer, in order to take into account the oxidation of the Ru uppermost layer, and an interface width of 0.5 nm have been assumed. Accordingly the optimization algorithm searched for solutions among those less sensitive to the radiation absorption in the capping layer. In addition to the Ru-capped multilayers just described, we also simulated the performances of the multilayer structure capped with Pt and a-Si as well. In the latter case the a-Si uppermost layer was

allowed to form a 1 nm thick oxide layer. In Fig. 9 the results of our simulations are reported: while the a-periodic structure shows higher reflectivity than the periodic structure in the case of multilayers containing Pt capping layers, the opposite is true for samples containing a-Si capping layers. (Unfortunately it is generally recognized that an a-Si capping layer is not a suitable solution for a photolithographic apparatus, due to poor resilience to oxidation.) Furthermore, by comparing the simulated performance of the different periodic and a-periodic structures, we find that the new structures presenting suitable shift of the standing wave node, both periodic, with last Si layer optimized, or a-periodic, are less sensitive to the choice of capping layer while in the case of periodic structures of standard design a strongly absorbing capping layer causes a significant reduction of reflectivity.
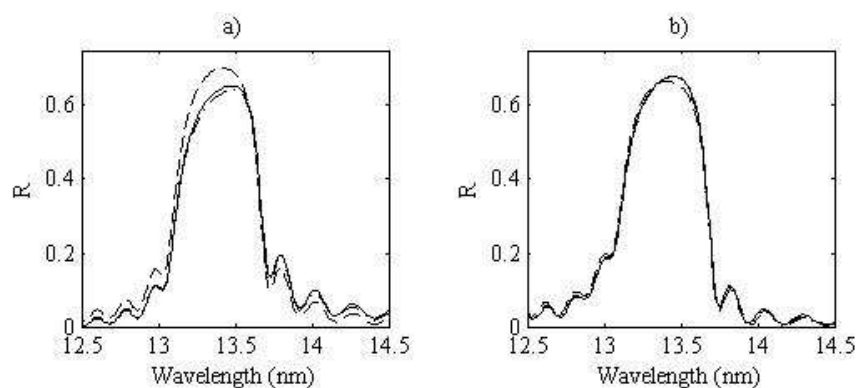
Fig. 9. Theoretical calculations of the reflectivity curves: case a) standard periodic ML, case b) a-periodic chaotic ML; in both cases: continuous line, MLs with Ru/Mo capping layer; dash dotted line, ML with Pt/Mo capping layer; and dashed line, ML with a-Si/Mo capping layer.

Prototype Mo/Si multilayers were deposited by magnetron sputtering in Reflective X-ray Optics' (RXO) "S-Gun" deposition system [14]. Multilayer structures containing 50 periods tuned near 13.5 nm were deposited onto 3" Si (100) wafers. Both periodic and aperiodic coatings were produced, with either 4.05nm/2nm Si/Mo, 2.0 nm/2.0nm Ru/Mo, or 1.0 nm/2.0 nm Pt/Mo capping layers. As already said the periodic structures do not provide any standing wave node shift and have been used to prove the noticeable effect deriving from suitable shift of the standing wave to put its node coincident with the capping layer.
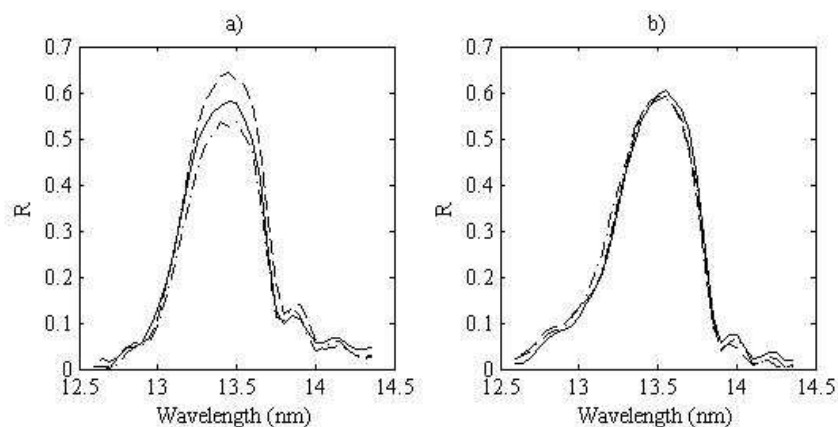
Fig. 10. Experimental reflectivity curves: case a) standard periodic ML, case b) a-periodic chaotic ML; in both cases: continuous line, MLs with Ru/Mo capping layer; dash dotted line, ML with Pt/Mo capping layer; and dashed line, ML with a-Si/Mo capping layer. The experimental measures have an experimental uncertainty of 10^{-3}.

Samples were tested through EUV and X-ray reflectivity measurements as well as with secondary electron yield measurements. EUV reflectance was measured immediately after deposition and then again a few months later when secondary electron yield measurements were performed. The EUV reflectance was measured after deposition as a function of wavelength from 12.5 to 14.5 nm in RXO's laser-plasma reflectometer.[14]

In Fig. 10 the experimental reflectivity curves for periodic and aperiodic Mo/Si structures having a-Si/Mo, Ru/Mo, and Pt/Mo capping layers are shown (The experimental measures have an experimental uncertainty of 10^{-3}). The peak reflectivity values are listed in Table 3. Note that because the deposition rates drift slightly over time in this particular deposition system, the multilayers do not all peak at the exact same wavelength; however the various reflectance curves in Fig. 10 have been slightly shifted in wavelength to facilitate comparison. Note also that the peak reflectance measured in the laser-plasma reflectometer has been verified to be systematically lower by about ~2% absolute compared with measurements made using synchrotron radiation at the ALS facility in Berkeley.

	ELETTRA RXO	ELETTRA RXO
	Periodic	A-periodic
Ru/Mo	0.563	0.612
	0.582	*0.605*
Pt/Mo	0.549	0.598
	0.537	*0.592*
a-Si/Mo	-------	-------
	0.644	*0.591*

Table 3. *Peak reflectance values for the six samples: italic, values measured at RXOLLC and underlined, values measured at ELETTRA.*

The experimental results shown in Fig. 10 are consistent with the theoretical simulations in Fig. 9: a-periodic multilayer structures have better performance than the periodic structures in the case of Ru/Mo and Pt/Mo capping layers. Due to the high transparency of a-Si at this wavelength, however, the situation for the case of the aperiodic Mo/Si multilayer with a-Si as capping layer shows different behavior: here the periodic structure gives the best reflectivity. On the other hand, as discussed above, a-Si protective capping layers are not suitable for photolithographic applications due to poor resistance to oxidation [8].

The X-ray reflectance (XRR) of our prototype samples was measured from 0 to 6 deg (grazing angle) using Cu Ka (1.54Å) radiation. The XRR curves are reported in Fig. 11 for periodic, Fig. 11 (a), and aperiodic, Fig. 11 (b), structures with Ru capping layers. Both the experimental XRR curves and the fits

are reported. Similar data have been obtained for the other samples listed above as well. The XRR data show clearly Bragg peaks up to the 9th order for the periodic case, while in the aperiodic case the peak amplitude rapidly decreases for the higher orders, and so peaks only up to the 5th order can be clearly distinguished from the noise. The XRR period was adjusted in the calculations to match the measured data for the periodic structures: the periods were thus found to be 7.05 nm, 6.985 nm, and 6.875 nm. (The decrease in period is the result of the drift in deposition rate characteristic of the deposition system mentioned above.) In the case of the aperiodic multilayers, no fitting was performed: the calculations shown were computed using the nominal design parameters. The good agreement between measurements and calculations confirms that the actual layer thicknesses deposited are reasonably close to the design layer thicknesses in all cases.
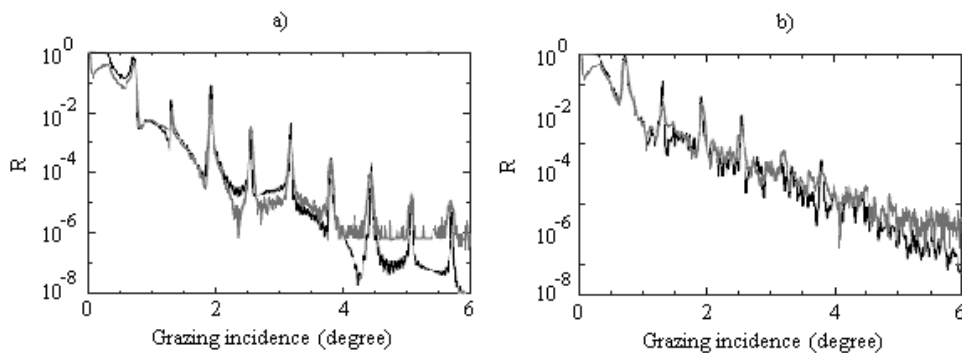
Fig. 11. *X-ray reflectance (XRR) measured from 0 to 6 deg (grazing) using Cu Kα (1.54Å) radiation. The structures considered are periodic (case a)) and a-periodic (case b)) over-coated by Ru/Mo capping layer. In both cases in gray the measured data and in black the fitting result.*

From the measured reflectivity curves (Fig. 10) it is clear that the aperiodic structures show a behavior substantially insensitive to the capping layer material while in the case of periodic structures the reflectivity curves show a significant decrease of the peak with the different capping layer materials, Pt, being the most highly absorbing material, giving the worst performance.

Several months (6 months) after the coatings were deposited, reflectivity measurements and secondary electron emission measurements were performed at the bending magnet BEAR beam line of the ELETTRA synchrotron (Trieste - Italy) on samples containing Ru and Pt capping layers (in Fig. 12 a schematic of the experimental setup used at the BEAR beam line). The primary electrons emitted via the photoelectric effect by monochromatic photons in an energy interval around the multilayer working wavelength generate secondary electron emission. These secondary electrons have a mean free path of only a few nm so the measured signal originates from a very thin layer below the top surface of the multilayer structure. Consequently the secondary electron signal can be related to the amplitude of the standing wave field resulting from the superposition of the incident and reflected waves at the top surface of the multilayer structure.
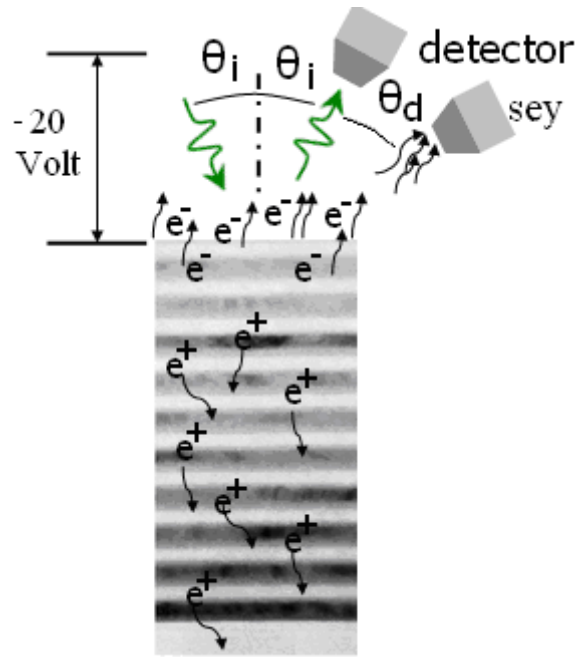
Fig .12 *A schematic of the experimental setup used at the BEAR beamline for the characterization of the samples. A 20 Volt of collection voltage has been used, θ_i (5°) is the incidence angle, e^- are the electrons photoemitted, θ_d is the configuration used for the secondary electron yields signal detection (40°).*

The reflectivity of periodic and a-periodic samples having Pt and Ru capping layers have been measured in both s and p polarization. In Fig. 13 the reflectivity curves for 10° incidence angle, average polarization and in the energy interval between 85 and 100 eV are reported.
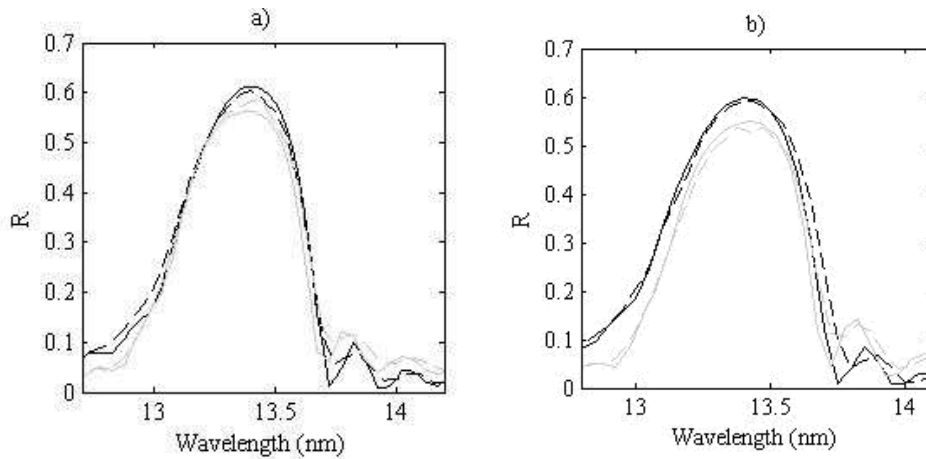

Fig. 13. *Experimental reflectivity curves measured at ELETTRA and RXO. In the case a) a-periodic and periodic structures with Ru/Mo capping layer, in the case b) a-periodic and periodic structures with Pt/Mo capping layer; in both cases: continuous black line, a-periodic structure measured at ELETTRA; dash dotted black line, a-periodic structure measured at RXO; continuous gray line, periodic structure measured at ELETTRA; and dash dotted gray line, periodic structure measured at RXO.*

For comparison the curves previously measured at RXO are shown as well. In order to correctly compare these data, we must take into consideration that the peak reflectivity values measured at RXO using a laser-

plasma reflectometer are slightly lower than the values measured using synchrotron radiation at the ALS, so we expect to find the same behavior for the ELETTRA data. It is clear that the two a-periodic samples show essentially the same peak reflectivities as measured immediately after deposition. These data confirm the superior performance of the coatings with standing wave shift. Furthermore, the periodic samples show further reduction of the reflectivity compared with the values obtained just after deposition, and in particular this decrease is greater for the Ru-capped coatings than for Pt–capped coatings. This fact could be ascribed to Ru oxide formation at the top surface, as Pt is known to be more chemically stable.

Photoemission measurements were performed only in s polarization, as theoretical evaluations showed that the standing wave field distribution in the uppermost layers of the structure was essentially independent on the polarization state of the radiation. The electron analyzer was set at 45° from the normal to the sample surface in order to have the best performance. The sample was positively biased at 20 V thus giving more kinetic energy to the escaping electrons, and consequently nearly saturating the detector, and allowing us to set the analyzer electron energy window to begin at 20 eV. Photoelectron detection at the exit of the analyzer was measured using a microchannel plate. The energy of the impinging radiation beam was scanned through the peak of the measured reflectivity curve of each ML while the angle of incidence was maintained at 10°.

The normalized, integrated signal of secondary electrons (SEY), from 20 to 50 eV is shown versus the scanning radiation energy in Fig. 14 for both periodic and aperiodic samples. In the same figure, for comparison, we show the calculated standing wave field intensity integrated below the vacuum interface of the ML. In order to take into account the mean free path, L, of secondary electrons in the materials, the intensity, I(z), versus the depth from top of the ML structure has been weighed according to the formula $I(z) \cdot e^{-(z/L)}$ [7]. L is about 1 nm for the materials considered. The ML parameters derived from the XRR measurements were used in the case of periodic structures, while for the a-periodic structures a constant correction to each layer was applied in order to properly match the measured reflectivity curves. In particular, the thickness of each layer was reduced by 0.35 Å in the case of Ru capped structures, while the thickness of each layer was increased by 0.15 Å for the Pt capped structure (see Fig 13). The good correspondence between the theoretical and experimental curves confirms that the signals correspond to the standing wave distribution in the ML.
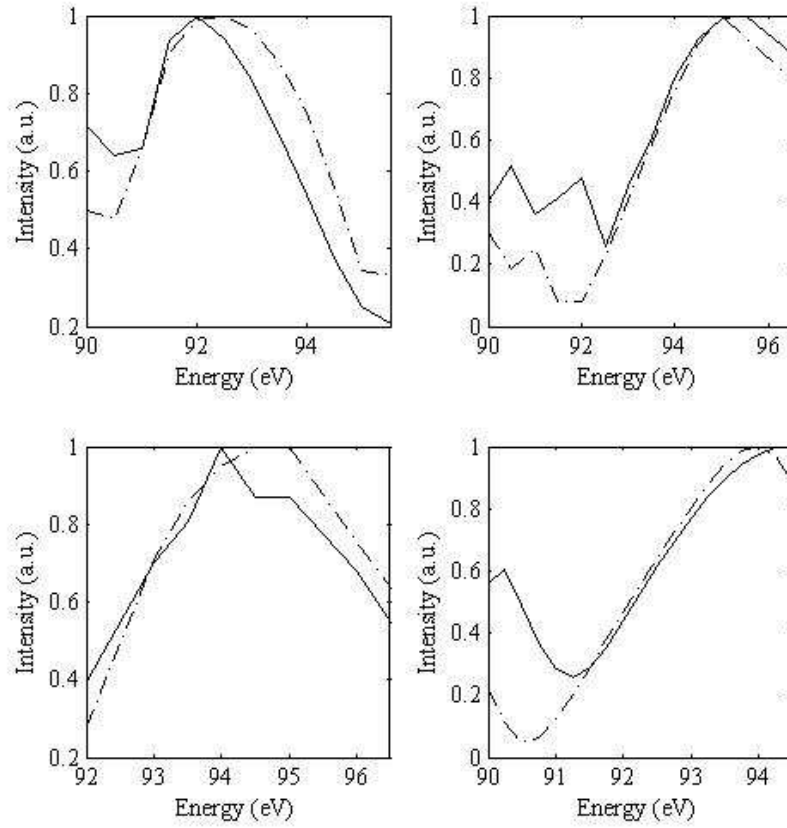
Fig. 14. Experimental (continuous line) results of photoemission compared with theoretical (dash dotted line) prediction of the standing wave intensity in the top of the ML, see text. In sub section a) the periodic case over capped by ruthenium, in sub section b) the a-periodic case over capped by ruthenium, in sub section c) the periodic case over capped by platinum and in sub section d) the a-periodic case over capped by platinum.

Finally we compare the SEY at the photon energy corresponding to the reflectivity peak for each multilayer studied. In Table 4 we list the ratio between the SEY values measured for the various samples. The SEY ratio between aperiodic and periodic ML structures having Pt capping layers is 0.022, while the ratio for structures having Ru capping layers is 0.54,. The SEY ratio between aperiodic structures having Pt and Ru capping layers is 0.057, while the SEY ratio for periodic structures is 1.42. These measurements have random errors of the order of a few percent. As secondary electrons can promote oxidation [10], the SEY data presented in Table 4 therefore further suggest that the a-periodic structures, or structures with minimum of standing wave at the cap-layer position, will be more resilient to oxidation, with a-periodic Pt-capped samples likely having greater resilience relative to Ru-capped coatings. It should be noted that Pt has not been considered for use as a capping layer material for EUVL coatings until now, because of its strong absorption at 13.5 nm; however our results suggest improved performance of Pt-capped multilayers relative to Ru-capped multilayers.

	Periodic Ru/Mo
(A-periodic Ru/Mo)/(Periodic Ru/Mo)	54 %
(A-periodic Pt/Mo)/(Periodic Pt/Mo)	2.2 %
(A-periodic Pt/Mo)/(A-periodic Ru/Mo)	5.7%
(Periodic Pt/Mo)/(Periodic Ru/Mo)	142 %

Table 4. The ratio between the total secondary electron yield signals taken at the reflectivity peak.

6.4   Conclusion

EUV ML structures have been in order to achieve the highest possible reflectivity at 13.5 nm while simultaneously yielding low sensitivity to capping layer optical properties. Prototype samples of these structures have been fabricated and tested, they are made of Mo/a-Si bilayers with Ru, Pt and a-Si capping layers. EUV reflectance measurements were performed after deposition using a laser-plasma reflectometer, and also 6 months later using synchrotron radiation. XRR and secondary electron yield measurements have been made as well. The experimental results demonstrate the superior performance of capped, a-periodic structures compared with conventional periodic coatings, showing higher reflectivity, lower secondary electron emission, better stability over time, and insensitivity to the choice of capping layer material. These structures are useful for EUV lithography applications in order to realize significant performance enhancements. The results obtained in this framework has been published in two papers [15-16] and an international patent [17] has been filled.

References

1   P. B. Mirkarimi, S. Bajt *et al.* "*Mo/Si and Mo/Be multilayer thin films on Zerodur substrates for extreme-ultraviolet lithography*", Applied Optics Vol. 39(10), pp. 1618-1625, 2000

2   S. Bajt, J. B. Alameda *et al.* "*Improved reflectance and stability of Mo/Si multilayers*", Optical Engineering 41(08), p. 1797-1804, Donald C. O'Shea; Ed., 2002

3   L. E. Klebanoff, P. A. Grunow, S. Graham, W. M. Clift, A. H. Leung, and S. J. Haney, "*Environmental data from the Engineering Test Stand*," Proc. SPIE 4688, 310–315 (2002).

4   S. Bajt, H.N. Chapman,N. Nguyen, J. Alameda, J.C. Robinson, M. Malinowski, E. Gullikson, A. Aquila, C. Tarrio, and S. Grantham, "*Design and performance of capping layers for extreme-ultraviolet multilayer mirrors,*" Appl. Opt. 42, 5750–5758 (2003).

5   Underwood et al, Applied Optics 32, p. 6985, 1993

6   S. Wurm and K. Kemp, "*SEMATECH pushes extreme ultraviolet lithography forward,*" http://spie.org/x8865.xml.

7   J. Hollensheada and L. Klebanoff, "*Modeling radiation-induced carbon contamination of extreme ultraviolet optics,*" J. Vac. Sci. Technol. B **24**, 64-82 (2006).

8   M.E. Malinowski, C. Steinhaus, W.M. Clift, L.E. Klebanoff, S. Mrowka, R. Soufli "*Controlling contamination in Mo/Si mutilayer mirrors by Si surface capping modifications*", Proc. SPIE **4688,** 442-453 (2002).

9   K. Motai; H. Oizumi; S. Miyagaki; I. Nishiyama; A. Izumi; T. Ueno; Y. Miyazaki; A. Namiki., "*Atomic hydrogen cleaning of Ru-capped EUV multilayer mirror,*" Proc. SPIE **6517,** 65170F1 – 65170F8 (2007).

10   S.Bajt, Z. R. Dai, E. J. Nelson, M. A. Wall, J. Alameda, N. Nguyen, S. Baker, J. C. Robinson, J. S. Taylor, M. Clift, A. Aquila, E. M. Gullikson, N. V. Ginger Edwards "Oxidation *resistance of Ru-capped EUV multilayers,*" Proc. SPIE **5751**, 118-127 (2005).

11   M. Singh, J.J.M.Braat, " *Capping layers for extreme-ultraviolet multilayer interference coatings,*" Opt. Lett. **26**, 259-261 (2001).

12   S. B. Hill, I. Ermanoski, C. Tarrio, T. B. Lucatorto, T. E. Madey, S. Bajt, M. Fang, M. Chandhok "*Critical parameters influencing the EUV-induced damage of Ru-capped multilayer mirrors,*" Proc. SPIE **6517**, 65170G (2007).

13   M. Singh, J. M. Braat, "*Design of multilayer extreme – ultraviolet mirrors for enhanced reflectivity*", Applied Optics Vol.39, No.13, p.2189, 2000

14   D. L. Windt and W. K. Waskiewicz, "*Multilayer facilities for EUV lithography,*" J. Vac. Sci. Technol. B **12**, 3826-3832 (1994).

15   M. Suman, M. G. Pelizzo, P. Nicolosi and D. L. Windt, "*Aperiodic multilayers with enhanced reflectivity for extreme ultraviolet lithography,*" Appl. Opt. **47,** 2906–2914 (2008).

16   M. G. Pelizzo, M. Suman, G. Monaco, P. Nicolosi, and D. L. Windt , "*High performance EUV multilayer structures insensitive to capping layer optical parameters*" *Optics Express*, Vol. 16, Issue 19, pp. 15228-15237 (September 2008)

17   PCT/EP2007/060477

Scientific publications and presentations

Patents:

1. **M. Suman**, Pelizzo M. G., Nicolosi P., and Windt L. D, "A-periodic multilayer structures" PCT/EP2007/060477.

Papers:

1. **M. Suman**, Frassetto F., Nicolosi P. and M.G.Pelizzo, "Design of a-periodic multilayer structures for attosecond pulses in the EUV", Applied Optics Vol. 46 No. 33 20th November 2007.

2. **M. Suman**, Pelizzo M. G., Nicolosi P., and Windt L. D., "A-periodic multilayers with enhanced reflectivity for EUV lithography" applied optics, Vol. 47, Issue 16, pp. 2906-2914 (June 2008).

3. Pelizzo M. G., **M. Suman**, G. Monaco, Windt L. D. and Nicolosi P. "A-periodic EUV multilayer structures insensitive to capping layer optical parameters" Optics express, Vol. 16, Issue 19, pp. 15228-15237 (September 2008).

Proceedings:

1. **M. Suman**, M. G. Pelizzo, D. L. Windt, G. Monaco, S. Zuccon, and P. Nicolosi, "Innovative design of EUV multilayer reflective coating for improved spectral filtering in solar imaging", International Conference on Space Optics 2008 14-17th October (Tolouse).

2. **M. Suman**, M. G. Pelizzo, D. L. Windt, and P. Nicolosi, "Design of a-periodic broadband multilayers for x-ray astronomy", International Conference on Space Optics 2008 14-17th October (Tolouse).

Presentations at Conferences and Posters:

1. **M. Suman**, F. Frassetto, M.G. Pelizzo and P. Nicolosi, Reflection of ultra-short pulses by a-periodic multilayer mirrors: applications in the extreme ultraviolet spectral region, MMDMeeting, Genova, Italia.

2. **M. Suman**, F. Frassetto, P. Nicolosi, M. G. Pelizzo, A-periodic Multilayer Mirrors Applied to Ultra-Short Pulses Reflection in the Extreme Ultraviolet Spectral Region, ICXOM-XVIII, Frascati (Roma), Italia.

3. **M. Suman**, F. Frassetto, P. Nicolosi, M. G. Pelizzo, Design of Aperiodic Multilayer Mirrors for Ultra-Short Pulses in the Extreme Ultraviolet Region, XCI, Catania, Italia.

4. **M. Suman**, F. Frassetto, P. Nicolosi, M. G. Pelizzo, A-periodic Multilayer Mirrors for ultrashort Pulses in the Extreme Ultraviolet Spectral Region, XIII Users' Meeting at Elettra Synchrotron (Basovizza-Trieste).

5. **M. Suman**, F. Frassetto, P. Nicolosi, M. G. Pelizzo, XUV Multilayer Coating Design for Attosecond Pulse Compression, 90th OSA (Optical society of America) annual meeting, Rochester (NY), USA.

6. G. Monaco, D. Garoli, **M. Suman**, M. G. Pelizzo, P. Nicolosi, L. Armelao, Study of time degradation of Boron carbide thin film performances in EUV optics, 15th International Conference on Vacuum Ultraviolet Radiation Physics.

7. **M. Suman**, M. G. Pelizzo, P. Nicolosi, D. L. Windt, Multilayer Coatings For Attosecond Experiments In The VUV Spectral Region, the 9th International Conference on the Physics of X-Ray Multilayer Structures, Big Sky (Montana) USA.

8. **M. Suman**, M. G. Pelizzo, P. Nicolosi, G. Monaco, D. L. Windt, A. Giglia, S. Nannarone, A-periodic multilayers for EUV lithography, the 9th International Conference on the Physics of X-Ray Multilayer Structures, Big Sky (Montana) USA.

9. **M. Suman**, M. G. Pelizzo, D. L. Windt, G. Monaco, S. Zuccon, and P. Nicolosi, "Innovative design of EUV multilayer reflective coating for improved spectral filtering in solar imaging", International Conference on Space Optics 2008 14-17th October.

10. **M. Suman**, M. G. Pelizzo, D. L. Windt, G. Monaco, S. Zuccon, and P. Nicolosi, "Design of a-periodic broadband multilayers for x-ray astronomy", International Conference on Space Optics 2008 14-17th October.

11. **M. Suman**, Maria Guglielmina Pelizzo, David L. Windt, Gianni Monaco, Sara Zuccon, Piergiorgio Nicolosi, "Realization and characterization of XUV multilayer coating for attosecond pulses", 92th OSA (Optical society of America) annual meeting, Rochester (NY), USA 18-23th October.

12. **M. Suman**, Maria Guglielmina Pelizzo, David L. Windt, Gianni Monaco, Monica Gastaldi, Piergiorgio Nicolosi, "Realization and characterization of XUV multilayer coating for attosecond pulses", Short Wavelength Laboratory Sources (Cost meeting), Dresden (De) 27th November.